University of Alberta

Colloidal Fouling of Salt Rejecting Nanofiltration Membranes: Transient Electrokinetic Model and Experimental Study

by

Md. Abdullaha-Al-Mamun

A thesis submitted to the Faculty of Graduate Studies and Research in partial fulfillment of the requirements for the degree of

Master of Science

Department of Mechanical Engineering

Fall 2012
Edmonton, Alberta

Dedicated To,

My Parents:
Kulsum and Kalam;

my inspiration and strength

Abstract

Membrane separation processes are widely used for separation of colloids, macromolecules, organic matter and ions. Among different membrane processes, nanofiltration (NF) is being increasingly used for removing multiple molecular weight and size solutes ranging from colloidal particles to salt using a single membrane barrier. Fouling is a commonly encountered phenomenon in membrane processes, adversely influencing the permeate flux and membrane life. However, models of membrane fouling by multiple rejected components in the feed are mostly empirical. In this work, a transient electrokinetic model has been developed to predict the performance of salt rejecting membranes in presence of colloidal particles. The model combines the transient growth of colloidal cake layer and cake enhanced concentration polarization (CECP) of the salt to predict the permeate flux and observed salt rejection. The study provides fundamental insight into the development of streaming potential and electroosmotic back flow due to transport of ions around the charged spherical particles of the cake layer based on the Levine-Neale cell model of electrophoresis. This model is then coupled with film theory to assess the permeate flux decline and salt rejection during NF. To validate the model with experimental results, cross flow NF was conducted with silica particles and sodium chloride in aqueous systems over a range of operating conditions. The model predictions of flux and cake layer fouling were found to be in good agreement with the experimental results.

Keywords: Membrane Filtration, Nanofiltration, Cake Enhanced Concentration Polarization, Film Theory, Kuwabara Cell Model, Levine-Neale Electrophoretic Mobility, Electroosmotic Back Flow

Acknowledgements

I would like to express my gratitude to Dr. Subir Bhattacharjee, who had been more than a supervisor during the last two years. His motivation, enthusiasm and technical discussion, inspired and guided me through various challenges I faced during the program. His dedication as professor and supervisor, and his philosophies in life will always keep him at high level of respect in front of me.

I would like take the opportunity to thank Dr. Mohtada Sadrzadeh for his enduring guidance and support during the frustrations and hardship of my experiments. Over the last one year, the amount support and help I received from him is indescribable. I am grateful to Dr. Arnab Atta and Ni Yang for their consistent technical support and directions. I feel proud to have the opportunity of working with them. I was fortunate that I had really good colleagues, specially Josie Nebo. Her cordial support in all purposes made my life way more easier than I expected.

In addition, I want to thank Tushar, Saiful, Reeshav, Tathagata, Mafijul, Micah, Jannat, Ehsan, Hadi, Abhijit and Subhayan for their appreciation and support. I can not say enough to thank Michael Andrech for his excellent work for building the experimental setup.

Above all, I am very fortunate to have my parents who literally gave up everything in their life for me. They are being the strength and inspiration of my life.

Contents

List of Tables

List of Figures

Nomenclature

a	Colloidal particle radius, m
A_m	Area of membrane, m^2
A_K	Kuwabara correction factor
A_1	Parameter in Eq. 3.24
b	Cell radius, m
$C_{i,f}$	Concentration of electrolyte at feed (i.e. i=ions), M
$C_{i,\delta}$	Concentration of electrolyte at cake surface, M
$C_{i,m}$	Concentration of electrolyte at membrane surface, M
$C_{i,p}$	Concentration of electrolyte at permeate, M
$C_{p,f}$	Concentration of particle at feed (i.e. p=particles), ppm
$C_{p,m}$	Concentration of particle at cake layer, ppm
D	Brownian diffusivity (i.e. D_i and D_p), m^2/s
D_i^*	Hindered diffusivity of ions, m^2/s
d_e	Hydrodynamic diameter of cross flow channel, m
g^*	Electroosmotic correction parameter
g_2	Levine-Neal correction parameter
H	Height of the channel, m
k	Mass transfer coefficient (i.e. k_i and k_p), m/s
k_B	Boltzmann constant, J/K
L	Thickness of cake layer, m
L_c	Length of the channel, m
M	Parameter in Eq. 3.46
N_A	Avogadro number, $\#/mol$
n_i	Number concentration ($10^3 C_i N_A$), $\#/m^3$
q_s	Surface charge density, C/m^3
R	Universal gas constant, $J/molK$
R_c	Resistance of cake layer, m^{-1}
R	Flow turbulence parameter of solute(i.e. R_i and R_p)
R_i^*	Cake layer Peclet number
R_m	Resistance of membrane, m^{-1}
R_o	Observed rejection
R_o	Real rejection
r_c	Specific cake resistance, m^{-2}
T	Temperature, K
t	Dimensional time, s

u_c	Cross flow velocity, m/s
Greek Symbols	
ϵ	Electrical permittivity of water, F/m
ε	Porosity of cake layer
φ_c	Volume fraction of cake layer
μ	Viscosity of water, $Pa.s$
σ^{∞}	Bulk solution conductivity, S/m
λ_i	Molar conductivity, Sm^2/mol
ψ_p	Zeta potential of colloidal particle, mV
β	Parameter in Eq. 3.28
ρ_p	Density of colloidal particles, kg/m^3
τ	Normalized time

Chapter 1

Introduction

1.1 Background

Separation of dissolved and suspended matter from a solvent constitutes a major unit operation, and is important in virtually every industry, including, water treatment, environmental remediation, resource extraction, food processing, and effluent treatment, to name a few. Among various separation methods, membrane based separation processes have become extremely popular owing primarily to their lower operating expenses and lower energy consumption compared to other processes, such as distillation. Energy requirement in a distillation process involves the latent heat of vaporization, which is very high. However, membrane processes require lower energy as the separation occurs without a phase transition [Mulder, 1997]. Other advantages of membrane separation processes include:

- ability to utilize multiple driving forces, such as pressure, chemical potential, and thermal gradients
- easily integrable with other types of unit operations and processes
- modular and flexible designs, allowing easy scale up
- availability of a vast range of membrane materials and properties allowing tailored separations for targeted components.
- high selectivity during separation
- ability to remove dissolved solutes and ions from the solvent at low temperatures, thus avoiding thermal degradation.

Improvement of membrane materials, manufacturing technologies, mechanical strength and cleaning processes have progressively expanded the scope and application of membrane technology for complex and challenging separation problems over the past three decades [Escobar, 2010].

The energy required in membrane processes is provided as a driving force such as pressure, temperature, concentration, or electric field. Among different membrane processes, pressure driven filtration processes, classified as microfiltration (MF), ultrafiltration (UF), nanofiltration (NF), and reverse osmosis (RO), are widely used for separating constituents from liquid phase. These processes are nowadays practically considered best available technologies for water treatment. Typical characteristics and comparison of these membrane processes are provided in Table 1.1. These four classes of membrane processes, either alone, or in combination, are used for separation of inorganic colloids, organic matter, viruses, bacteria, pesticides, enzymes, and ions. The major challenges of these pressure driven membrane processes are concentration polarization (CP) and fouling by the entities retained by the membrane, which tend to accumulate on the membrane surface. Fouling may be defined as the irreversible deposition of retained particles, colloids, macromolecules, salt etc. on the surface or within the pores of membranes [Mulder, 1997]. This includes absorption [Marshall et al., 1993, Belfort et al., 1994, Banerjee and De, 2010], pore blocking [Taniguchi et al., 2003, Mattaraj et al., 2011], precipitation [Gouellec and Elimelech, 2002, Bhattacharjee and Johnston, 2002] and cake formation [Hong et al., 1997, Hoek and Elimelech, 2003]. CP and fouling are inherently part of the separation process [Mulder, 1997]. Thus, proper measures have to be taken to minimize these phenomena to ensure reliable operation of a membrane process, which makes the study of fouling mechanisms very pertinent.

Microfiltration (MF) and ultrafiltration (UF) processes are used for separation of particles and macromolecules, and the separation principle is based on the physical retention (sieving) of the suspended matter by microporous membranes based on particle size. Typically MF membranes retain particles > 100 nm, and have large pore sizes, whereas UF membranes retain macromolecules, colloids, and proteins in the size range of 5 to 100 nm. These two processes are not suitable for rejection of salts and divalent ions, as the pore size of the membranes used is larger than these entities. Fouling mechanisms during

MF and UF processes typically include pore blocking, solute adsorption, and cake/gel formation. The hydraulic or flow resistance of MF and UF membranes toward the permeation of the solvent are relatively low, which results in higher flux per unit pressure. Reverse Osmosis (RO) has been mostly used in desalination of water for the past four decades. RO membranes exhibit high rejection of monovalent salts [Tang et al., 2011]. The separation principle is based on the solubility of selected ionic components into the membrane as well as diffusivity of these components through the membrane (solution-diffusion mechanism). RO membranes have a dense active layer, with extremely low solvent permeability. Because of higher hydraulic resistance and osmotic pressure development, RO plants must operate at very high pressure. The high pressure requirement of RO processes makes it considerably energy intensive, and often the permeate water is extremely pure [Li et al., 2008], making the process suitable for ultrapure water production, such as in the semiconductor industry.

The development of nanofiltration (NF) about 20 years ago brought in a new surge of interest in pressure driven membrane separation processes. NF membranes have a higher permeability and exhibit lower rejection of monovalent ions ($< 70\%$) compared to RO processes. Tight NF membranes are in some ways similar to RO membranes, whereas loose NF membranes could probably be classified as UF membranes [Li et al., 2008]. NF membranes have higher rejection of multivalent ions ($> 99\%$) and organic matter ($> 90\%$). Therefore, NF processes acted as a bridge between UF and RO, allowing a facile method for removal of hardness generating divalent ions from water, and even for partial desalination of brackish waters employing considerably lower operating pressures than RO. More recently, several studies have explored whether NF can be used as a single unit operation to remove multiple molecular weight and size species like nano colloids, organic matter, and ions as a single pass membrane treatment. One of the outcomes of this trend is that fouling and performance decline mechanisms manifest in a very complex manner in NF processes including combination of cake formation, gel formation, scaling, and CP. Addressing the combined fouling mechanism of these constituents in NF processes involves several degrees of complexity.

A specific problem of interest in context of NF membrane fouling is the combined fouling due to cake formation by charged colloids retained by the membrane, and concentration polarization due to the retained ions. Such

fouling mechanisms are evident in numerous NF processes like desalination, water treatment, softening, produced water treatment in petroleum extraction and refining, *etc.* [Hoek and Elimelech, 2003, Yaun and Kilduff, 2010, De and Bhattacharjee, 2011]. This combined fouling by charged colloids and ions also forms the focus of the present study. The fouling by the charged colloids and the ions are not additive, but manifest in more complex manner, depending on the particle charge, particle size, ion concentration in the feed, and the membrane characteristics, such as the permeability and the salt rejection. The study focuses on developing a comprehensive understanding of how the rejection of these colloidal and ionic species, and other physico-chemical parameters synergistically influence such fouling.

Over the past decade, several models have been postulated to elucidate the mechanism of permeate flux decline and observed rejection variation during constant pressure operation due to colloidal fouling in salt rejecting membrane processes. The mechanism was first explained by Hoek and Elimelech [2003]. They conducted colloidal fouling experiments during cross flow NF and RO processes, and reported the flux decline due to cake enhanced osmotic pressure (CEOP) or cake enhanced concentration polarization (CECP). They explained the fouling mechanism as arising from hindered back-diffusion of salt ions within the colloidal deposit layers, resulting in an increase of CP as well as the transmembrane osmotic pressure (TMOP). Later, Wang and Tarabara [2007] proposed another approach to determine the contribution of CP and cake resistance on performance decline in experiments based on salt permeability measurement. Both of these approaches quantify the relative contribution of CEOP and cake resistance during constant pressure filtration experiments. However, none of these approaches consider the transient growth of the cake layer and couple it with CP phenomenon to develop a predictive model of permeate flux and observed rejection decline.

Earlier, CECP models also neglected an important property, zeta potential, of colloidal particles. Zeta potential affects the cake structure in addition to the permeation drag and salt concentration [Kim et al., 2006]. Besides, fluid flow and charge transport through a packed bed of colloidal particles are closely interrelated due to the formation of electric double layer (EDL) around the charged colloids. A new class of electrokinetic model for colloidal cake layer in cross flow filtration was introduced by Bowen and Jenner [1995a,b]. They

developed a dynamic UF model for charged colloidal dispersions including the particle-particle interaction and electroviscous effect. The electroviscous effect creates additional flow resistance for the cake layer due to streaming potential development [Rice and Whitehead, 1965, Levine et al., 1975]. The main drawback of their model was that it could not relate the cake structure to the electroviscous effect as the effect was formulated for charged nano pores. Recently, De and Bhattacharjee [2011] proposed an electrokinetic model for flux decline during cross flow filtration of charged colloids and electrolyte. Similar to Rice and Whitehead [1965] study, electroviscous effect was considered for the charged nano-pores in their model. Besides, this model did not provide mechanistic links between the electroviscous effect and CECP of salt rejecting membrane processes. None of these developed electrokinetic models related the particle-particle interactions and cake structure with electroviscous effect and coupled them with transient growth of cake layer to develop a mechanistic model of performance decline during NF membrane processes.

1.2 Objectives and scope

The main objectives of this study are:

- To develop a transient electrokinetic model for explaining the effect of cake layer growth, electroviscous resistance, and CECP on solvent and salt transport process within the cake layer of charged colloids, and explain the permeate flux and salt rejection behavior during the filtration process.

- To develop a cross flow membrane filtration setup for conducting experimental study on combined colloid-electrolyte fouling of NF membranes, perform controlled experiments using model colloidal suspensions as feed, and compare the experimental trends with the mechanistic model.

The applicability of the developed electrokinetic model is limited to non-interacting, incompressible colloidal particles yielding a constant cake porosity and indifferent monovalent electrolytes. The model is, however, developed in such a manner that the governing equations can be modified to incorporate particle-membrane and particle-particle interactions, multivalent ions, critical flux concept, and dynamic variations of the cake layer porosity. The experimental setup was developed to allow collection of transient flux decline and

rejection information during a fouling experiment in considerable detail over a long duration. This will allow highly sensitive parametric studies on fouling. The experimental results collected employing well-characterized colloidal suspensions will also serve as benchmark data sets, that will allow us to investigate the effect of properties of nano-colloidal foulants and experimental conditions on permeate flux, CECP and observed salt rejection of membranes. The experimental methodology developed in this study will provide the ability to conduct systematic studies on membrane fouling due to colloids, organic matter, and ions, and any combination of these in salt rejecting membrane processes to optimize the membrane performance.

1.3 Organization of the thesis

The objectives and scope of the present work is outlined in this chapter with a brief description of colloidal fouling mechanisms and limitation of the previous models.

Chapter 2 provides a detailed literature review on the mechanisms of membrane fouling, factors affecting membrane fouling, and CECP models. A comparative study on CECP models and their limitations justify the significance of the present transient electrokinetic model, thus providing the motivation of the modeling approach of this work.

Chapter 3 provides the mathematical framework of the present study. Details of colloid deposition, CECP and fundamentals of electrokinetic transport phenomena are described. The assumptions and framework of the electrokinetic model are outlined along with the governing equations of electroosmotic effect, cake layer growth, film theory, and transmembrane osmotic pressure. This is followed by the numerical methodology of solving the coupled model of cake layer growth and salt transport to obtain the permeate flux, observed rejection, osmotic pressure and deposited mass of the cake.

Chapter 4 describes the details of fouling experiments including foulant characterization, development of experimental setup, importance of membrane compaction, determination of critical flux, and protocol of colloidal fouling experiments. In addition, some important results of characterization, membrane compaction, and critical flux experiments are discussed in this chapter.

Chapter 5 describes the results of experimental validation along with the discussion on the experimental results and model predictions for different operating conditions. Contribution of electroosmotic back flow is also described in this chapter.

Finally in Chapter 6, conclusions from the present work are drawn, along with a brief overview of possible future work in this area.

Table 1.1 – Comparison of pressure driven membrane processes [Mulder, 1997, Li et al., 2008]

	MF	UF	NF	RO
Membrane morphology	microporous	micro- / nanoporous	nanoporous	dense skin
	100 - 1000 nm	5 - 100 nm	1 - 5 nm	< 1 nm
Separating components	particles	macro-molecules	colloids, multivalent ions, organic	monovalent ions
Separation principle	sieving mechanism	sieving mechanism	size exclusion and electro-kinetic	solution - diffusion
Salt rejection	no	no	monovalent ions ($< 70\%$), multivalent ions ($> 99\%$)	monovalent ions ($> 95\%$)
Osmotic pressure	negligible	negligible	high	very high
Fouling mechanism	pore blocking and cake/gel formation	pore blocking and cake/gel formation	scaling, cake/ gel formation, CECP	scaling, CECP

Chapter 2

Literature Review

2.1 Introduction

Membrane separation processes are increasingly being used in industries for separation of colloids, macromolecules, organic matter, and ions. The major operating costs associated with membranes include creating the operating pressure and mitigation of fouling. Both of these operating costs are directly related to the overall energy consumption of membrane filtration processes. The possible sources of fouling are [Schafer et al., 2004]:

1. Deposition of suspended colloidal particles
2. Precipitation of salts on membrane when their constituent ions exceed the solubility product or scaling
3. Adsorption of low molecular weight compounds
4. Gel formation by organic molecules
5. Chemical reaction on the membrane surface

In order to mitigate fouling, it is necessary to identify the foulants by characterizing them in solutions. Different foulants like colloids, organic matter and precipitants that are present in membrane filtration processes are shown in Fig 2.1. Knowing the type of foulant allows one to select the proper filtration process. Fouling mechanism is obviously affected by the type of foulant, and the selected filtration process. In conventional water treatment processes, MF and UF are used as pretreatment for NF or RO processes to remove large suspended particles [Hoek and Elimelech, 2003]. However, filtration of charged nano colloidal particles in the presence of electrolytes and hardness

generating ions are encountered quite often in NF and RO processes [Allen, 2008]. Deposition of suspended colloidal particles causes cake layer formation on the membrane surface. Fouling by the hardness generating ions are called precipitation fouling or scaling. The scale formation mechanism is different from cake formation by colloidal particles [Bhattacharjee and Johnston, 2002]. However, both scaling and cake formation happen in RO and NF membranes, which increase the electrolyte concentration polarization (CP) and enhance the transmembrane osmotic pressure (TMOP). This causes rapid performance decline in such membranes. Transport through the cake layer of charged colloids/precipitated crystals is a complex phenomenon. Hence, fouling during NF and RO processes become more complex and the system performance gets influenced by the foulant size, zeta potential, inter-particle interaction and ionic strength of solution [Bacchin et al., 2006, Bhattacharjee et al., 1999, Chong et al., 2007, Guell and Davis, 1996]. Therefore, study of the fouling mechanism of NF or RO process is important to develop a better understanding of the relation between the permeate flux, salt rejection, cake formation in a filtration process. In this chapter, existing literature on NF and RO fouling has been summarized. The review also includes previous studies on MF and UF membrane colloidal fouling for better understanding of the developed electrokinetic model in this work.

2.2 Mechanism of fouling

2.2.1 Modeling of concentration polarization

RO and NF membranes can retain solutes of few Angstroms (ions) to several nanometers (nano colloids). Separation of such solutes from their solution (ions) or suspension (nano colloids) leads to the formation of CP layer and/or cake layer on the membrane surface. Filtration of ions from their solution does not form any cake layer and filtration process is explained using the concept of CP employing the thermodynamics (osmotic pressure) approach of liquid solution [Elimelech and Bhattacharjee, 1998]. However, separation of colloids from their suspension can form both CP and cake layer. Song and Elimelech [1995] developed a theoretical model for CP of non interacting particles based on the hydrodynamic (filtration) approach of particles. The model could reveal the on set of cake formation by introducing a dimensionless filtration number. Filtration number is the ratio of the energy required to

bring a particle from the membrane surface to bulk suspension to the thermal (dissipative) energy of the particle. There is a critical value of filtration number above which cake layer forms on the membrane surface. It should be noted that filtration theory applied in this model is applicable for the stationary bed or cake layer of particles while the particles in CP layer are suspended in liquid state. Therefore, application of filtration theory in CP layer may be faulty unless the difference between a stationary bed and a suspension in liquid is not incorporated. Hence, Elimelech and Bhattacharjee [1998] developed another model of CP for small hard spherical solutes by utilizing the equivalence of thermodynamic (osmotic pressure) and hydrodynamic (filtration) approach. Therefore, during the combined filtration of ions and colloids, combination of osmotic pressure and filtration theory need to be utilized to explain the CP and cake formation. However, the osmotic pressure of colloids can be neglected due to their larger size compared to the ions.

2.2.2 Modeling of cake resistance

Filtration of colloidal particles can be divided into two regimes by the concept of critical flux. Critical flux can be defined as the flux below which there is no deposition of solutes as a cake layer on the membrane surface, and flux decline is solely due to CP [Howell, 1995]. The transition from CP to cake formation was experimentally studied for colloidal silica by systematically increasing the permeate flux and observing the system response during UF process [Chen et al., 1997]. Another improved way to determine the critical flux is the pressure step method [Espinasse et al., 2002], which allows rigorous determination of critical flux above which irreversible fouling or cake formation occurs. Therefore, fouling experiments have to conducted above the critical flux condition.

Formation of cake layer introduces additional hydrodynamic resistance to permeate flux. The hydrodynamic resistance for the cake layer of monodispersed noninteracting solutes can be estimated by simple Kozeny-Carman model [Carman, 1937]. However, Bowen and Jenner [1995a] used Wigner and Seitz [1933] cell model approach to account for multiparticle electrostatic (double layer) interaction within the filtered cake. The permeability of cake layer was calculated based on Happel cell model of concentrated particle system. Use of Happel cell model improved the applicability over a broad porosity range of the cake, while Kozeny-Carman model is primarily valid for low porosity

[Bowen and Jenner, 1995a, Kim et al., 2006]. The sole difference between the Kozeny-Carman and cell model is the fixed cake structure in Kozeny-Carman model, embodied by the assumed value of 5.0 for the Kozeny-Carman constant, and the variable cake structure in cell model [Kim et al., 2006]. The permeability model of packed bed of polydispersed spherical particles was given by Li and Park [1998], which allows to determine the specific resistance and flux decline during combined fouling process. They used cell model and effective medium approximation to account for the influence of neighboring particles. Kim et al. [2009] presented one of the most detailed model of three component combined fouling based on Happel cell approach to represent flux decline behavior of a system in dead end filtration process. Chemical and physical interactions play important roles in determining the structure of cake layer and the propensity of fouling a membrane [Zhu and Elimelech, 1997]. The particle-particle interaction using the Happel-cell model was incorporated in the flux decline model by Kim et al. [2006], to determine the cake structure and resistance during the cross flow filtration process. The approach provided better prediction of flux decline behavior during colloidal fouling. Therefore, cell models allow to incorporate variable structure of cake layer, inter-particle interactions and effect of neighboring particles in the filtration model. Cake compressibility is another important phenomenon for membrane processes, which increases the cake resistance with increasing pressure. Effect of compressibility is sometimes included in calculation of cake resistance by an empirical power law relation [Belfort et al., 1994, Buffle and Leppard, 1995]. The compressive drag force within the cake layer varies from zero at cake-CP interface to maximum at the membrane surface. Hence, the local cake volume fraction and specific resistance increase towards the membrane surface [Bowen and Jenner, 1995a]. Therefore, the local specific cake resistance varies as a function of position within the cake layer and time.

2.3 Other mechanisms of membrane fouling

Apart from CP and colloidal cake formation, membranes can also be fouled due to:

1. Gel formation
2. Adsorption
3. Pore blocking

4. Scaling

During high flux membrane filtration processes, the concentration of retained macromolecules at the membrane surface may reach very high values, and a critical maximum concentration may be reached referred to as gel concentration. The gel concentration on membrane surface depends on size, shape, structure, and solubility of the macromolecules [Mulder, 1997]. Further increase of operating pressure or permeate flux does not increase the solute concentration, and gel layer thickness increases. This implies that, gel layer becomes the limiting factor in determining the permeate flux during filtration of macromolecular solutions with high flux membranes [Mulder, 1997].

Adsorption can be defined as the interaction of membrane and solute even in absence of permeate flow through the membrane. Adsorption of solutes can occur on membrane surface and within pores. If the solutes are smaller than the pores of membrane, they can be adsorbed onto the pore wall. For large solutes, adsorption happens only on the membrane surface. Different mechanisms of flux decline during NF of organic matter was studied by Bruggen and Vandecasteele [2001], and adsorption was defined as the mechanism of flux decline. Bruggen et al. [2002] investigated the mechanism of flux decline during NF process due to adsorption of organic compounds. According to their investigation, surface charge and hydrophobicity of the membrane play major roles in solute adsorption.

Pore blocking mechanism is important for membrane processes for which foulants are smaller than the membrane pore size. If the particles are less than the pore size, they will deposit on the pore walls, reducing the effective pore radius and flow path for the permeate [Belfort et al., 1994]. Yuan et al. [2002] investigated humic acid fouling using a pore blockage-cake filtration model. According to their model, initial flux decline occurred due to pore blocking on the membrane surface and then cake layer grows in the region of blocked pores. Mattaraj et al. [2011] developed a coupled pore blockage, osmotic pressure, and cake filtration model to determine flux decline during NF of natural organic matters (NOM) and salts. Presence of sparingly soluble salt, specially $Ca_3(PO_4)_2$, deteriorated the membrane performance compared to soluble salts in presence of NOMs.

The fouling process of sparingly soluble electrolytes ($CaSO_4$, $CaHPO_4$ etc.), called precipitation fouling or scaling is slightly different from the fouling by colloidal particles and organic matter [Bhattacharjee and Johnston, 2002]. Bhattacharjee and Johnston [2002] developed a coupled model of CP, fouling by precipitation and ion transport through the membrane pore to predict the permeate flux decline during NF of multi component ionic mixtures. The model considers scaling layer build up by precipitated salt when the solubility product of specific ion pairs is exceeded, which causes the decline of permeate flux. Scaling by $CaHPO_4$ occurs quickly compared to $CaSO_4$ due to rapid nucleation [Shirazi et al., 2006]. However, for $CaSO_4$, the process has four stages. According to Lin et al. [2005], the four stages are: concentration polarization, nucleation, flux decline due to cake formation and steady-state filtration when scale growth is balanced by shear rate.

2.4 General factors affecting the colloidal fouling process

The performance of filtration process in presence of colloidal fouling is affected by different factors like operating and hydrodynamic conditions, properties of colloids and membranes, and solution chemistry. Numerous studies have been conducted to investigate the influence of individual parameter on performance of filtration processes. Proper understanding of individual factor is important for developing a filtration model so that effect of each parameter on membrane performance can be captured by the model. This section provides an overview of general factors influencing the colloidal fouling process.

2.4.1 Operating and hydrodynamic conditions

Hoek et al. [2002] investigated the influence of filter geometry and shear rate on colloidal fouling of RO and NF membranes. They derived a theory by combining solution-diffusion model, film theory and cake filtration model to quantify the interplay between the growing fouling layer and CP layer. The main mechanism of flux decline was referred as cake enhanced osmotic pressure (CEOP). The shear rate depends on the volumetric flow rate and cross flow channel height. Increase of shear rate, by reducing the channel height or increasing the volumetric flow rate, reduced the initial TMOP drop, mass deposition, and flux decline, while salt rejection was increased. However, reduced chan-

nel height has more significant effect compared to increased volumetric flow rate. For a constant shear rate, mass deposition and extent of fouling was controlled by the channel height and CEOP was substantially lower for the smaller channel height. For all cases, reducing the channel height reduced the initial TMOP, mass deposition and CEOP, while increased the salt rejection. Therefore, cross flow channel height and shear significantly affect the colloidal fouling mechanism of salt rejecting membrane processes.

2.4.2 Colloidal properties and interaction

A colloidal dispersion can be defined as a multi phase system, in which a dispersed phase is suspended in a continuous medium. In order to have a colloidal system, the dispersed phase should have a size at least one order higher than the size of continuous phase molecules. In this context, colloids are defined as particles having a size range of 1 nm to 10 μm [Masliyah and Bhattacharjee, 2006]. The most frequently found colloidal components in water are divided in two groups: inorganic colloids including amorphous silica, iron hydroxyde, $CaCO_3$, aluminosilicates (clays), etc. and organic colloids consisting microorganisms, biological debris, polysaccharides, organic fibrillar materials, gel-like organic materials, and soil-derived fulvic or humic compounds [Buffle and Leppard, 1995, Buffle et al., 1998].

The properties which contribute most to the nature of colloidal system are: particle size and shape, surface properties of colloids, physical and chemical properties of the continuous phase, particle-particle interaction, and particle-continuous phase interaction. These properties not only determine the interactions and stability of the colloidal system, but also determine the propensity of fouling a membrane. Inorganic colloids are present in different size and shape, and they are primarily rigid. Most of them are negatively charged at around neutral pH. Properties of colloidal particles also determine the structure of cake layer.

The effect of chemical and physical interactions on the fouling rate of RO membranes was investigated by Zhu and Elimelech [1997]. The colloidal fouling rate increases with the increase of ionic strength, colloid feed concentration, and pure water flux. Initial rate of colloidal fouling is controlled by the interplay between electric double layer repulsion and permeate drag. According to

their study, permeation drag plays more significant role than chemical interaction and controls the extent of fouling.

Effect of electrostatic double layer (EDL) interaction on the permeate flux decline and deposited cake structure was investigated by Faibish et al. [1998]. According to their study, solution ionic strength has more significant effect than pH on the rate of flux decline. The effect of ionic strength on flux decline increases as the particles size decreases. For a given size of particles the porosity and thickness increases as the ionic strength decreases. The cake layer porosity increases with decreasing particle size while the cake layer permeability decreases for a fixed physical and chemical condition. The decrease in cake layer permeability is due to increased hydrodynamic resistance for small colloidal particles at same physical and chemical condition. These results are attributed to the increased importance of EDL repulsion in controlling the cake structure for decreased ionic strength and particle size.

A detailed theoretical model was developed by Kim et al. [2006], to describe the cake layer structure and resistance for interacting nano particles during cross flow membrane filtration. The model considers the van der Waals, acid-base, electrostatic interaction forces, and permeate drag for governing the nano particle cake structure. At low ionic strength, the porosity of the cake layer is controlled by the electrostatic double layer interaction and permeate drag. At high flux and ionic strength, the porosity is controlled by short-range acid-base interaction and permeate drag. Their model also suggests that smaller nano particles produce more porous cake layer, which is in agreement with the result of Faibish et al. [1998]. Therefore, solution conductivity, pH and permeation drag influence the colloidal interaction and cake structure in filtration processes.

Contreras et al. [2009] studied the combined fouling of organic and inorganic colloids in NF membrane process. According to their study three mechanisms played role in performance decline in various degrees. These are increased hydraulic resistance of mixed cake layer structure, hindered back diffusion, and changes in colloid surface properties due to organic adsorption [Contreras et al., 2009]. Among these three mechanisms organic adsorption on colloid surface has most significant effect, which reduces the repulsion between foulants, as well as, foulants and membrane. Therefore, other than the

solution chemistry, presence of organic matter also affects the colloidal fouling behavior.

2.4.3 Properties of membrane

Membrane properties such as, zeta potential, surface roughness, hydrophobicity/hydrophilicity influence the fouling during the filtration process. Childress and Elimelech [1996] investigated the effect of solution chemistry on surface charge of NF and RO membranes using streaming potential analyzer. They analyzed the zeta potential of four different membranes at different ionic strength over the pH range of 2 to 9. The isoelectric point of NF and RO membranes in NaCl solution ranges from pH 3.0 to 5.2. Later, a novel asymmetric clamping cell was developed by Walker et al. [2002] to measure the average streaming potential and surface charge of the membranes. It is desirable to have higher zeta potential of the membrane to enhance the solute-membrane repulsion and reduce the intensity of fouling. However, hydrophobic interaction may overcome the repulsion and cause fouling.

Hoek et al. [2001] investigated the most influential membrane properties governing the colloidal fouling rate during the initial period of RO (LFC1 and X20) and NF (NF70 and HL) membrane processes. They characterized membranes for surface morphology, surface chemical properties, surface zeta potential and specific surface chemical structure. According to their study membrane surface roughness is the most influential property that governs the propensity of colloidal fouling. Particles preferentially accumulate in valleys of rough membrane causing significant flux decline during initial stage of the filtration process. To better understand the consequences of surface roughness on colloid deposition and fouling, Hoek et al. [2003] developed a technique to reconstruct the mathematical topology of polymeric membrane surface. They used statistical parameters derived from atomic force microscopy (AFM) roughness analysis of the membranes. Later, Boussu et al. [2007] studied the influence of membrane and colloidal characteristics on fouling of different NF membranes at different pH and ionic strength during the first 2 hrs of operation. Their study reveals that, rough membranes are most likely to foul by the particles. Large particles with more negative surface potential are beneficial for NF process where higher ionic strength leads to more fouling. Their experiments were conducted at higher cross flow velocity to minimize the ef-

fect of CP and to investigate the intrinsic fouling mechanism only. Rizwan and Bhattacharjee [2007] studied the initial deposition of colloidal particles (polystyrene latex) on rough NF90 membrane using AFM. According to their study, 100 nm particles preferentially accumulate near the peaks than the valleys of rough NF90 membrane. Therefore, properties like zeta potential and membrane roughness play major role in determining propensity of fouling.

2.5 Cake enhanced concentration polarization (CECP) or cake enhanced osmotic pressure (CEOP) model

To explain the combined fouling mechanism of colloids and electrolyte in salt rejecting membrane processes several methods were postulated. The mechanism was first successfully explained by Hoek et al. [2002] and Hoek and Elimelech [2003]. They conducted colloidal fouling experiments during cross flow filtration using RO (LFC1 and X20) and NF (NF70 and HL) membranes, and reported the flux decline due to CEOP phenomenon. They modeled the flux decline mechanism as hindered back-diffusion of electrolyte and altered cross flow hydrodynamics within the colloidal cake layers. Hindered back diffusion increases the CP on membrane surface resulting in an increase of TMOP. The CECP model can successfully describe the flux and observed rejection decline mechanism during an experiment using the experimental result of deposited mass. The independent variable of the theoretical model was cake thickness which again depends on filtration time. The model could not relate the cake thickness to filtration time because it did not consider the effect of operating and hydrodynamic condition on colloidal deposition on membrane surface.

Later, Wang and Tarabara [2007] proposed another approach to determine the contribution of CP and cake resistance on performance decline based on salt permeability constant measurement instead of considering hindered diffusivity within the cake layer. Kozeny-Carman equation was used to calculate the porosity from the cake resistance and experimental deposited mass.

These two approaches quantify the relative contribution of CP and cake resistance during constant pressure filtration experiments. Increase of salt rejection after the addition of colloidal particles was observed in both studies

which was attributed to the disturbance of steady state CP profile due to the addition of particles. However, none of these models consider the effect of channel geometry on transient growth of cake layer and couple it with CP phenomenon to establish a mechanistic model of permeate flux and observed rejection decline independent of experimental results. According to the preceding literature discussed in this chapter, the complete theoretical approach should combine the following three frameworks:

1. Transport mechanism of electrolyte and solvent through the colloidal cake layer and membrane which includes the influence of cake structure (volume fraction).

2. Transient growth of cake layer along the length of cross flow channel which includes the effect of operating and hydrodynamic conditions (section 2.4.1).

3. Chemical and physical interaction of colloidal particles within the cake to estimate the variable structure (section 2.4.2) and resistance (section 2.2.2) of the cake layer.

Later, Chong and Fane [2009] described a model to elucidate the performance of RO membrane process during colloidal fouling. The model considers the growth of cake layer by relating the critical flux and fractional deposition constant with time. Fractional deposition constant (Φ) quantifies the amount of silica convected to the membrane and finally deposited on the membrane. However, the model considers the fractional deposition constant to be 1.0 which limits the applicability of the model for high cross flow velocity [Chong et al., 2008]. Besides, the model does not include the effect of cross flow geometry on colloidal deposition and growth of cake layer.

All these three approaches used Kozeny-Carman equation to model the cake resistance. Kozeny-Carman model considers fixed cake structure whereas cell model considers variable cake structure. Therefore, cell model approach would allow to consider the inter-particle interactions in determining the variable cake structure [Kim et al., 2006]. Researchers have also tried to develop different experimental techniques to investigate the CECP phenomena considering the hindered back diffusion as the mechanism of performance decline [Chong et al., 2008, Yaun and Kilduff, 2010, Sim et al., 2011].

2.6 Electrokinetic model of CECP

Earlier model of CECP did not incorporate the zeta potential of colloidal particle which affect the cake structure [Kim et al., 2006]. In addition, transport mechanism of solvent and electrolyte through the packed bed of charged particles are closely interrelated due to the formation of EDL around the charged colloids. Transport of electrolyte through a charged packed bed develops a streaming potential which creates an electroviscous effect in addition to the hydrodynamic resistance of the packed bed [Schafer and Nirschl, 2005, 2010]. This electrokinetic transport phenomenon was first studied by Rice and Whitehead [1965] in narrow cylindrical capillaries. They developed an electrokinetic model of electroviscous resistance for the Debye-Hückel approximation ($\frac{ze\psi_p}{K_BT} \ll 1$). Debye-Hückel approximation limited the applicability of the theory for small zeta potential values. Later, Levine et al. [1975] extended the Rice and Whitehead [1965] theory for the higher zeta potential and developed an improved expression of electroviscous effect. Theoretical model of electroviscous effect within the charged capillary was further improved by Bowen and Jenner [1995b]. They avoided previous large number of analytical expressions and numerically solved the Poisson-Boltzmann equation for cylindrical capillary flow. They also extended the analysis of electroviscous effects by including the mobility of individual ionic species of symmetric electrolyte. Later, Bowen and Jenner [1995a] established a dynamic UF model for charged colloidal dispersions including the electroosmotic back flow due to the streaming potential development across the cake layer by applying their previous model [Bowen and Jenner, 1995b]. They applied the capillary model to porous cake layer by introducing an equivalent cylindrical capillary within the cake layer. The electroosmotic back flow increased the apparent viscosity and was referred to as electroviscous effect. De and Bhattacharjee [2011] proposed another electrokinetic model for determining the electroviscous resistance of cake layer and predicting flux decline during combined filtration of charged colloids and electrolyte. They also assumed the cake layer as a bundle of charged cylindrical nano-pores similar to the membrane for modeling the electroviscous effect. However, the electroosmotic flow or electroviscous effect through a bed of stationary colloidal particles must consider the effects of surrounding particles because the presence of neighboring particles affects the fluid velocity field and ion distribution in the immediate vicinity of each particle [Masliyah and Bhattacharjee, 2006]. It is therefore important to know how the concentration

of packed bed affects the electroosmotic flow of electrolyte. This problem can be solved by applying the cell model approach to the electroosmotic flow of electrolyte. Besides, this model does not provide mechanistic links between the colloidal particles characteristics and CECP.

2.7 Summary

This chapter presents a comprehensive literature review of the fouling mechanisms, general factors affecting the fouling process, and CECP mechanism for performance decline of salt rejecting membranes. A detailed study on the fouling mechanisms and factors affecting the extent of fouling is outlined. The preceding review provides ample justification for developing a new model of colloidal fouling in which the three frameworks (transient growth of cake layer, chemical and physical interaction of colloids within the cake layer, and transport mechanism of electrolyte and solvent) need to be coupled for a complete CECP model. The importance of electroviscous resistance and pertinent literature to explain the phenomena during fouling in cross flow filtration process is also discussed. Two frameworks, transient growth of cake layer and transport mechanism of electrolyte and solvent are combined in the present study. The cake layer has been modeled using the cell model approach, which allows to consider the inter-particle interaction and effect of neighboring particles on electroosmotic flow. However, inter-particle interactions are not included in this study to determine the cake structure. The details of fouling in cross flow filtration process and development of transient electrokinetic model of CECP is provided in the next chapter.

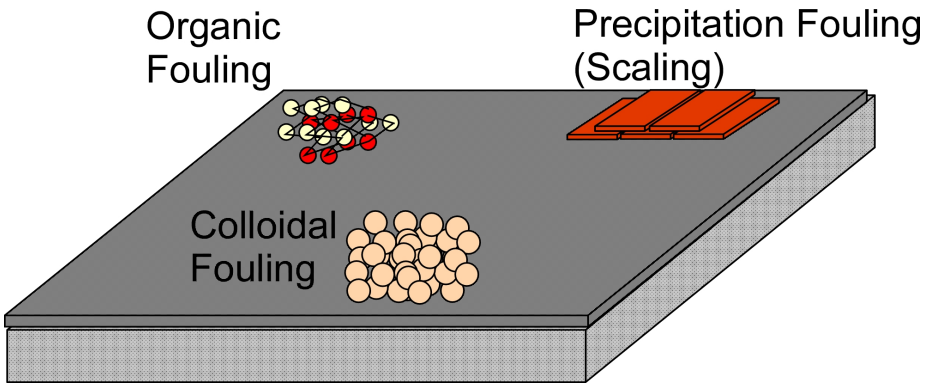

Figure 2.1 – Schematic representation of foulants in membrane processes

Chapter 3

Transient Electrokinetic Model

In this chapter, the combined fouling mechanism of electrolyte and charged colloids in cross flow membrane process has been described. First, a brief discussion of concentration polarization (CP), colloidal deposition and cake layer growth in cross flow has been presented. Following this, fundamentals of electrokinetic transport through the charged cake layer and development of electroosmotic back flow of solvent are presented. Finally, this chapter includes the governing equation of each transport processes and couple them together to develop the transient model. Numerical methodology of solving the set of governing equations are included at the end of the chapter. The transient electrokinetic model developed here allows to investigate the permeate flux and observed rejection decline and quantify the contribution of cake enhanced concentration polarization (CECP) and hydrodynamic resistance of cake layer on performance of nanofiltration (NF) processes.

3.1 Theory

During cross flow membrane filtration, permeation drag brings the solutes toward the membrane and keeps the rejected solutes in the vicinity of membrane surface. The axial flow transports the solutes along the cross flow channel and thus reduces the retentate concentration at the membrane surface. The accumulation of solutes at the membrane surface results in a CP layer and creates a concentration gradient from the membrane toward the bulk, which results in back diffusion of the solutes. Therefore, accumulation of solutes within the CP layer is controlled by three transport mechanisms: permeation drag, axial flow, and back diffusion, as shown in Fig. 3.1a. The cross flow hydrodynamics is important for larger solutes (greater than 300 nm) filtration processes

[Kim et al., 2006]. Cross flow hydrodynamics affects the inertial lift and shear induced diffusion influencing the solute back diffusion. If permeation drag is higher than the critical flux of cake formation, then the accumulated solutes form a cake layer on the membrane surface. After the formation of cake layer, the thickness of the cake layer continues to increase with filtration time until it reaches to a steady state value. Transverse transport of solvent occurs across the cake layer, which exerts hydrodynamic resistance to the permeate flux in addition to the membrane resistance.

Above the cake layer, there is CP layer of solutes. According to the filtration theory, due to the presence of CP layer, solvent encounters a specific resistance and pressure drop while traversing through the CP layer [Song and Elimelech, 1995]. On the other hand, according to thermodynamic approach, effective pressure is modified by introducing the term transmembrane osmotic pressure (TMOP) [Elimelech and Bhattacharjee, 1998]. Thermodynamic approach focuses on the determination of solute concentration and osmotic pressure across on the membrane surface. Therefore, permeate flux across the membrane arises due to the difference between applied pressure and TMOP. The applied pressure is the pressure difference between the bulk and permeate. However, the osmotic pressure model and filtration model are equivalent and address the flux decline due to CP from the thermodynamic and hydrodynamic point of view, respectively [Elimelech and Bhattacharjee, 1998].

During the combined filtration of electrolyte solution and charged colloidal particles, colloids form the stationary cake layer at the membrane surface above the critical flux and the electrolyte forms the CP layer on top of the cake layer, as shown in Fig. 3.1b. As the electrolyte and colloids in the CP layer are suspended in liquid state, there is no hydrodynamic pressure drop across the CP layer. Therefore, pressure at the bulk and cake surface can be considered same. Due to the large size of colloidal particles, osmotic pressure caused by them can be neglected and osmotic pressure of electrolyte is the dominant one. The formation of cake layer induces hydrodynamic resistance and transport of electrolyte occurs through tortuous interstices of the cake layer to the membrane surface. Due to the tortuous path in the cake layer, the back diffusion of electrolyte also gets hindered. As a result, CP increases on the membrane surface which enhances the TMOP and reduces the effective pressure. The phenomenon is referred to as cake enhanced osmotic pressure

(CEOP) or CECP of electrolyte and can be estimated by knowing the average porosity of the cake layer [Hoek et al., 2002].

However, colloidal particles can have surface charge, which in presence of electrolyte leads to formation of an electric double layer (EDL) around each particle. Therefore, transport process through the cake layer gets influenced by the electrokinetic phenomena. When an electrolyte flows through a charged porous medium under an applied pressure gradient, the charges in the mobile part of the EDL are transported toward the cake membrane interface. This creates a streaming current (I_s) and accumulated charges create an electric field. The electric field creates an opposite flow of charges referred to as conduction current (I_c). Conduction current is equal to streaming current at steady state. The potential difference developed across the porous medium at steady state is defined as streaming potential [Rice and Whitehead, 1965, Bowen and Jenner, 1995b,a, De and Bhattacharjee, 2011]. Development of streaming potential induces an electric field which creates an electroosmotic back flow opposite to permeate flux, thus imposing additional resistance to the hydrodynamic resistance of the cake layer and reduces the intensity of CECP. Therefore, cake layer resistance is comprised of two components: (i) hydrodynamic resistance of stationary bed of colloidal particles and (ii) electroviscous resistance due to the presence of charges. According to Darcy's law, the total resistance to permeate flow comprises two components: (i) membrane resistance and (ii) cake layer resistance. During the filtration process, the cake layer continues to grow with time and the permeate drag declines, which results in decrease of CP and colloid deposition. On the other hand, as the cake layer grows, the effect of hindered back diffusion increases. The electroosmotic back flow depends on the pressure gradient across the cake layer, cake porosity, electrolyte concentration and properties of colloidal particles. Therefore, the CECP phenomenon depends on the coupled effect of all these phenomena and changes with time, which makes the transport problem more complicated.

Figure 3.2a illustrates the CP profile and cake layer growth for the electrokinetic model. The retained colloidal particles at the membrane surface form the cake layer and the electrolyte creates the CP layer. At steady state of the filtration process, the thickness of the CP layer and cake layer, concentration of electrolyte at membrane surface and permeate flux depend on the axial position of the cross flow channel. The transport process of the present

model assumes the cake layer to be thin compared to CP layer thickness and no transport occurring within the cake layer in axial flow direction. This allows to consider the film theory for formulation of the electrokinetic model [Hoek et al., 2002]. Therefore, the complex transport model of two dimensional cross flow filtration simplifies to one dimensional mass transfer problem by assuming negligible axial solute transport at the membrane surface [Hong et al., 1997]. The mass transfer coefficient of solutes is considered to be constant and expressed using Leveque equation [Leveque, 1928, Kim and Hoek, 2005], as the cake thickness does not occupy a significant portion of channel height. In this study, the cake layer formed over the membrane surface by the colloids is modeled as a swarm of non interacting, incompressible, spherical, charged particles. The growth of the cake layer has been modeled using the mass balance of colloids at the cake surface as dead end filtration theory [De and Bhattacharya, 1997, Hong et al., 1997] . Several studies have showed that, dead end filtration theory provides a good approximation when modeling initial flux decline [Belfort et al., 1994]. The model assumes that the initial permeate flux decline is independent of the axial flow and most particles deposit in the cake layer by the permeation drag [Chong et al., 2008]. The Kuwabara [1959] cell model of concentrated suspension has been considered for formulating the hydrodynamic resistance of cake layer. The Levine and Neale [1974] model of electrophoretic mobility of a charged particle in a concentrated suspension has been used to evaluate the flow of solvent through the interstices of the porous cake layer, as shown in Fig. 3.2b. Kuwabara and Levine-Neal, both model considers the same cell boundary condition of azimuthal velocity to be zero at outer cell envelope. The salt transport within the cake layer considers hindered diffusivity due to tortuous path of cake layer and TMOP drop is calculated using the linear van't Hoff equation [Mulder, 1997].

3.2 Mathematical modeling

3.2.1 Film theory of cross flow filtration

The equation for pure water flux (v_w^o) is given as follows:

$$v_w^o = \frac{\Delta P}{\mu R_m} \tag{3.1}$$

here, operating pressure $\Delta P = P_b - P_p$, where, P_b and P_p are pressure at the bulk and the permeate, respectively, R_m is membrane hydraulic resistance and μ is dynamic viscosity of water.

During the filtration of electrolyte solution, electrolyte concentration profile develops on the membrane surface due to the rejection of ions. Such CP generates a diffusive back flow of electrolyte toward the bulk and develops a steady concentration profile at equilibrium. The driving force for permeate flux at the equilibrium condition is the difference between the applied pressure (ΔP) and the TMOP ($\Delta\pi$). Thus, the permeate flux (v_i) in presence of salt is described as:

$$v_i = \frac{\Delta P - \Delta\pi}{\mu R_m} \tag{3.2}$$

As the solutes in the polarized layer are suspended in liquid state, it is considered that there is no pressure drop across the polarized layer [Elimelech and Bhattacharjee, 1998]. The TMOP, $\Delta\pi = \pi_m - \pi_p$, where π_m and π_p are osmotic pressure at membrane surface and permeate, respectively.

When the colloidal particles are added to the system, they start depositing instantaneously on membrane surface, and their concentration increases on the membrane surface. When the volume fraction of colloids reaches maximum packing density, new layers of colloidal particles start to form and the thickness of cake layer increases. The permeate flux (v_w) is represented by the following resistance-in-series model or modified Darcy's equation [Hoek et al., 2002]:

$$v_w = \frac{\Delta P - \Delta\pi_m}{\mu(R_m + R_c)} \tag{3.3}$$

here, $\Delta\pi_m$ is enhanced TMOP, R_c is the total cake resistance including the hydrodynamic resistance of the packed bed and electroviscous resistance due to the presence of charged particles in electrolyte solution.

3.2.2 Electroviscous resistance of the cake layer

Hydrodynamic resistance

The model considers structure of cake layer as a swarm of non interacting spherical particles and is represented using the Kuwabara cell model [Kuwabara, 1959]. Cell model focuses on a single particle and a representative volume of fluid phase enclosing that particle instead of considering the overall structure

of the suspension [Masliyah and Bhattacharjee, 2006]. To elucidate the electrokinetic transport of solvent and electrolyte through the interstices of cake layer, consider a single colloidal particle within the cake illustrated in Fig. 3.2b. The figure provides the schematic representation of the model where, a colloidal particle of radius a (m) and zeta potential ψ_p (mV) is considered stationary in a spherical coordinate system. The radius of the fluid phase enclosing the particles is b (m) and determined from the volume fraction (φ_c) of the cake layer as, $b = a/\varphi_c^{1/3}$.

The hydrodynamic drag exerted by the stationary colloidal cake layer is derived from the Stokes-Einstein law of a single particle. The Stokes drag is then combined with the Kuwabara cell model to account for the effect of neighboring particles within the cake layer. The expression of drag force on a particle is given as follows:

$$F_{D,Stokes} = 6\pi\mu a A_K v_w \tag{3.4}$$

where A_K is the correction factor accounting for effect the neighboring particles in the cake layer. According to Kuwabara [1959] cell model :

$$A_K = \frac{1}{1 - \frac{9}{5}\varphi_c^{1/3} + \varphi_c - \frac{1}{5}\varphi_c^2} \tag{3.5}$$

The pressure drop across a unit thickness of cake layer in the direction of permeate flow is the product of $F_{D,Stokes}$ and number density of particles $n_p = 3\varphi_c/4\pi a^3$, within the cake layer. Therefore, the pressure gradient across the cake layer is given as:

$$\frac{\Delta P_c}{L} = 6\pi\mu a A_K v_w n_p \tag{3.6}$$

which yields the following equation of permeate flux:

$$v_w = \frac{\Delta P_c}{\mu r_c L} \tag{3.7}$$

here, ΔP_c is pressure drop across the cake layer, L is cake layer thickness and r_c is the specific hydrodynamic cake layer resistance expressed as:

$$r_c = \frac{9\varphi_c A_K}{2a^2} \tag{3.8}$$

The unit of specific resistance is m^{-2}.

Electroosmotic back flow

The expression of specific cake resistance does not include the effect of reverse electroosmotic flow due to streaming potential development. To consider the effect of electroosmotic flow, electrophoresis of single charged particle in a concentrated suspension is considered based on Levine and Neale [1974] model. According to the Levine-Neale model, the total potential within the system is assumed to be $(\phi + \psi_p)$, where ψ_p arises from the charge of the particle and ϕ arises from the induced streaming potential. The potential distribution is solved using the Poisson equation:

$$\epsilon \nabla^2 \psi_p = -\rho_f \tag{3.9}$$

where, $\psi_p = \psi_p(r)$ depends on radial position and ρ_f is the volumetric free charge density. Boundary conditions for Eq. 3.9 are:

$$\frac{d\psi_p}{dr} = -\frac{q_s}{\epsilon} \quad \text{at} \quad r = a \tag{3.10a}$$

$$\frac{d\psi_p}{dr} = 0 \quad \text{at} \quad r = b \tag{3.10b}$$

where, q_s is the surface charge density. The boundary condition of Eq. 3.10a relates the surface potential gradient to the surface charge density and Eq. 3.10b refers to non conducting surface or isolated fluid shell from the other particle.

The potential distribution due to the induced electric field $\phi(r, \theta)$ is governed by the following equation:

$$\nabla^2 \phi = 0 \tag{3.11}$$

The boundary conditions of Eq. 3.11 are:

$$\frac{\partial \phi}{\partial r} = 0 \quad \text{at} \quad r = a \tag{3.12a}$$

$$\frac{\partial \phi}{\partial r} = -E_\infty \cos\theta \quad \text{at} \quad r = b \tag{3.12b}$$

Equation 3.12a recognizes that dielectric permittivity of the particle is insignificant compared to the surrounding fluid and Eq. 3.12b refers to the fact that electric field is undisturbed at the cell envelope.

Using the Debye-Hückel approximation ($\frac{ze\psi_p}{k_BT} \ll 1$) [Masliyah and Bhattacharjee, 2006], the solution of the potentials are:

$$\psi_p(r) = \left(\frac{q_s a}{\epsilon}\right)\left(\frac{a}{r}\right)\left[\frac{\sinh(\kappa b - \kappa r) - \kappa b \quad \cosh(\kappa b - \kappa r)}{(1-\kappa a.\kappa b)\sinh(\kappa b - \kappa a) - (\kappa b - \kappa a)\cosh(\kappa b - \kappa a)}\right] \tag{3.13}$$

and

$$\phi(r,\theta) = \left(-\frac{E_\infty}{1-\varphi_c}\right)\left(r + \frac{a^3}{2r^2}\right)\cos\theta \tag{3.14}$$

where, $q_s = \epsilon\kappa\psi_p(1 + 1/\kappa a)$ and κ is the inverse Debye length expressed as:

$$\kappa = \left(\frac{2e^2z^2n_{i,f}}{\epsilon k_B T}\right)^{1/2} \tag{3.15}$$

The flow around the spherical particle is governed by the Navier Stokes equation for creeping flows. The body force on the charged particle is given by $\rho_f\nabla(\psi_p + \phi)$, which yields the following equation:

$$\mu\nabla^2\mathbf{u} = \nabla P + \rho_f\nabla(\psi_p + \phi) \tag{3.16}$$

and the continuity equation is written as:

$$\nabla \cdot \mathbf{u} = 0 \tag{3.17}$$

The boundary conditions for the Navier Stokes and continuity equations based on Kuwabara [1959] cell model are:

$$u_r(r,\theta) = u_\theta(r,\theta) = 0 \quad \text{at} \quad r = a \tag{3.18a}$$

$$u_r(r,\theta) = -U\cos\theta \quad \text{at} \quad r = b \tag{3.18b}$$

$$\omega_\theta = \frac{1}{r}\frac{\partial(ru_\theta)}{\partial r} - \frac{1}{r}\frac{\partial(u_r)}{\partial\theta} = 0 \quad \text{at} \quad r = b \tag{3.18c}$$

The assumptions for above set of boundary conditions are:

1. No slip condition at the particle surface, Eq. 3.18a.
2. At the cell boundary radial velocity is defined in terms of mean relative velocity (U) of the interstitial fluid with respect to the particle, Eq. 3.18b.
3. Azimuthal component of vorticity is zero at the outer cell envelope, Eq. 3.18c.

Using the above set of boundary conditions, the solution of electrophoretic mobility is given by [Levine and Neale, 1974]:

$$\eta = \frac{U}{E_\infty} = \left(\frac{\epsilon\psi_p}{\mu}\right) g_2(\kappa a, \varphi_c) \tag{3.19}$$

where, $g_2(\kappa a, \varphi_c)$ accounts for the presence of neighboring particles, which is evaluated using Levine-Neale model. The expression of $g_2(\kappa a, \varphi_c)$ in Levine-Neale expression of electrophoretic mobility was given by Ohshima [1997]:

$$\begin{aligned} g_2(\kappa a, \varphi_c) &= -\frac{2}{3(1-\varphi_c)} \int_a^b \left\{ 1 - \left(\frac{a}{r}\right)^3 + \frac{3}{2}\left(\frac{a}{r}\right)^5 + \right. \\ &\left. \frac{\varphi_c}{10}\left[1 - 10\left(\frac{r}{a}\right)^3 + 6\left(\frac{a}{r}\right)^5\right]\right\} \frac{1}{\psi_p}\frac{d\psi_p^{(0)}}{dr} dr \end{aligned} \tag{3.20}$$

where, the function $\psi_p^{(0)}$ is given by:

$$\psi_p^{(0)} = \psi_p \frac{a}{r}\left(\frac{\sinh[\kappa(b-r)] - \kappa b \cosh[\kappa(b-r)]}{\sinh[\kappa(b-a)] - \kappa b \cosh[\kappa(b-a)]}\right) \tag{3.21}$$

According to Eq. 3.19, as the particles are stationary, under the application of an electric field E_∞, there has to be a fluid velocity U opposite to the direction of E_∞ to keep the particles stationary. Therefore, in absence of an applied pressure gradient, the electrolyte solution will flow past the particle at a velocity U along the direction of electric field, which is referred to as the electroosmotic velocity. The electroosmotic velocity through the interstices of the cake layer along the direction of induced streaming potential with respect to the particle is given from Eq. 3.19 as follows:

$$U = E_\infty \left(\frac{\epsilon\psi_p}{\mu}\right) g_2(\kappa a, \varphi_c) \tag{3.22}$$

The streaming potential development is related to the pressure gradient of the cake layer ($P_y = \Delta P_c/L$). The expression of induced streaming potential (E_∞) in electrophoretic mobility, Eq. 3.19, at zero current condition, in accordance with Onsager principle of reciprocity for irreversible phenomena, is given as [Masliyah and Bhattacharjee, 2006]:

$$E_\infty = \frac{\Delta P_c}{L}\left(\frac{\epsilon\psi_p}{\mu\sigma^\infty}\right)\left(1 - \frac{2\ I_1(\kappa a)}{\kappa a\ I_0(\kappa a)}\right) \tag{3.23}$$

In Eq. 3.23, $\sigma^\infty = \sum \lambda_i C_{i,f}$ is bulk solution conductivity, $C_{i,f}$ is electrolyte concentration in feed and λ_i is molar conductivity. Here, $I_0(\kappa a)$ and $I_1(\kappa a)$ are

zeroth and first order modified Bessel function of the first kind, respectively. According to this equation, the electric field increases with the increased pressure gradient and zeta potential of cake layer, and reduced conductivity of the salt solution. The expression for bulk electroosmotic flux across the cake layer can be written from interstitial fluid velocity using the continuity assumption as follows:

$$u_w = U(1-\varphi_c) = \frac{\Delta P_c}{L\sigma^\infty}\left(\frac{\epsilon\psi_p}{\mu}\right)^2 (1-\varphi_c) g_2(\kappa a, \varphi_c) A_1 \tag{3.24}$$

where,

$$A_1 = 1 - \frac{2\ I_1(\kappa a)}{\kappa a\ I_0(\kappa a)} \tag{3.25}$$

Electroviscous resistance

The total flux across the cake layer due to effective cake pressure ΔP_c and reverse electroosmotic flux (u_w) is given as follows:

$$v_w = \frac{\Delta P_c}{\mu r_c L} - u_w \tag{3.26}$$

which yields the following equation:

$$v_w = \frac{\Delta P_c}{\mu R_c} \tag{3.27}$$

here, $R_c = r_c L/g^*$ is the cake layer resistance. The parameter g^* accounts for electroosmotic effect within the cake layer and expressed as follows:

$$g^* = [1 - 9\varphi_c(1-\varphi_c) A_K \beta g_2(\kappa a, \varphi_c) A_1] \tag{3.28}$$

The parameter g^*, quantifies the change of apparent viscosity ($\mu_a = \mu/g^*$) in models of electroviscous effect. However, in the present calculations, g^* is considered as the electroviscous resistance ($R_c = r_c L/g^*$). As electroviscous resistance is inversely proportional to g^*, decrease of this parameter quantifies the increase of electroosmotic back flow due to the streaming potential development across the charged cake layer. The parameter $g_2(\kappa a, \varphi_c)$ strongly depends on κa and is independent of volume fraction at large κa values [Masliyah and Bhattacharjee, 2006]. The parameter β quantifies the effect of zeta potential (ψ_p) and solution conductivity (σ^∞) on electroosmotic back flow and expressed as follows:

$$\beta = \frac{(\epsilon\psi_p)^2}{2a^2\mu\sigma^\infty} \tag{3.29}$$

3.2.3 Electrolyte transport

Through the CP layer

The electrolyte solution builds up CP layer on cake surface. The mass balance of electrolyte within the concentration polarization layer ($0 < y < \delta$) is (Fig. 3.2a):

$$v_w C_{i,p} = v_w C_i - D_i \frac{dC_i}{dy} \tag{3.30}$$

with the boundary conditions as follows (see Fig. 3.2a):

$$C_i = C_{i,f} \quad \text{at} \quad y = 0 \tag{3.31a}$$

$$C_i = C_{i,\delta} \quad \text{at} \quad y = \delta \tag{3.31b}$$

Integrating the Eq. 3.30 with the above boundary conditions gives the following equation:

$$\frac{C_{i,\delta} - C_{i,p}}{C_{i,f} - C_{i,p}} = \exp(v_w/k_i) \tag{3.32}$$

where, $k_i = D_i/\delta$ is salt mass transfer coefficient obtained using Leveque equation [Leveque, 1928]:

$$k_i = 1.86 \left(\frac{D_i^2 u_c}{d_e L_c} \right)^{\frac{1}{3}} \tag{3.33}$$

Through the cake layer

The electrolyte transport through the cake layer is modeled based on the average mass balance within the cake layer ($\delta < y < \delta + L$) as follows (Fig. 3.2a):

$$v_w C_{i,p} = v_w C_i - D_i^* \frac{dC_i}{dy} \tag{3.34}$$

with the following boundary conditions (see Fig. 3.2a):

$$C_i = C_{i,\delta} \quad \text{at} \quad y = \delta \tag{3.35a}$$

$$C_i = C_{i,m} \quad \text{at} \quad y = \delta + L \tag{3.35b}$$

Solution of Eq. 3.34 with the given boundary conditions is:

$$\frac{C_{i,m} - C_{i,p}}{C_{i,\delta} - C_{i,p}} = \exp\left(v_w L/D_i^*\right) \tag{3.36}$$

Using the Eqs. 3.32 and 3.36, expression of dimensionless salt concentration at the membrane surface or CP modulus can be written as:

$$\bar{C}_{i,m} = \frac{C_{i,m}}{C_{i,f}} = \frac{\exp\left(v_w/k_i + v_w L/D_i^*\right)}{R_r + (1 - R_r)\exp\left(v_w/k_i + v_w L/D_i^*\right)} \tag{3.37}$$

where, $R_r = 1 - C_{i,p}/C_{i,m}$ is real rejection of the membrane and D_i^* is hindered diffusivity, expressed as:

$$D_i^* = \frac{\varepsilon D_i}{\varsigma} \tag{3.38}$$

where, $\varsigma = 1 - \ln(\varepsilon^2)$ is the tortuosity [Boudreau, 1996, Hoek and Elimelech, 2003].

3.2.4 Growth of cake layer

Simplification of the complex transport problem to one dimensional mass balance of colloidal particles within the concentration boundary layer ($0 < y < \delta$), gives the following governing equation [De and Bhattacharya, 1997]:

$$\rho_p \frac{dL}{dt} = v_w C_p - D_p \frac{dC_p}{dy} \tag{3.39}$$

The pertinent boundary conditions for colloid concentration from Fig. 3.2a are:

$$C_p = C_{p,f} \quad \text{at} \quad y = 0 \tag{3.40a}$$

$$C_p = C_{p,m} \quad \text{at} \quad y = \delta \tag{3.40b}$$

Solution of Eq. 3.39 for concentration with the above boundary conditions is [De and Bhattacharya, 1997]:

$$\rho_p \frac{dL}{dt} = v_w \frac{C_{p,m} - C_{p,f} \ \exp(v_w/k_p)}{1 - \exp(v_w/k_p)} \tag{3.41}$$

Here t is duration of filtration after the addition of colloid particles, $C_{p,f}$ is feed concentration of colloids, $C_{p,m}$ is concentration of colloids in the cake layer and ρ_p is density of colloid particles. For small colloidal particles, back diffusion (D_p) is dominated by Brownian diffusion whereas for large colloidal particles (greater than 300 nm) back diffusion mechanism is dominated by shear induced diffusion and/or inertial lift [Belfort et al., 1994, Kim et al., 2006]. Due to difficulty of determining the colloid mass transfer coefficient (k_p) at specific length of the slit channel and as the cake layer thickness is assumed to be very small compared to the height of the channel, length average k_p for laminar flow in slit channel has been obtained by Leveque [1928] expression:

$$k_p = 1.86 \left(\frac{D_p^2 u_c}{d_e L_c} \right)^{\frac{1}{3}} \tag{3.42}$$

From electrolyte concentration at cake-membrane interface the dimensionless TMOP is expressed as the van't Hoff equation,

$$\Delta\pi_m = 2RT(C_{i,m} - C_{i,p}) \tag{3.43}$$

Finally, the observed salt rejection of the membrane can be written as:

$$R_{i,o} = 1 - \frac{C_{i,p}}{C_{i,f}} \tag{3.44}$$

3.2.5 Pressure drops

Overall pressure drop during operation is the summation of pressure drop across the cake layer and the membrane. Therefore,

$$\Delta P = \Delta P_c + \Delta P_m + \Delta\pi_m \tag{3.45}$$

where, ΔP_c and ΔP_m are the pressure drops across the cake layer and membrane, respectively.

3.2.6 Non-dimensional governing equations

To facilitate the solving procedure of above set of differential-algebraic equations, the governing equations were non-dimensionalized against the pure water flux ($v_w^o = \Delta P/\mu R_m$), applied pressure (ΔP), membrane resistance (R_m) and hydrodynamic diameter of cross flow channel (d_e). The normalized cake layer resistance is:

$$R_c^* = \frac{R_c}{R_m} = \frac{L^*}{Mg^*} \tag{3.46}$$

here, $L^* = L/d_e$ is normalized cake thickness and $M = R_m/r_c d_e$. The normalized TMOP from Eq. 3.43 is expressed as:

$$\Delta\pi_m^* = \frac{\pi_m}{\Delta P} = \alpha\bar{C}_{i,m} \tag{3.47}$$

where, $\alpha = 2RTR_rC_{i,f}/\Delta P$ and the expression of $\bar{C}_{i,m}$ from Eq. 3.37 is:

$$\bar{C}_{i,m} = \frac{\exp\left[v_w^*(R_i + L^*R_i^*)\right]}{R_r + (1 - R_r)\exp\left[v_w^*(R_i + R_i^*L^*)\right]} \tag{3.48}$$

here, $R_i = v_w^o/k_i$ and $R_i^* = v_w^o d_e/D_i^*$. The normalized permeate flux from Darcy's law (Eq. 3.3) is expressed as:

$$v_w^* = \frac{v_w}{v_w^0} = \frac{1 - \Delta\pi_m^*}{1 + R_c^*} \tag{3.49}$$

The cake layer growth, Eq. 3.41, in non-dimensional form can be written as follows:

$$\frac{dL^*}{d\tau} = v_w^* \frac{\bar{C}_{p,m} - \exp(v_w^* R_p)}{1 - \exp(v_w^* R_p)} \tag{3.50}$$

where, $\tau = \frac{v_w^o C_{p,f}}{d_e \rho_p} t$ is normalized time, $\bar{C}_{p,m} = \frac{C_{p,m}}{C_{p,f}}$ is normalized cake layer concentration and $R_p = v_w^o / k_p$. Finally, the observed rejection is expressed as:

$$R_{i,o} = 1 - (1 - R_r)\bar{C}_{i,m} \tag{3.51}$$

The relative pressure drops due to TMOP, cake and membrane resistance can be calculated from the following non-dimensional pressure equation expressed from Eq. 3.45:

$$\Delta {P_c}^* + \Delta {P_m}^* + \Delta \pi_m^* = 1 \tag{3.52}$$

here, $\Delta {P_c}^* = v_w^* R_c^*$ is normalized trans-cake hydrodynamic pressure. The TMOP ($\Delta \pi_m^*$) and transmembrane pressure ($\Delta {P_m}^*$) are calculated from Eqs. 3.47 and 3.52, respectively.

3.3 Numerical methodology

The resulting set of non-dimensional differential-algebraic Eqs. 3.46 to 3.50 are solved using a coupled differential algebraic equation solver (DASSL) in Fortran. DASSL is an open source code that can be found in the SLATEC library from Netlib's repository (www.netlib.org). DASSL solves a system of differential-algebraic equation of the form $F(T, Y, Y') = 0$ where, F, Y and Y' are N dimensional vectors, Y' is the derivative of Y [Petzold, 1982]. A consistent set of conditions T, Y and Y' at initial time must be known so that $F(T, Y, Y') = 0$. DASSL solves the system of equation for Y and Y' for a specific range of independent variable, ΔT. The algorithm of DASSL involves replacing the derivative with a k^{th} order backward difference formula (BDF) and using a predictor-corrector method. The predictor-corrector polynomials are specified using the value k ranging from one to five [Maier et al., 1993]. An absolute solver accuracy of 1×10^{-4} has been used for the DASSL. A subroutine RES in DASSL was used to define the system of differential-algebraic equations.

The electrokinetic model considers the cross flow geometry, operating pressure, cross flow velocity, properties of solvent, colloids and membrane, and feed concentrations as known quantities. The viscosity and dielectric constant of

water was 1.0×10^{-3} $Pa.s$ and 80.0, respectively, at 25℃. The concentration of colloidal particles in the cake layer was considered to be 200 kg/m^3 for 0.2 kg/m^3 feed concentration [Zaidi and Kumar, 2005]. The cake concentration was 200 kg/m^3 for all the analysis.

3.4 Summary

This chapter provides the mathematical model of cake enhanced concentration polarization in cross flow membrane filtration. Each phenomenon contributing to flux is elaborated in addition to the corresponding equations. The formulation of electroviscous resistance and cake layer growth are outlined. To solve the system of differential-algebraic equations, the equations are simplified to dimensionless form for numerical solution. The numerical methodology for solving the electrokinetic model is also discussed along with assumed parameters. The validation of electrokinetic model will be presented in Chapter 5 along with the comparison of experimental results.

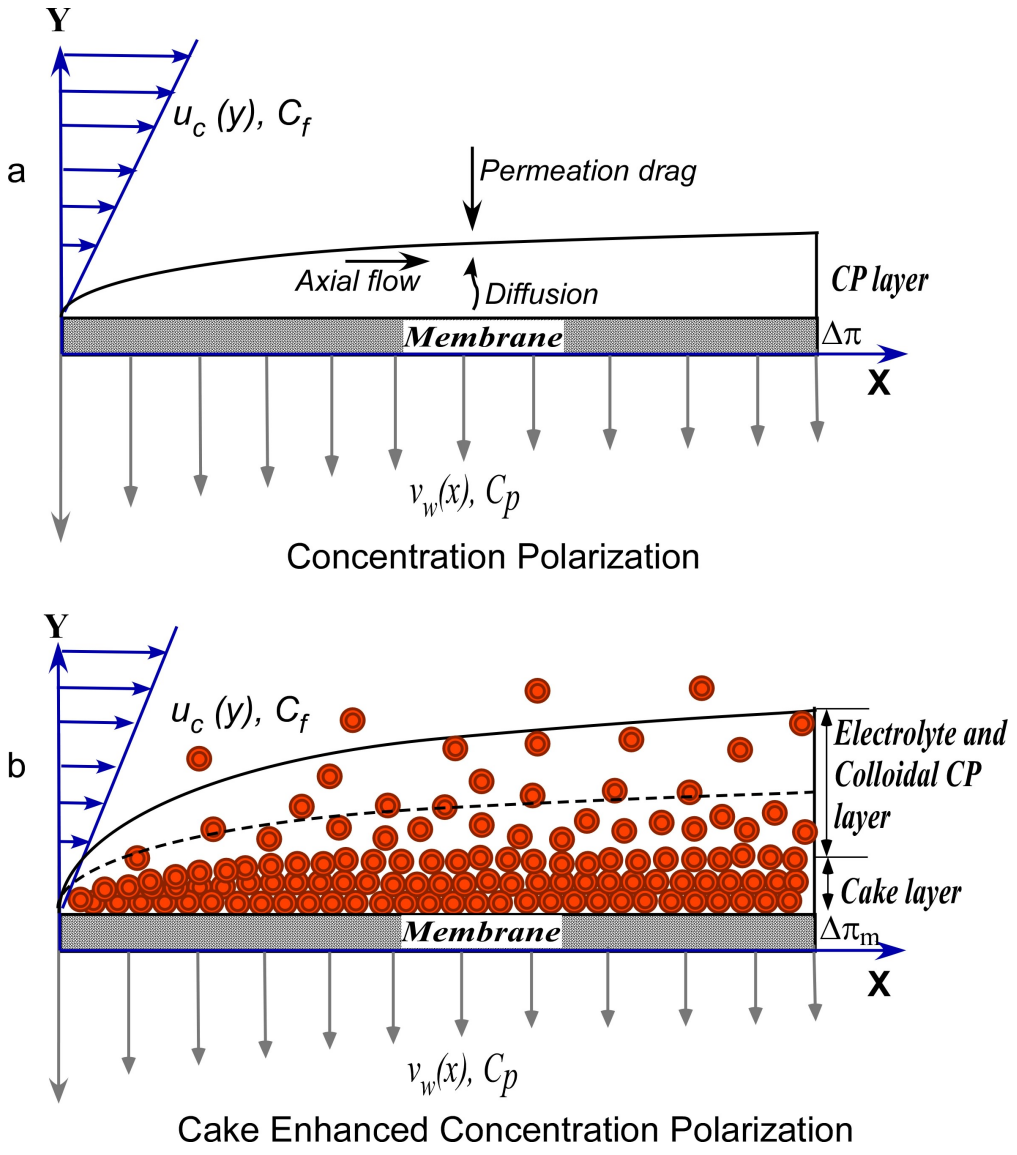

Figure 3.1 – Schematic representation of steady-state a) concentration polarization phenomenon, and b) cake enhanced concentration polarization phenomenon, under the influence of permeate drag and cross flow velocity in a cross flow filtration unit

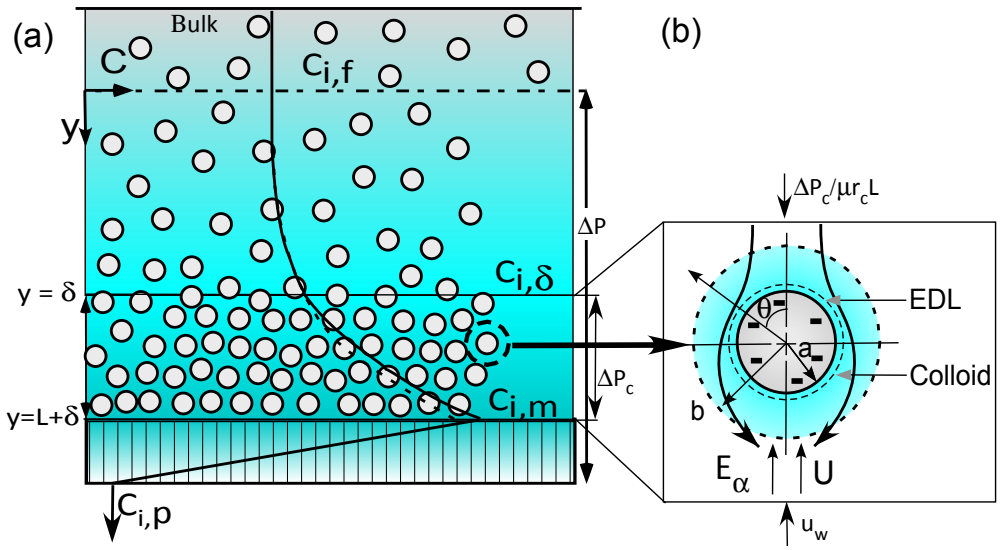

Figure 3.2 – a) Transport of electrolyte through CP layer, cake layer and membrane, here, δ is CP layer thickness, L is cake thickness, ΔP is applied pressure, ΔP_c is pressure drop across the cake layer, $C_{i,\delta}$ is salt concentration at cake surface and $C_{i,m}$ is salt concentration at membrane surface. b) Levine-Neale electrophoretic flow model, here, E_∞ is streaming potential, U is electroosmotic velocity, $\Delta P_c/\mu r_c L$ is permeate flux and u_w is electroosmotic flux.

Chapter 4

Cross Flow Nanofiltration of Aqueous Salt Solution in Presence of Silica Colloids

In this chapter, details of cross flow nanofiltration (NF) of salt solution in presence of silica colloids is described. First, the chapter provides a brief description of properties of membrane, silica particles and salts, following the measurement of size and zeta potential of particles. Then, features of the established cross flow experimental setup and basics of LabVIEW data acquisition has been presented. The chapter also describes the importance and procedure of membrane preconditioning and determination of critical flux before colloidal fouling experiment. Finally, the chapter includes the detail methodology of colloidal fouling experiment. The methodology developed in this chapter allows to scientifically conduct the fouling experiments, explain the results and validate the present model.

4.1 Colloids, membranes and reagents

As model colloidal foulant, nanoparticles of 25 nm, 40-50 nm and 70-100 nm diameter were used for the experiments. Nanoparticles of 25 nm were Ludox TM 50 (50 wt% suspension in water) from Aldrich Chemistry. The particles of 40-50 nm and 70-100 nm were Snowtex 20L (20 wt% suspension in water) and Snowtex ZL (40 wt% suspension in water), respectively, supplied from Nissan Chemical America Corporation (Houston, TX). The pH of colloidal suspensions were 9.5 to 10. The average size and zeta potential of particles were determined using Dynamic Light Scattering (DLS) and Acoustic and

Electroacoustic spectrometer. The density of the silica particles were 2360 kg/m^3.

The NF membrane was aromatic polyamide composite membrane (NF90, supplied by Dow FilmTec). The membrane samples were immersed in deionized water and stored at 5℃. The NF90 polymeric composite membrane comprises three layers: aromatic polyamide active layer, polysulfone inter layer and polyester support web. The thickness of the active layer is less than 1 μm. The average roughness of NF90 membrane is 65 nm [Rizwan and Bhattacharjee, 2007] and zeta potential from streaming potential measurement is -18 mV within the pH range of 7 to 9 in 10 mM NaCl solution [Bellona and Drewes, 2005]. The average hydraulic resistance (R_m), real rejection (R_r) and observed rejection (R_o) of the membrane were $4.0 \pm 0.1 \times 10^{13}$ m^{-1}, 97% and 90±1%, respectively. Maximum operating pressure and temperature for the membrane is 4135 kPa and 45℃, respectively [Rizwan, 2009].

Salt solution was prepared by dissolving ACS grade 99% NaCl crystals (Sigma Aldrich) in demineralized water. The pH of the solution was adjusted using ACS-grade HCl and NaOH, for particle size and zeta potential measurements.

4.2 Properties of colloids

4.2.1 Sample preparation

It is important to characterize the colloidal particles to mechanistically explain the fouling experimental results. Therefore, the particle size and zeta potential were measured prior to the fouling experiments. To measure the size and zeta potential of the silica particles, samples were prepared as follows:

- Solution of 10 mM NaCl in deionized water was prepared in a round bottom flux.
- Then 2.5 g Ludox TM or 3.125 g Snowtex ZL dispersion having pH 9 was weighed in a beaker.
- After that, colloidal dispersion was diluted to 125 g total weight using 10 mM NaCl solution to prepare 1 $wt\%$ colloidal suspension in 10 mM NaCl solution.

- Then, HCl or NaOH was added to adjust the pH of the samples.
- The samples were stirred for 12 hrs. and ultrasonicated for 1 hr, to make sure that silica particles are not aggregated.
- Then the pH, particles size and zeta potential of the each sample were measured and plotted in graphs.

The particles size and zeta potential were measured using the Acoustic and Electroacoustic spectrometer DT-1200 for which minimum concentration of suspension is 1 $wt\%$. The particle size and zeta potential were also measured using DLS and ZetaPALS (Brookhaven), respectively.

4.2.2 Particle size and zeta potential

The size of silica particles were measured using DLS and DT-1200 Acoustic spectrometer and shown in Fig. 4.1. The DLS measurement provides hydrodynamic diameter of the particles. The size of Ludox TM particles varied from 25 nm to 38 nm within the pH range of 2 to 10.5 in 10 mM NaCl concentration. The Snowtex ZL particles size varied from 115 nm ot 145 nm for 10 mM NaCl solution over the pH range. Therefore the Ludox TM and Snowtex ZL particles were stable for the pH range in 10 mM NaCl ionic strength solution. The size of Snowtex 20L particles were 55 nm at pH 7.2 in 10 mM NaCl solution.

The zeta potential of Ludox TM and Snowtex ZL particles at different pH were measured for ionic strength of 10 mM NaCl using Electroacoustic spectrometer at 25℃ and plotted as function of pH in Fig. 4.2. The experimental results for Ludox TM particles were comparable with the industrial data available from Horiba Scientific. The zeta potential measurement of Ludox TM using ZetaPALS was also in good agreement with the Electroacoustic spectrometer results as shown in Fig. 4.2. The negative zeta potential of Ludox TM and Snowtex ZL particles increased with increasing pH. The zeta potential of Ludox TM and Snowtex ZL particles within the pH 7 to 9 in 10 mM NaCl solution varied from -30 to -35 mV and -30 to -45 mV, respectively. In 10 mM NaCl solution and at pH 7.2 the Snwotex 20L showed zeta potential of -35 mV.

4.3 Cross flow membrane filtration setup

The laboratory scale cross flow membrane filtration (CFMF) setup shown in Fig. 4.3 was developed from commercial stainless steel (SS) Sepa CF cell (Sterlitech Corporation, Kent, USA). The rated operating pressure of the unit was 6895 kPa (1000 psi). The cross flow cell had channel dimension of 14.6 cm × 9.5 cm × 1.7 mm. The effective membrane area and cross sectional flow area for these dimensions were $1.40 \times 10^{-2} m^2$ and $1.62 \times 10^{-4} m^2$, respectively. This channel dimension provided the cross flow velocity 0.1 m/s and Reynolds number 344 (laminar) for the experimental condition of 1 LPM cross flow rate. A constant flow diaphragm pump of maximum capacity 6.8 LPM (1.8 GPM) from Hydra-Cell was used to provide feed to the Sepa CF cell at a maximum 6895 kPa (1000 psi) pressure. The feed suspension was supplied from a 19 L (5 Gallons) stainless steel tank opened to atmosphere. Feed water temperature was maintained at temperature of 24±1℃ by a recirculating heater/chiller (Isotemp 3013, Fisher Scientific). The original setup was modified by replacing the concentrate control valve placed at the channel outlet with a back pressure regulator (Swagelok, Edmonton, Canada). A by-pass valve and a pressure gauge was installed before the channel inlet. The combination of by pass valve and back pressure regulator (BPR) allowed fine and constant control over a wide range of applied pressure and cross flow velocities within the CFMF unit. The BPR stability and sensitivity was improved by replacing the soft original o-ring of seat retainer with a more stiffer one. A regular maintenance operation of the BPR was the replacement of o-ring when the BPR could not control the constant operating pressure and cross flow velocity. The applied pressure was monitored using a bourdon tube pressure (Aschrof, USA) installed before the back pressure regulator and retentate flow rate was monitored using a floating disk rotameter installed after the BPR. Gauge protectors or snubbers were installed at the inlet of pressure gauges to protect the pressure gauge from high frequency fluctuation associated with the reciprocating pump. Weighing balance (Mettler), digital flow meter (Coleparmer) and two conductivity probe in conductivity meters (Fisher Scientific and Mettler) were used to measure the permeate weight, permeate flow rate, and feed and permeate conductivity. Permeate line was returned back to the feed tank for maintaining constant electrolyte concentration in feed tank. A conductivity chamber having dead volume of 30 mL was designed and installed at permeate return line to measure the permeate conductivity. The chamber

was made using PVC to the avoid interference of the SS conductivity probe with chamber wall. The results were collected directly into the computer using the data acquisition system. The data acquisition system was developed using the LabVIEW (National Instruments).

4.4 Data acquisition using LabVIEW

The CFMF setup was interfaced with the computer for data acquisition using LabVIEW 8.0. The weighing balance, digital flow meter and conductivity meters were connected to the computer using RS-232 serial communication and each serial port was defined as "VISA Resource Name" or COM(i) port where, i = 1,2,3,....n. The baud rate, data bits, parity, stop bits and flow control of the interfaced instruments and computer have to be same for the successful communication. Therefore, the serial or COM port was configured using the "VISA Configure Serial Port" Virtual instrument (VI). The baud rate, data bits, parity, stop bits and flow control were set to 9600, 8, None, 1.0 and None, respectively. The same configuration was followed for all the instruments and computer. After all of these five parameters of instrument and computer were synchronized, the instruments were ready to receive and execute the command. Hyperterminal was used to confirm the communication before using LabVIEW. The specific command to receive data from the instrument was defined by the Standard Interface Command Set Manual of each instrument. The specific command was sent to the instrument from the "Write Buffer" using "VISA Write" VI. The instrument executed the specific command and returned information to the serial port. The "ActiveX Property Node"function was used to read the number of bytes returned from the instrument. Then the "VISA Read" VI was used to read the information from the serial port using the number of bytes information which returned the result as a string in a "Read buffer". After that, specific measured value was scanned from the read buffer using "Scan From String" function and appended to an array using "Build Array" function. Then the 1-D data was written into a "*.lmv"file using the "Write to Spreadsheet File" VI. Each instrument was interfaced using a different block diagram and executed sequentially at each iteration. All the block diagrams were executed inside a "Timed Loop" for specific period of the experiments. The total time duration to execute the program was defined for each experiment and interval of each execution was set to 1 minute. After the total time duration, all the Visa resources were

closed using the "VISA Close" VI.

4.5 Membrane compaction and hydraulic resistance

Before conducting colloidal fouling experiments, it is necessary to compact the membranes hydrostatically to acquire constant membrane properties, with regard to water permeation. Different water flux values of a new membrane (before compaction) and a used one (after compaction) demonstrates why membrane pre-compression was needed. The swelling and compaction tendency of polymeric membrane matrix determines the pure water permeability at different pressures. Intrusion of water molecules into the polymer swells the polymer matrix and increases water flux by increasing the diffusion rates at higher pressures. In contrast, membrane compaction under an applied pressure decreases the fractional free volume within the polymer matrix, and leads to a denser structure. As a consequence, the water flux decreases. The combined effect of swelling and compaction determines the permeability and hydraulic resistance of a polymeric membrane. Figure 4.5 shows the permeate flux results of new and used NF90 membrane with time at different operating pressures. The operating pressure was increased and decreased step wise from 275 to 1240 kPa and 1240 to 275 kPa, respectively, for the new membrane. The permeate flux was monitored for 15 minutes at each pressure. Then, the same experiment was conducted after compacting the membrane at 1515 kPa for 2 hrs. During these two steps, the cross flow rate was maintained 1 LPM. As can be seen, for a new membrane, different flux values were obtained at different pressures. However, symmetric permeate flux versus time plot was obtained for the compacted membrane, showing small hysteresis and stable values at different pressures.

In order to further explain the permeate flux behavior of new membrane during this experiment, the permeate flux and membrane resistance were plotted against the applied pressure as shown in Figs. 4.6 and 4.7, respectively. The dotted lines represent new membrane and solid lines represent membrane after compaction. The closed and open symbols show the trend of pressure increase and decrease, respectively. According to these figures, the permeate flux increased and hydraulic resistance decreased with the increased applied pressure for the new membrane. The decline rate of resistance at higher pressure

was small and it became almost constant at 1100 and 1240 kPa. This behavior can be attributed to the dual effect of membrane swelling and compaction on permeate flux by increasing the applied pressure. Increasing the pressure increases both compaction and swelling of the membrane. In the case of a new membrane, effect of swelling is dominant and results in non-linear flux vs. pressure graph (Fig. 4.6) as well as decreasing trend for hydraulic resistance with increasing pressure (Fig. 4.7). At higher pressures, the counter effects of swelling and compaction are equal, which leads to constant hydraulic resistance. Hysteresis can also be observed in Figs. 4.6 and 4.7. For the compacted membrane, the permeate flux changed linearly and resistance remained constant both for the increasing and decreasing trends of pressure, which shows no hysteresis after equilibrating the membrane at higher pressure. The average hydraulic resistance of the equilibrated membranes was $4 \pm 0.1 \times 10^{13}$ m^{-1}. Therefore, membrane compaction at a pressure higher than fouling experiments pressure (which was estimated by critical flux experiments) must be done before each experiment.

4.6 Critical flux of colloidal particles

The objective of the present work is to validate the developed model, investigate the contribution of fouling resistance and CECP on the performance of NF90 membrane. Therefore, the experiments must be conducted at fluxes higher than critical flux to ensure that colloidal fouling is happening for both small and large particles. Experimental protocol to determine the critical flux is based on the pressure step method [Espinasse et al., 2002]. In this method, each steady state flux measurement at an applied pressure is followed by a decrease in applied pressure in order to determine the reversibility or irreversibility according to Fig. 4.8 (i). The advantage of this method is, it allows a rigorous determination of the critical flux above which irreversible colloidal fouling occurs.

By comparing the corresponding flux obtained at pressure steps 1 and 4 in Fig. 4.8 (ii), one can determine whether the flux obtained in step 3 is due to irreversible (cake formation) or reversible (concentration polarization layer) fouling phenomenon. According to Fig. 4.8 (ii) if the flux in step 4 is on point b, fouling is irreversible or cake formation occurs at membrane surface and if the flux is on point a, fouling phenomenon is by concentration polarization

(CP). Therefore, reversible or irreversible fouling can be determined according to the flux value at step 4 (included on segment a-b). The procedure to estimate the critical flux was as follows:

- The membrane was compacted for 2 hrs. at 1515 kPa.
- Then, 10 L solution with 10 mM NaCl and 300 ppm of 100 nm silica was added in the tank. The feed flow rate was maintained at 1 LPM.
- The first pressure to measure the permeate flux was 275 kPa. Then the applied pressure was increased from 275 kPa to 345 kPa.
- After that, the applied pressure was reduced from 345 to 275 kPa and the flux was recorded.
- The pressure was again increased from 275 to 415 kPa, then reduced to 345 kPa, and the permeate flux was measured.

  Note: At each pressure, flux was monitored for 20 minutes to ensure stable performance. The pressure was increased until critical flux or irreversibility was obtained.
- After the irreversibility or attainment of critical flux, the pressure was increased another three steps and permeate flux was measured.
- Then, applied pressure was reduced stepwise from the maximum to minimum pressure, and permeate flux was measured.
- The applied pressure and permeate flux was plotted against time. Then permeate flux vs. pressure graph was plotted. The point at which flux became irreversible was the critical flux where irreversible fouling or cake formation occurs.

Fig. 4.9 shows the critical flux experiment results for Snowtex ZL (100 nm) colloidal particles with details of pressure steps used during the experiment. Same experiment was conducted for Ludox TM (25 nm) particles. The experimental results are then plotted as Permeate flux vs. Pressure in Fig. 4.10 along with the result of pure water flux and 10 mM NaCl solution flux. The experimental results of 100 nm particles shows that, the permeate flux observed up to 482 kPa was reversible and almost equal to the salt water flux. The irreversible fouling or cake layer formation first appeared at 550 kPa and at 620 kPa the irreversibility became significant. Therefore, according to

Fig. 4.10, the critical flux for irreversible cake formation is around 1.16×10^{-5} m^3/m^2s for 100 nm colloidal particles. The results of 25 nm colloidal particles are different from 100 nm. The permeate flux was reversible up to 825 kPa, and was significantly less than the 10 mM NaCl salt water flux. The observed lower permeate flux behavior of 25 nm particles can be attributed to a new initial resistance (R_i) as follows [Espinasse et al., 2002]:

$$v_w = \frac{\Delta P - \Delta \pi_m}{\mu(R_m + R_i + R_c)} \tag{4.1}$$

This initial resistance is due to the CP of small particles, which can be accounted using either the filtration theory [Song and Elimelech, 1995] or osmotic pressure model [Elimelech and Bhattacharjee, 1998], and blocking of pores at the valleys of membrane [Hoek et al., 2001, Boussu et al., 2007]. According to filtration theory, the CP layer of particles causes an hydrodynamic resistance (R_i) to permeate flux. As the roughness of NF90 membrane is 65 nm [Rizwan and Bhattacharjee, 2007], it is possible that 25 nm colloids get trapped at the membrane valleys and causing an initial resistance. According to Fig. 4.10, irreversible fouling first occurred at 965 kPa and at 1100 kPa the irreversibility increased. Therefore, the corresponding critical flux for 25 nm particles is 1.35×10^{-5} m^3/m^2s. Another representation of critical flux or irreversible cake formation for 25 nm colloids is shown in Fig. 4.11. According to the figure, 25 nm particles exerts an initial resistance (R_i), additional to membrane resistance (R_m) until the flux reaches to critical flux [Espinasse et al., 2002]. After the critical flux, the normalized fouling resistance increases with the increase of permeate flux at different pressure steps. Above analysis indicates that, permeate flux decline in presence of nano-colloidal particles can occur below the critical flux. This flux decline depends on the solute-solute and solute-membrane interactions [Hoek et al., 2001, Boussu et al., 2007]. However, solute-solute interaction is more prominent than solute membrane interaction in determining the CP layer resistance because CP is an instantaneous phenomena compared to valley clogging of rough membrane and resulting in rapid flux decline. From above analysis, it can be summarized that during fouling experiment with 25 nm silica particles in 10 mM NaCl solution, the operating pressure has to be higher than 965 kPa to observe the fouling phenomena, which is higher than 550 kPa for 100 nm silica particles.

4.7 Colloidal fouling experiment

4.7.1 Membrane resistance, observed rejection, initial transmembrane osmotic pressure and mass transfer coefficient

The colloidal fouling experiments were conducted according to the procedure described by Hoek and Elimelech [2003]. The following steps were followed before the addition of colloidal particles in feed tank.

- Prior to each experiment, the membrane was compacted for 2 hrs. at 1515 kPa. After the 2 hrs. of compaction, the applied pressure (ΔP) and cross flow velocity (u_c) were set to the desired condition of the filtration experiment.

- The pure water flux (v_w^o) was measured for 1 hr and membrane resistance (R_m) was calculated using the following equation:

$$v_w^o = \frac{1}{A_m}\frac{dV}{dt} = \frac{\Delta P}{\mu R_m} \tag{4.2}$$

- Then, an electrolyte (NaCl) solution was added to obtain desired feed concentration ($C_{i,f} = 10\ mM$) and equilibrated for 1 hr. The permeate and retentate were returned to the feed tank to maintain constant salt feed concentration.

- During the equilibration process, the permeate flux, feed, and permeate conductivity were measured. From the permeate conductivity measurement, the observed salt rejection ($R_{i,o}$) was calculated as follows:

$$R_{i,o} = 1 - \frac{C_{i,p}}{C_{i,f}} \tag{4.3}$$

- From the permeate flux data, transmembrane osmotic pressure (TMOP) ($\Delta\pi$) was measured using the following equation:

$$v_i = \frac{\Delta P - \Delta\pi}{\mu R_m} \tag{4.4}$$

- The initial mass transfer coefficient (k_i) of electrolyte was calculated using $\Delta\pi$, $R_{i,o}$ and following osmotic pressure equation:

$$\Delta\pi = 2RT\ C_{i,f}\ R_{i,o}\ \exp(v_i/k_i) \tag{4.5}$$

- The measured mass transfer coefficient was cross checked against calculated mass transfer coefficient for laminar flow in rectangular channel as follows [Leveque, 1928]:

$$k_i = 1.86(\frac{D_i^2 u_c}{d_e L_c})^{\frac{1}{3}} \tag{4.6}$$

4.7.2 Permeate flux and observed salt rejection decline due to colloidal fouling

After electrolyte equilibration, desired dose of silica colloidal particles was added to the feed tank to provide appropriate colloid feed concentration ($C_{p,c}$). The pH was adjusted to the desired value for the experiment. The operating pressure and cross flow velocity was maintained same as electrolyte equilibration step. The permeate flux and conductivity values were collected at one minute interval during the experiment to obtain permeate flux (v_w) and measure the observed rejection ($R_{i,o}$). The pH of feed solution was also measured at the beginning and end of fouling experiment.

Mass of deposited cake layer

The mass of colloidal cake layer was determined by measuring feed solution concentration at different time interval and conducting simple mass balance of the feed suspension according to Fig. 4.12. Suppose, at initial time $t = 0$ the feed concentration is $C_{p,0}$ and volume is $V_{f,0}$. Therefore, the total mass at time $t = 0$ is $m_0 = C_{p,0}V_{f,0}$. At a time, $t = t$, the feed concentration is $C_{p,t}$ and sample volume is $V_{f,0}$. Therefore, the mass of silica in feed at time t is $m_t = C_{p,t}V_{f,0}$. The feed concentrations ($C_{p,t}$) at different times were measured by UV absorbance analysis using a UV-VIS Spectrometer (Varian Carey 50). The path length for the UV-absorbance experiment was 10 mm and wavelength was chosen 225 nm to minimize the effect of NaCl solution absorbance. During the UV absorbance analysis, scan mode of the instrument was used instead of simple read. This allowed UV absorbance measurement of the sample over wide range of wavelength and provided more flexibility to use specific wavelength for calculation. The mass reduction from the tank during time t was the amount of mass deposited on the membrane surface and was calculated using the following equation:

$$dm = m_0 - m_t \tag{4.7}$$

which yields:

$$M_d = \frac{dm}{A_m} = \frac{C_{p,0}V_{f,0} - C_{p,t}V_{f,0}}{A_m} \tag{4.8}$$

here, M_d is the amount of deposited mass per unit area of the membrane and A_m is the effective membrane area. The cake layer hydrodynamic resistance is described by M_d using the hydrodynamic drag exerted by spherical colloids within the cake layer based on Kuwabara cell model.

$$R_c = \frac{9\varphi_c A_K}{2a^2 g^*}\frac{M_d}{\rho_p \varphi_c} \tag{4.9}$$

where $\varphi_c = 1 - \varepsilon$ is the volume fraction of the cake layer, ε is the average cake layer porosity, a is particle diameter, L is cake thickness, A_K is the correction factor accounting for the effect of neighboring particles in the cake layer, and g^* accounts for electroosmotic effect in swarm of charged colloidal particles. The expressions of A_K and g^* are given in Eq. 3.5 and 3.28, respectively. The thickness of the cake layer (L) is related to the amount of deposited mass as follows:

$$L = \frac{M_d}{\rho_p \varphi_c} \tag{4.10}$$

where ρ_p is the particle density.

Cake enhanced osmotic pressure

The cake enhanced osmotic pressure (CEOP) was calculated based on the experimental results of permeate flux (v_w) and cake layer resistance (R_c) using the following equation:

$$\Delta\pi_m = \Delta P - v_w \mu (R_m + R_c) \tag{4.11}$$

The CEOP was also calculated based on modified van't Hoff equation,

$$\Delta\pi_m = 2RT \quad C_{i,f} \quad R_{i,o} \quad \exp(v_i/k_i^*) \tag{4.12}$$

where k_i^* is the combined hindered mass transfer of ions within the CP layer and cake layer. The hindered mass transfer coefficient was calculated using the mass transfer of ions within the CP layer and hindered diffusivity of ions within the cake layer as follows:

$$k_i^* = \left[L\left(\frac{1}{D_i^*} - \frac{1}{D_{i,\infty}}\right) + \frac{1}{k_i} \right]^{-1} \tag{4.13}$$

where, $D_{i,\infty}$ is the bulk diffusivity and D_i^* is the hindered diffusivity expressed in Eq. 3.38. The average cake layer porosity (ε) is the sole fitting parameter to set the Eqs. 4.11 and 4.12 equal. The expression of CP modulus is written as:

$$\bar{C}_{i,m} = \frac{C_{i,m}}{C_{i,f}} = \frac{\exp\left[v_w/k_i^*\right]}{R_r + (1 - R_r)\exp\left[v_w/k_i^*\right]} \tag{4.14}$$

4.8 Summary

A detailed methodology of fouling experiments in cross flow filtration process is presented in this chapter. The procedure of colloids and membrane characterization, details of experimental setup, basics of LabVIEW instrumentation, importance of membrane compaction, methodology for determination of critical flux and procedure of fouling experiment have been provided in this chapter. The experimental results obtained by the methods described are explored in the next chapter along with validation of transient electrokinetic model.

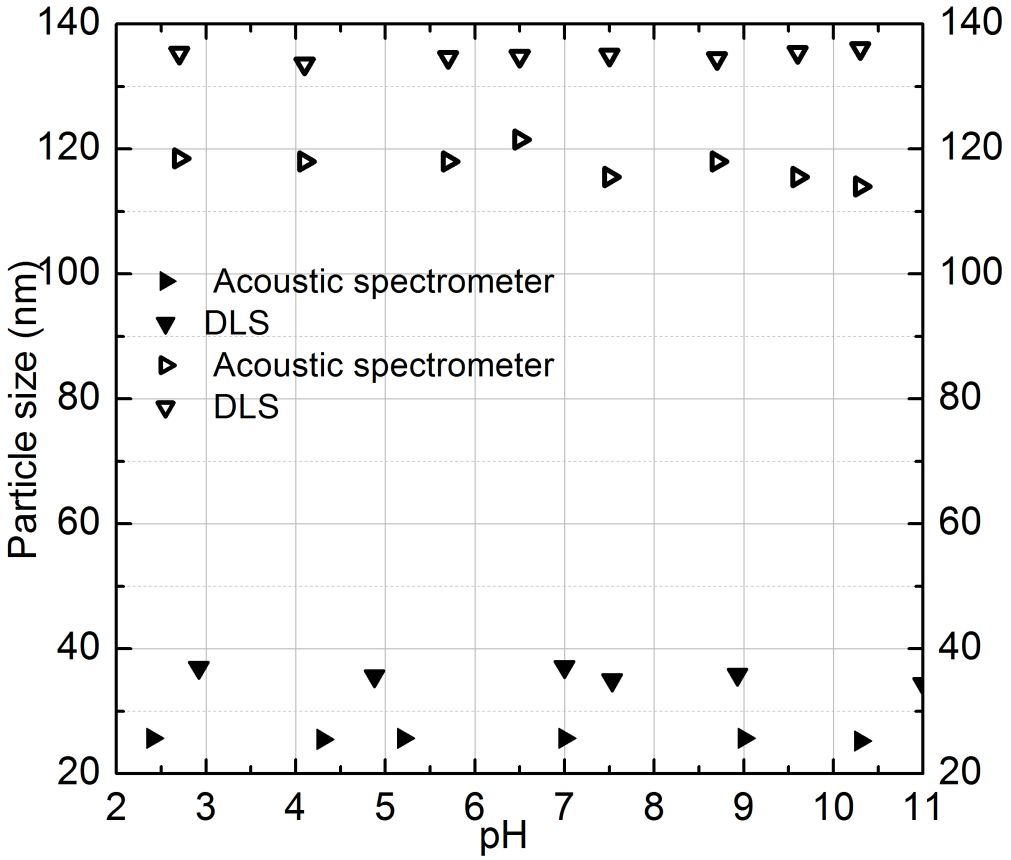

Figure 4.1 – Particle size of model silica colloids: Ludox TM (closed symbols) and Snowtex ZL (open symbols) as a function of pH in 10 mM NaCl solution using DT-1200 Acoustic spectrometer and Dynamic Light Scattering at 25°C

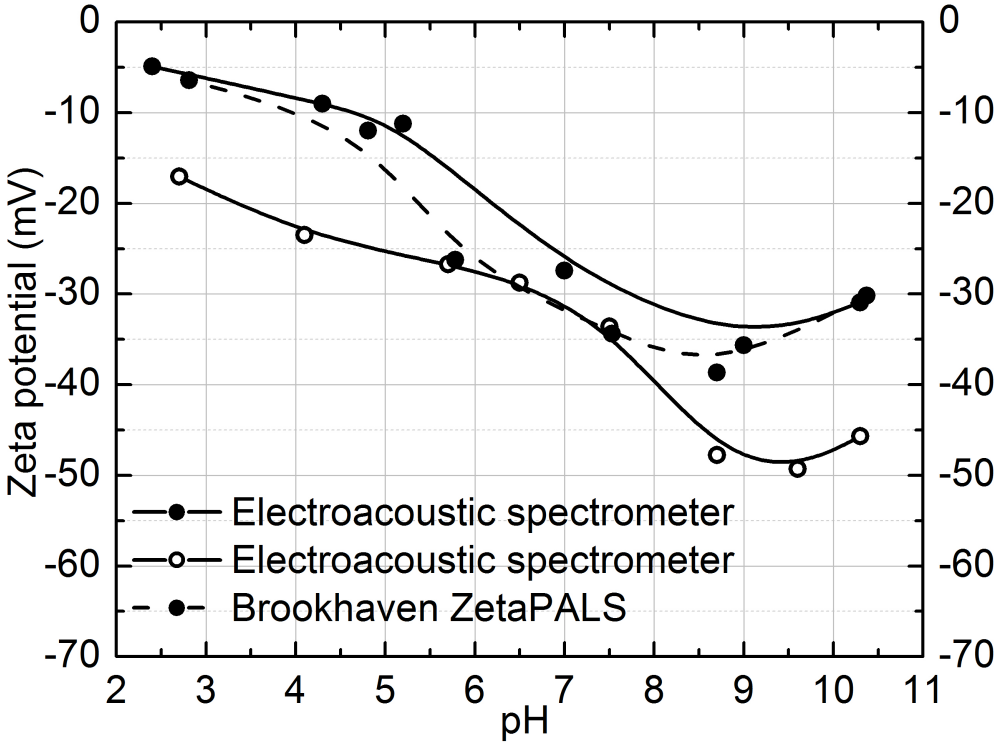

Figure 4.2 – Zeta potential of model silica colloids: Ludox TM (closed symbols) and Snowtex ZL (open symbols), as a function of pH in 10 mM NaCl solution using DT-1200 Electroacoustic spectrometer and Brookhaven ZetaPALS at 25℃. The lines are used as guides.

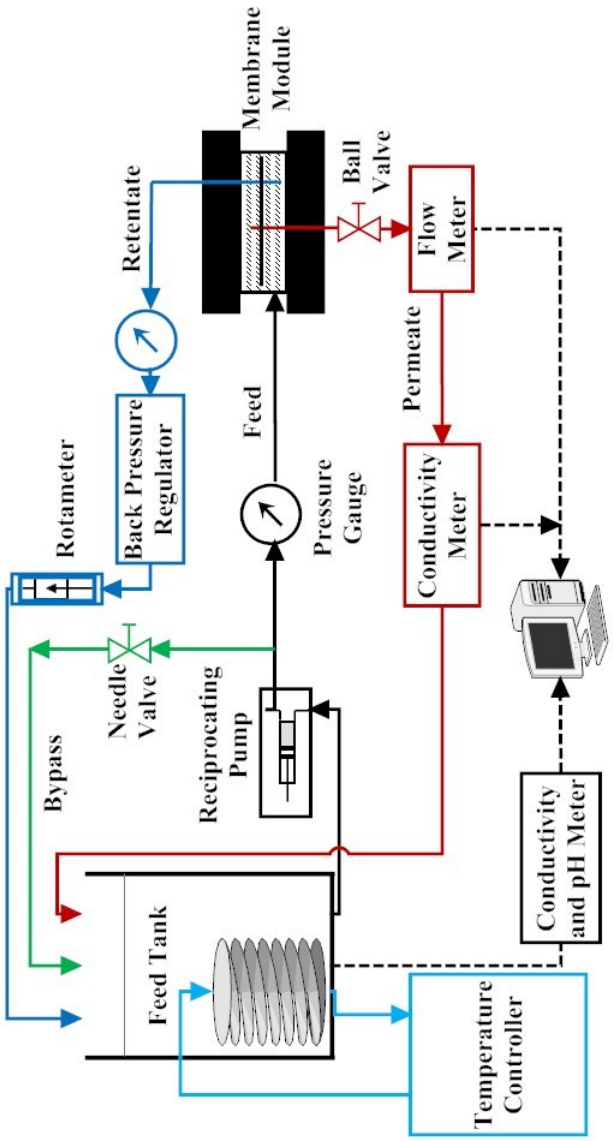

Figure 4.3 – Schematic of cross flow membrane filtration unit

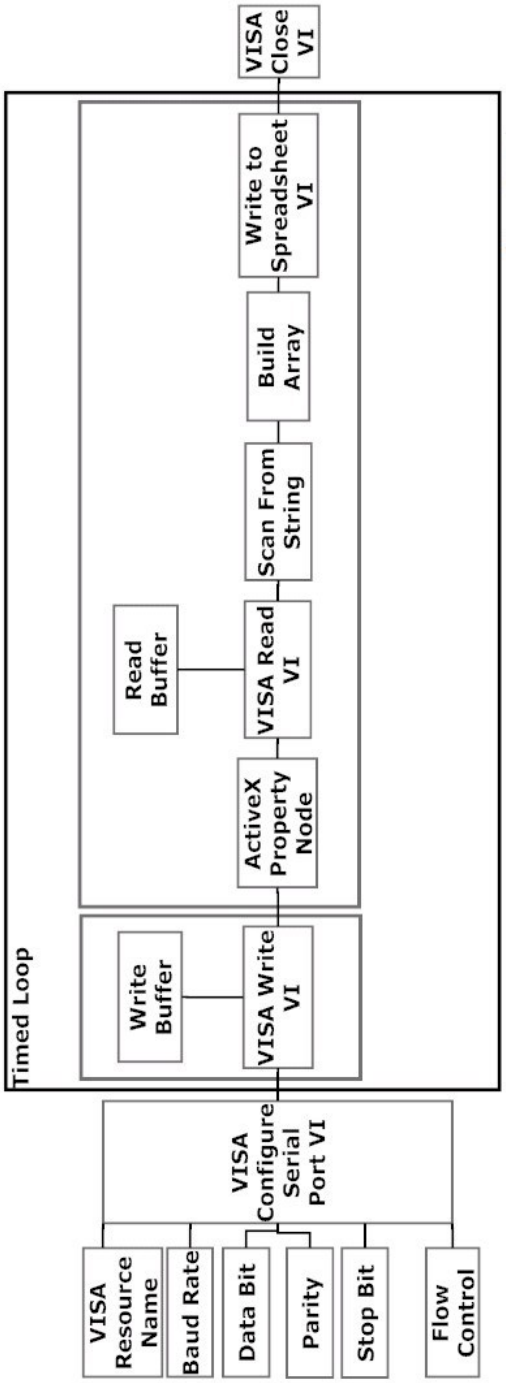

Figure 4.4 – LabVIEW block diagram for data acquisition

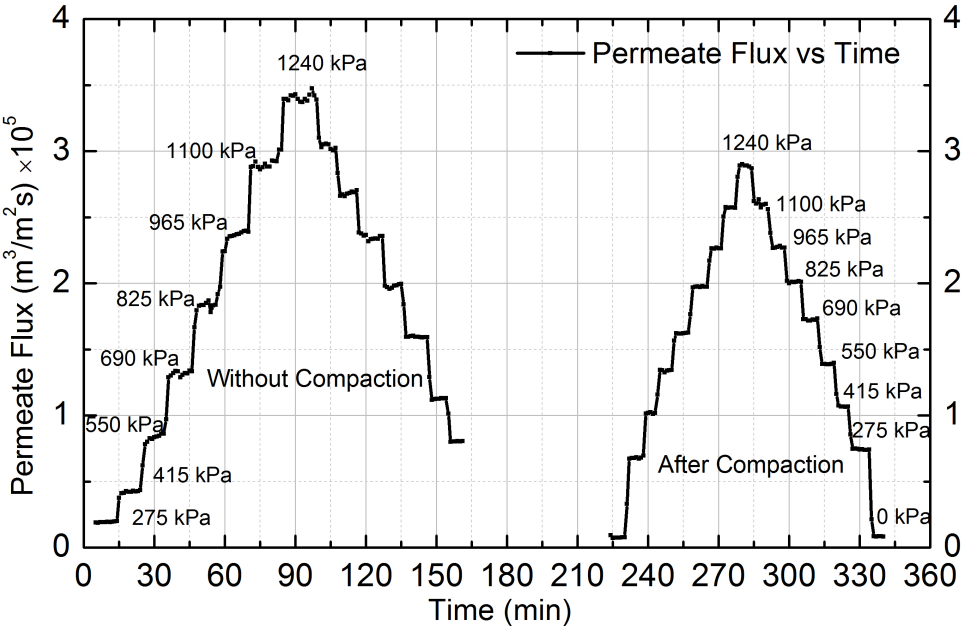

Figure 4.5 – Permeate flux (m^3/m^2s) vs. Time (min.) at different pressure before and after compaction

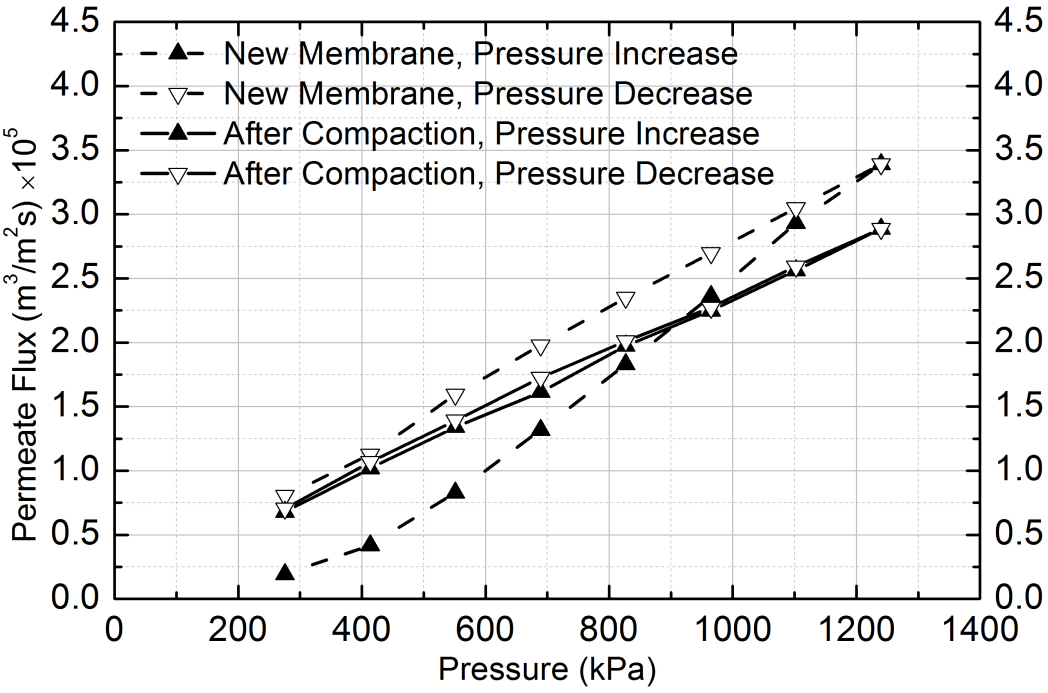

Figure 4.6 – Permeate flux (m^3/m^2s) vs. Pressure (kPa)

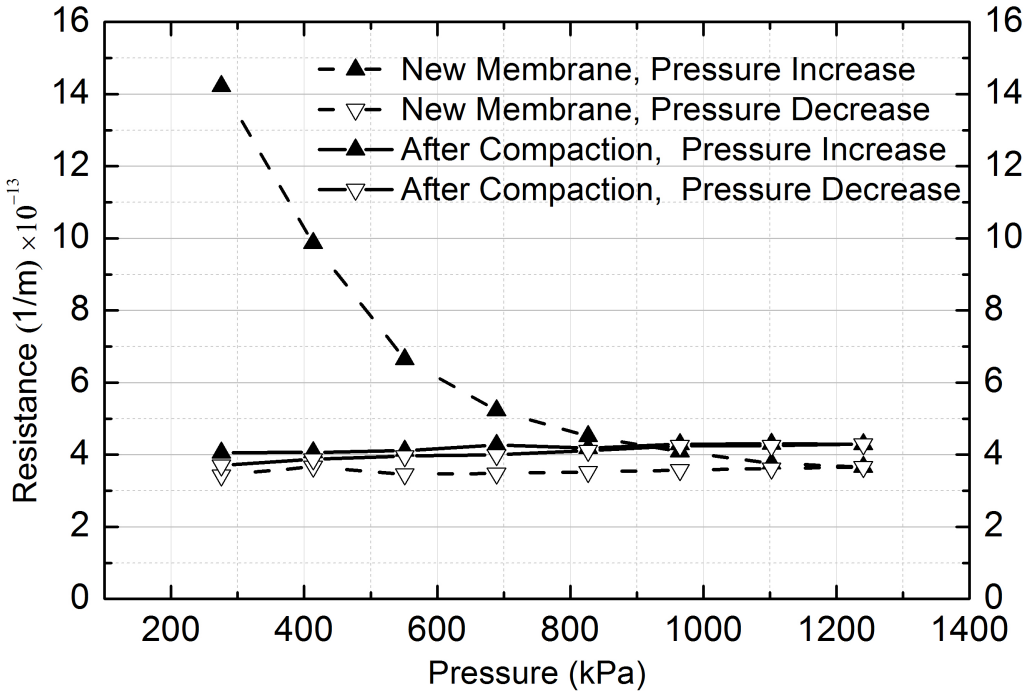

Figure 4.7 – Resistance $(1/m)$ vs. Pressure (kPa)

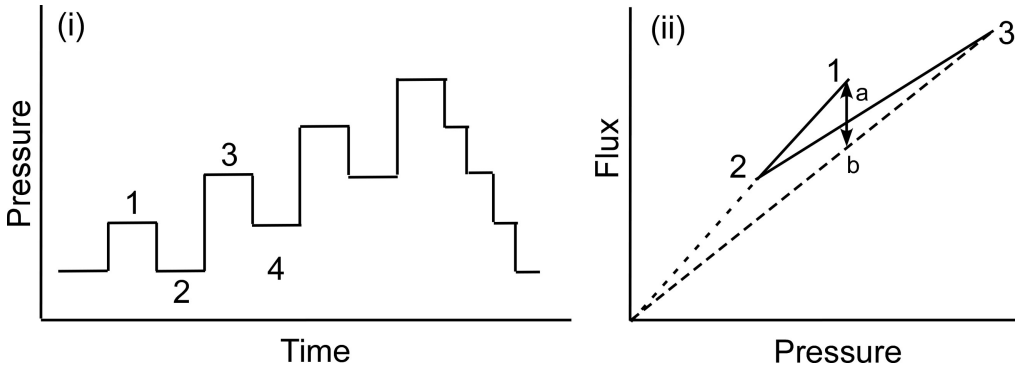

Figure 4.8 – (i) Pressure vs. Time, Pressure step method (ii) Corresponding Flux vs. Pressure, the flux of step 4 is included on segment a-b [Espinasse et al., 2002]

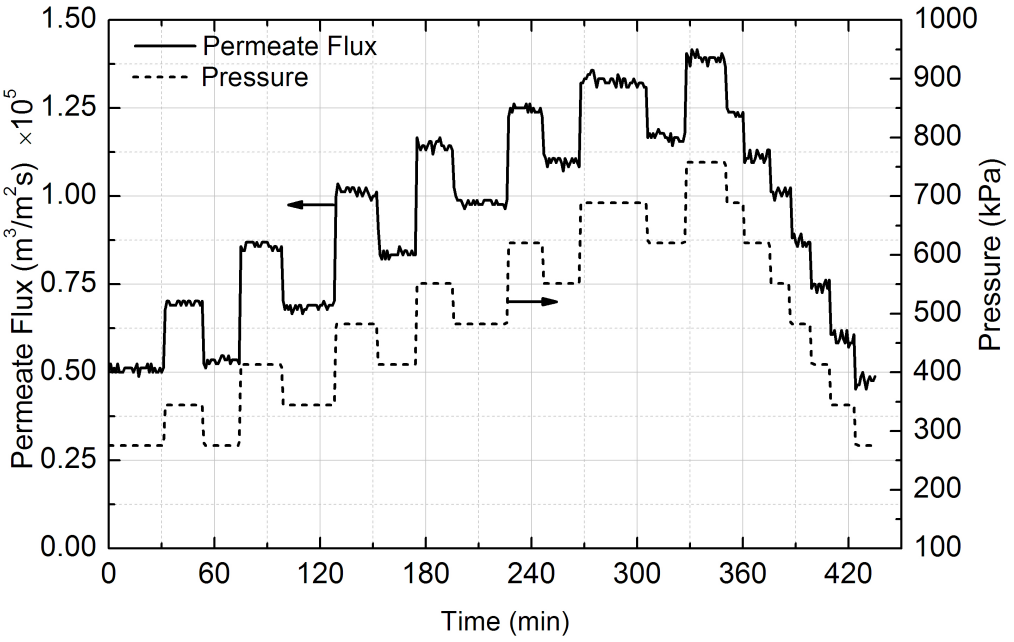

Figure 4.9 – Pressure (kPa) and Permeate Flux (m^3/m^2s) vs. Time (min.) for 100 nm Snowtex ZL colloidal particles in 10 mM NaCl solution. The cross flow velocity was 0.1 ms^{-1} and Reynolds number was 344.

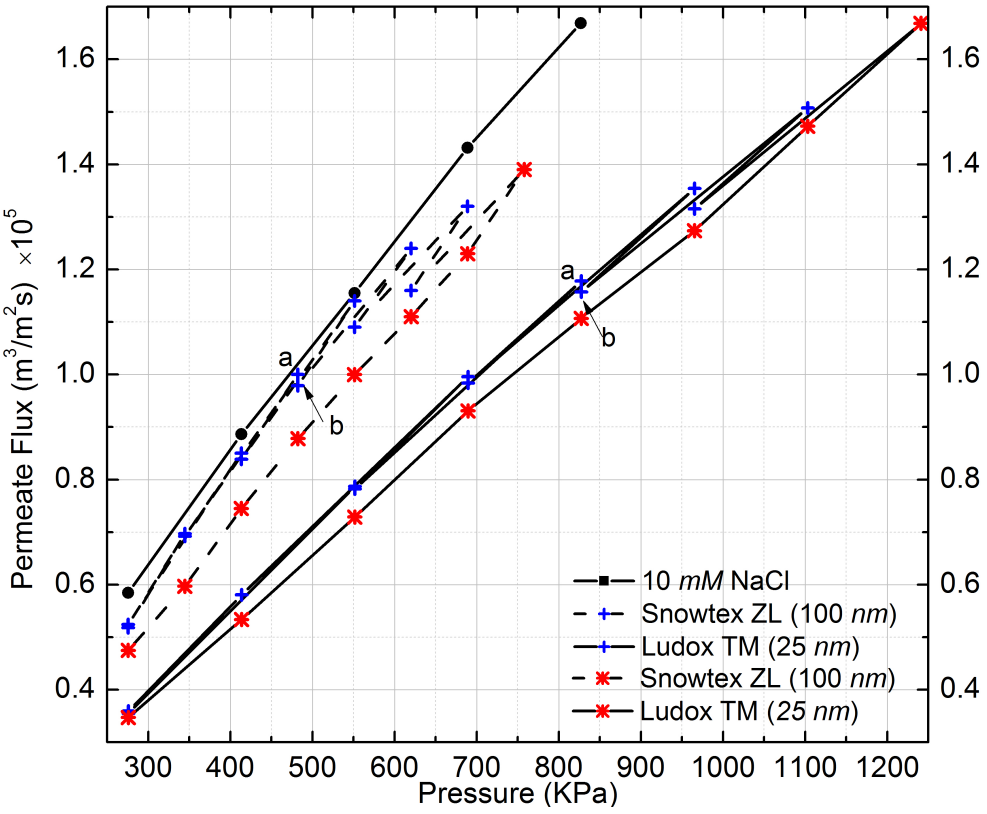

Figure 4.10 – Permeate Flux (m^3/m^2s) vs. Pressure (kPa) for pure water, 10 mM NaCl solution, 300 ppm Snowtex ZL and Ludox TM colloidal particles. The cross flow velocity was 0.1 ms^{-1}. Blue and red symbols represents pressure increase and decrease, respectively.

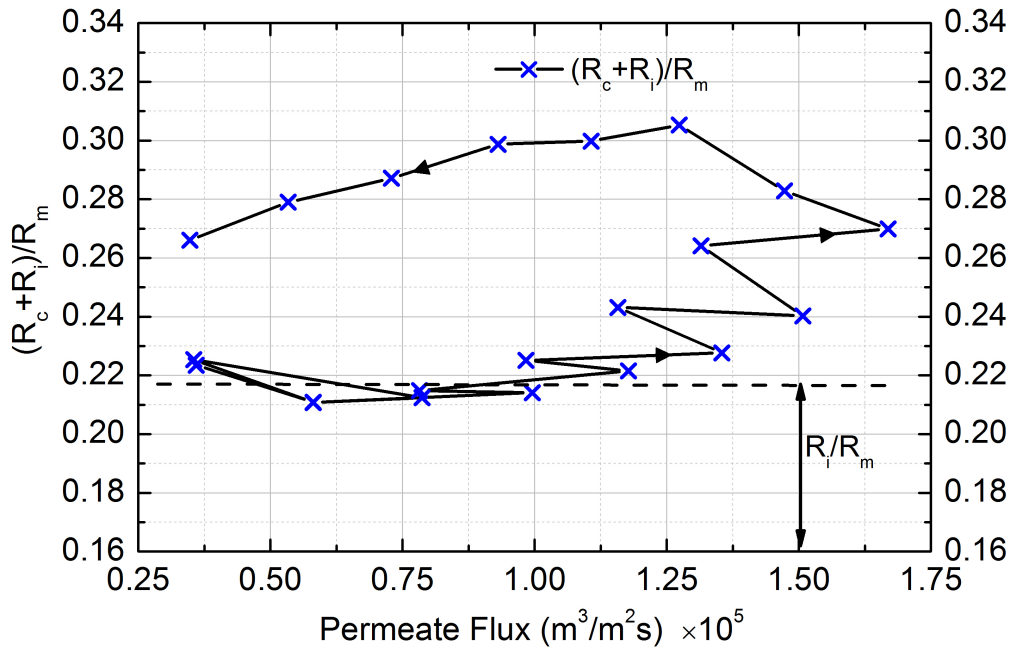

Figure 4.11 – Normalized resistance $((R_c + R_i)/R_m)$ vs. Permeate flux (m^3/m^2s). Evaluation of resistance for Ludox TM colloidal particles during critical flux experiment. The cross flow velocity was 0.1 ms^{-1}.

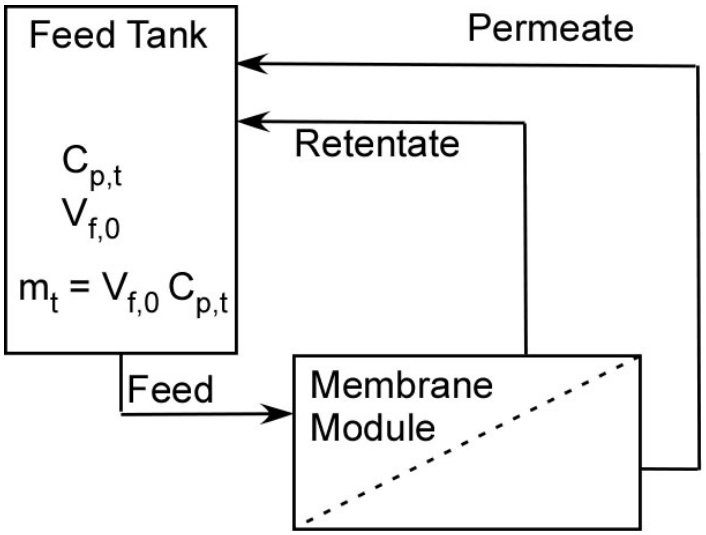

Figure 4.12 – Mass balance of the feed suspension

Chapter 5

Results and Discussion

The primary goals of this chapter are to highlight the key differentiating features of the developed filtration model, and compare the flux decline predicted by the model with controlled cross flow filtration experiments to highlight its accuracy and sensitivity. Accordingly, a brief parametric study of the electroosmotic back flow effect captured by the model is first presented. Following this, comparison of the performance predictions with the experimental results are presented. In this sense, the model and experiments are both tested simultaneously over a wide range of physico-chemical parameters representing cross flow filtration of silica suspensions at different ionic strengths of an indifferent 1:1 electrolyte. The results help establish the ability of the model to describe the combined flux decline owing to colloidal cake formation, as well as the ensuing cake enhanced concentration polarization (CECP). Finally, statistical analysis of model predictions and experimental results were done to estimate the goodness of fit for the model.

5.1 Contribution of electroosmotic back flow

The primary differentiating feature of the present model is that it accounts for an electroosmotic flow across the cake owing to the streaming potential as presented in chapter 3. The importance of the electroosmotic back flow is highlighted here. The electroosmotic back flow due to the presence of charged colloidal particles of cake layer is captured in the parameter g^* (Eq. 3.28) in the developed model. The parameter quantifies this effect in terms of an electroviscous resistance, which is additional to the hydrodynamic resistance of the cake layer. It also directly relates the cake volume fraction (φ_c) and zeta

potential (ψ_p) of particles to the electroviscous resistance. Cake volume fraction depends on salt concentration and zeta potential. The earlier models in literature discussed in section 2.6, also accounted for the electroviscous effects in porous media considering electrolyte transport through narrow capillaries. Influence of volume fraction on the electroviscous effect was neglected in those studies.

Figure 5.1 shows the effect of zeta potential (ψ_p) and cake volume fraction (φ_c) on the pressure drop ratio ($\Delta P_c^*/\Delta P_{c,h}^*$) as a function of κa. This is the ratio of total pressure drop (ΔP_c^*) including the electroviscous effect to the pressure drop ($\Delta P_{c,h}^*$) due only to hydrodynamic resistance of the cake. The influence of ψ_p on pressure drop ratio is shown in Fig. 5.1a for a constant volume fraction of 0.5. The pressure drop ratio exhibits a maximum value with respect to κa for different values of ψ_p. Maximum pressure drop ratio was observed at around κa of 4.0 and the maximum ratio is substantially higher than the unity for larger ψ_p values. Effect of φ_c on pressure drop ratio is shown in Fig. 5.1b for constant zeta potential of -35 mV. As shown in this figure, pressure drop ratio increases with the increase of φ_c and the maximum pressure drop ratio shifts right toward the larger κa values. For example, for random close packing volume fraction of hard spheres (0.64) [Elimelech and Bhattacharjee, 1998], the maximum pressure drop ratio is observed at κa value of 5.5. This indicates that for higher volume fractions, the electroviscous effect becomes important at larger κa values. Hence, electroosmotic back flow is important for denser cake layers having higher zeta potentials for $2< \kappa a <15$. In presence of denser cake layer or higher cake volume fractions, the radius of the outer cell envelope, b, becomes smaller, as $b = a/\varphi_c^{1/3}$. At the same time, the electric double layer (EDL) thickness, κ^{-1}, increases for smaller κa values. Therefore, electroosmotic back flow becomes important when the EDL thickness becomes comparable with the outer cell radius, b. At these two conditions, flow through the interstices of cake layer modifies the ion distribution and creates the electroosmotic back flow. The electroviscous effect can be seen as back flow, engendered by the streaming potential, and aid migration of ions from the membrane surface toward the CP layer across the cake. In other words, this electroosmotic flow can counter the hindered diffusion of ions in the cake layer and reduce the CECP of salt. Therefore, presence of denser and charged cake layer might be able to overcome the negative effect of hindered back diffusion during low salt concentration operation, and improve the

rejection behavior of low salt rejecting membranes.

5.2 Effect of operating parameters on fouling behavior and CECP for NF90 membrane

To investigate the accuracy and sensitivity of the developed model, cross flow filtration experiments were conducted using a colloidal suspension of silica particles in aqueous NaCl by systematically adjusting the operating parameters. The transient flux decline was determined for each experiment over a duration of 5 hrs. Simultaneously, the deposited mass of the cake layer, as well as the observed salt rejection were recorded as a function of time in each experiment. The experiments allow calculation of all the embedded parameters (primarily the cake porosity and the osmotic pressure) used in the model independently. The experiments were conducted at the same pH and temperature, which, for a given colloidal particle size, maintained the particle zeta potential fixed. Five parameters were varied in these experiments, namely, the applied pressure difference, the cross flow velocity, the particle radius, the particle feed concentration, and the salt concentration in the feed. A few of the experiments that will be discussed specifically in this section are listed in Table 5.1.

During the experiment, permeate flux and salt conductivity of the permeate and feed were directly measured at 1 min. intervals. From the conductivity measurement, the observed rejection was calculated. Feed samples were collected at 20-30 min. intervals for UV absorbance measurement. The UV absorbance provided the time dependent silica concentration in the feed tank, which provided the mass deposited on the membrane. The cake layer porosity was calculated from the deposited mass according to the procedure described in section 4.7.2. From the porosity values at different time intervals, the average cake porosity was calculated for each experiment.

In the following subsections, the effects of the five operating parameters are shown individually. In all the plots, the raw experimental data, as well as the experimentally calculated derived parameters will be shown in symbols. The corresponding model predictions will also be superimposed on these experimental plots to depict how the model tracks the experimental trends in each figure. The electrokinetic model considers the colloidal particles as a swarm of non interacting incompressible spherical particles. The particle-particle and

Table 5.1 – Experimental conditions for fouling experiment on NF90 membrane at 25 ± 1℃ and pH=7.0

Experiment	Operating Parameters				
No.	$C_{p,f}$ (ppm)	u_c (m/s)	ΔP (kPa)	$C_{i,f}$ (mM)	a (nm)
1	300	0.1	965	10	100
2	500	0.1	965	10	100
3	500	0.2	965	10	100
4	300	0.1	689	10	100
5	300	0.1	1033.5	20	100
6	100	0.1	689	1	100
7	300	0.1	965	10	50

particle-membrane interactions are not taken into account, hence, the variations of the cake layer porosity are not mechanistically incorporated in the model. The model therefore considers the cake volume fraction or porosity (φ_c, or ε=1-φ_c) as the only constant adjustable parameter, which is obtained as an experimental input. In all experimental results and model predictions, permeate flux has been presented as normalized flux (v_w/v_i) and the time of silica addition is considered as zero. The steady state salt water flux (v_i) and observed rejection (R_o) were obtained by solving Eqs. 3.2, 3.32, 3.43 and 3.44.

5.2.1 Effect of silica concentration

Experimental results and model predictions for two silica concentrations, 300 *ppm* (experiment 1) and 500 *ppm* (experiment 2), are shown in Figs. 5.2 and 5.3, respectively. In Figs. 5.2a and 5.3a, the normalized permeate flux (v_w/v_i), observed rejection (R_o) and deposited mass (M_c) on membrane are depicted. The initial salt water flux was 1.9×10^{-5} m^3/m^2s for both experiments. After 5 hrs. of filtration, the permeate flux decreased by 33% and 36% for 300 *ppm* and 500 *ppm*, respectively, whereas the observed rejection declined about 8% for both. For 500 *ppm* silica concentration, the initial deposition and flux decline rate was higher, and the deposition rate decreased significantly after 3 hrs. The experimental flux was virtually constant after that. This was owing to the fact that the critical flux for particle deposition was attained in this case and cake development was arrested. For the 300 *ppm* concentration, on the other hand, the flux decline continued through the 5 hrs. duration. Thus, at higher feed particle concentrations, the mass deposition rate is faster, as evident from the corresponding experimental plots in Figs. 5.2a and 5.3a.

The formation of the cake is primarily governed by the rate of particle deposition on the membrane, which is driven by the permeation drag. As the cake layer thickness increases, this permeation drag decreases, and eventually reaches a critical limiting value, below which no particles can be convected to the cake surface. This critical flux, although determined experimentally for each run (chapter 4), was not incorporated in the model [Chong et al., 2008]. The critical flux for particle deposition for 500 *ppm* ($1.16 \times 10^{-5}\ m^3/m^2 s$) was attained after 3 hrs., and remained constant thereafter. The model fails to capture this steady state and continues to predict a transient decline past the point when the critical flux has been attained. This is evident in Fig. 5.3a. Thus, although the model provides excellent agreement with experimental flux and observed rejection during the transient stages of flux decline, it fails to capture the attainment of steady state after the limiting flux is attained.

In the present work, cake layer thickness values for 300 *ppm* and 500 *ppm* silica solutions were calculated to be 37 μm and 41 μm, respectively. As the cake layer thickness is very small, about 1% of the hydrodynamic diameter of the channel, the assumption of film theory and constant mass transfer coefficient is reasonable [Hoek et al., 2001]. The average porosity values obtained experimentally for 300 *ppm* and 500 *ppm* were 0.48 and 0.5, respectively. The difference between experiment results and model predictions are mainly due to the absence of particle-particle interaction and critical flux concept in the model to determine the rate of silica deposition.

The relative contribution of cake-enhanced transmembrane osmotic pressure (TMOP) and trans-cake hydrodynamic pressure drop for 300 *ppm* and 500 *ppm* are shown in Figs. 5.2b and 5.3b, respectively. The experimental results were obtained by following the calculation procedure described in section 4.7.2. Normalized trans-cake hydrodynamic pressure was 1.5% of the applied pressure. Due to the growth of the cake layer, the experimental TMOP increased 25% and 28% for 300 *ppm* and 500 *ppm*, respectively. Therefore, cake-enhanced TMOP is the dominant mechanism for permeate flux and observed salt rejection decline. The model captures these mechanisms very accurately during the transient stages of the flux decline.

5.2.2 Effect of cross flow velocity

The experimental results and model predictions for two cross flow velocities, experiments 2 and 3, are shown in Figs. 5.3 and 5.4, respectively. The normalized flux declined by 44% for 0.2 m/s cross flow velocity as compared to 34% for 0.1 m/s. The observed rejection declined 8% for both experiments. The more severe flux decline for 0.2 m/s (experiment 3) may at first appear counter intuitive, because higher cross flow velocity should have led to lower fouling. This is where, the coupling between salt concentration polarization (CP) and cake filtration manifests itself in an interesting manner. At higher cross flow velocities, the salt CP is lower, which results in higher initial permeation drag (2×10^{-5} m^3/m^2s). This causes a more rapid initial colloid deposition, resulting in a more aggressive growth of cake. Furthermore, the critical flux is attained at a much later time in this experiment compared to experiment 2. Thus, keeping all other parameters constant, increasing cross flow velocity increases the initial colloid deposition, aggravates the cake growth, and delays the onset of critical flux governed steady state condition. The total mass deposited in experiment 3 after 5 hrs. is higher, 0.95 g. Therefore, the rate of deposition is mostly governed by the permeation drag, and cross flow velocity seems to have insignificant effect on particle removal from cake surface for the thin cake layers.

The average porosity obtained from experimental mass deposition data was 0.5 and 0.52 for 0.1 m/s and 0.2 m/s, respectively, which were used for model predictions as well. Since the feed salt concentration (10 mM) and subsequently EDL repulsion is same for both experiments, the cake layer porosity is expected to be similar. The reason for slight increase of average porosity for 0.2 m/s can be attributed to the higher porosity of upper layers of deposited cake as it grows [Tung et al., 2008]. Cake layer thickness values were 41 μm and 55 μm for 0.1 m/s and 0.2 m/s cross flow velocities, respectively, after 5 hrs. The model overestimates the observed rejection decline by 10% for both experiments.

Normalized pressure drops due to cake enhanced osmotic pressure (CEOP) and trans-cake pressure drop are shown in Figs. 5.3b and 5.4b. Transmembrane osmotic pressure increased 28% and 35% after 5 hrs. of experiment for 0.1 m/s and 0.2 m/s, respectively. The observed increase of TMOP at

higher cross flow velocity was due to more silica deposition and enhanced hindered diffusivity. The trans-cake pressure drop was very small, less than 2% of applied pressure, compared to TMOP drop for both experiments. Therefore, enhanced TMOP is the dominant mechanism for the performance decline, which is mostly influenced by the deposited mass or thickness of the cake layer.

5.2.3 Effect of operating pressure

To study the effect of operating pressure on initial salt water flux and subsequently on the fouling performance of NF membrane, two experiments (experiments 1 and 4) were considered at two different pressures with the other conditions remaining indentical. Figure 5.5 shows the experimental results and model predictions for experiment 4 at 689 kPa operating pressure. According to Figs. 5.2a and 5.5a, after 5 hrs. of filtration, permeate flux and observed rejection decline was higher by 15% and 4%, respectively, for 965 kPa, as compared to 689 kPa. Higher flux decline at 965 kPa is due to the higher and continuous deposition of silica particle during the 5 hrs. experiment. On the other hand, the rate of silica deposition reached steady state value after 210 min. for 689 kPa as shown in Fig. 5.5a. The steady state mass deposition and permeate flux were 0.37 g and 1.14×10^{-5} m^3/m^2s, respectively, and remained constant.

Based on experiments 1-4, it can be concluded that critical flux for 100 nm silica particles is around $1.15 \pm 0.02 \times 10^{-5}$ m^3/m^2s. Since, the initial salt water flux at 965 kPa was 35% higher compared to 689 kPa and salt concentration was same, it is expected that the average porosity at 689 kPa will be higher. However, the average porosity for both experiments were calculated to be 0.48. Based on critical flux values, silica deposition stops earlier at 689 kPa as compared to 965 kPa and the exerted transmembrane pressure makes the cake layer denser after that, instead of forming new layers as shown in Fig. 5.9. Hence, in addition to salt water flux and deposited mass, critical flux is also a determining parameter for controlling the average porosity of the cake layer. The model prediction of deposited mass, flux and observed rejection decline for constant average porosity of 0.48 are also shown in Fig. 5.5a. The average porosity obtained for 689 kPa experiment is also in good agreement with that reported in literature [Hoek and Elimelech, 2003].

Experimental results and model predictions of normalized pressure drops are shown in Figs. 5.2b and 5.5b for 965 kPa and 689 kPa, respectively. As the amount of silica deposition was higher for 965 kPa, the normalized cake-enhanced TMOP was also higher by 10% compared to 689 kPa. Normalized trans-cake hydrodynamic pressure drops were 1.5% of the operating pressure. Therefore, operating at lower pressure is beneficial for performance of the membrane as it reduces the effect of CEOP considering that the permeate flux will eventually reach steady values after it reaches the critical flux of particle deposition.

5.2.4 Effect of salt concentration

The salt concentration affects the performance of the filtration process by controlling the rate of mass deposition, porosity of cake, and CECP. The rate of mass deposition is mainly governed by the initial salt water flux and silica concentration in the feed. As mentioned before, the porosity of the cake layer also depends on initial permeation drag (salt water flux), deposited mass, critical flux, and salt concentration. In this section, the effect of salt concentration on porosity, flux decline, and CECP will be discussed. In order to study the effect of salt concentration on porosity and CECP, two experiments were considered (experiment 1 and 5) at two different salt concentration (10 mM and 20 mM) having the same initial salt water flux. The operating pressure was set at 1033.5 kPa for 20 mM (experiment 5) to have the same initial salt water flux as experiment 1. Figure 5.6 shows the experimental results and model predictions for 20 mM salt concentration. According to Figs. 5.2a and 5.6a, permeate flux declined 33% and 35% for 10 mM and 20 mM, respectively. The amount of mass deposition was 0.15 g less for 20 mM experiment. The average experimental porosity obtained for 20 mM salt concentration was 0.45, lower then the porosity of 10 mM experiment, 0.48. The observed higher flux decline, even at low mass deposition, is attributed to the denser structure of cake layer as shown in Fig. 5.9 and subsequent enhanced CP at 20 mM. The decrease of porosity at higher salt concentration is due to the reduced electrostatic repulsion at the same permeation drag condition. TMOP increased 25% for both experiments as shown in Fig. 5.2b and 5.6b. The model predictions are in good agreement with experimental results for constant average porosity of 0.45. The model overestimated the normalized flux decline, observed rejection and CEOP, but the predictions were within 10% of experiments.

The electroosmotic effect strongly depends on salt concentration, cake volume fraction and zeta potential. This effect becomes prominent for small κa values in presence of denser and charged cake layer. Hence, experiment 6 (Table 5.1) was conducted with 1 mM NaCl and 100 nm silica particles at pH 7. The resultant κa value was 6.72 and zeta potential of colloidal particles was -35 mV. Figure 5.7 shows the experimental results and model prediction of this experiment. After 5 hrs. of filtration experiment, the permeate flux declined by 5% owing to the 0.2 g silica deposition. Experimental average porosity obtained from the mass deposition data was 0.5. According to the Fig. 5.1a, the corresponding pressure drop ratio is 1.5. Hence, the electroosmotic effect is important for this experimental condition. The model prediction for 0.5 volume fraction are also presented in Fig. 5.7. As the model accounts for the electroosmotic effect, permeate flux and normalized trans-cake hydrodynamic pressure drops match well with the experimental results. The TMOP was also very small, 4% after 5 hrs., due to lower salt concentration and reduced hindered diffusivity caused by the electroosmotic back flow. Therefore, electroosmotic effect is an important phenomenon to reduce the effects of fouling and CECP, and improve the permeate flux and salt rejection during filtration.

5.2.5 Effect of particle size

The properties of colloidal particles such as size and zeta potential affect the filtration performance. To investigate the effect of particle size, experiments were conducted with two different particle sizes of 50 nm and 100 nm, having same zeta potential in a specific solution. The zeta potential of the particles are -35 mV in 10 mM NaCl solution at pH 7. The permeation drag on particles is proportional to the particle radius, according to Eq. 3.4. Figure 5.8, shows the experimental results of 50 nm particles. According to the figure, 15% flux decline was observed during the initial 1 hr and corresponding mass deposition was 0.45 g. The experimental flux became constant after that. This behavior can be explained by the critical flux of 50 nm particle deposition on the cake surface, corresponding to the value of 1.56×10^{-5} m^3/m^2s. The average cake porosity obtained for 50 nm particles was higher, 0.69, as compared to 100 nm particles, 0.45 to 0.52. The increase of porosity can be attributed to the less permeation drag on smaller particles compared to larger particles, which has stronger influence in determining the cake layer porosity compared

to inter particle interactions [Kim et al., 2006].

The contribution of CEOP and cake layer resistance on permeate flux decline is shown in Fig. 5.8b. Comparison of Figs. 5.3b and 5.8b, reveals that contribution of cake layer resistance to permeate flux decline increased for smaller particle compared to larger one. After 2 hrs. of filtration CEOP increased 12% for 50 nm particles as compared to 20% of 100 nm particles. The observed increase in cake pressure drop and decrease in CEOP pressure for smaller particles is due to combined effect of increased specific resistance and porosity of the cake layer [Faibish et al., 1998].

The model predictions for the average porosity of 0.69 do not match with the experimental results. The resultant behavior can be attributed to the absence of particle-particle interaction in the present model. These interactions become progressively important as the colloidal particle size becomes smaller ($<$100 nm). For smaller particles, the interactions give rise to higher osmotic pressure (due to the particles) which further diminish the applied pressure difference. Hence, it was not expected that this model will predict the combined fouling behavior for particles smaller than 100 nm. In accordance with that, most of the experiments were conducted for 100 nm particle size. Incorporation of these interactions to determine the colloid volume fraction in the cake as it grows with time based on suitable models of colloidal interactions in concentrated systems Kim et al. [2006] may improve the predictions of mass deposition and flux decline of the transient electrokinetic model.

5.2.6 Porosities of the cake layers

The experimental flux decline and mass deposition based cake porosity obtained over the filtration time from each fouling experiment is presented in Fig. 5.9. The porosity of 50 nm particles were higher compared to 100 nm particles. In case of 100 nm particles, the porosity varied from 0.53 to 0.43 during all the experiments. As the cake layer porosity of any experiment does not vary significantly from the average value, consideration of constant average porosity over the filtration time simplifies the model for these particles. In addition, for all fouling experiments, the initial porosity was higher and gradually decreased to constant values. However, this should not be the case. Formation of new layers of colloidal particle and subsequent growth of cake

layer would occur when the maximum volume fraction of cake forming particles is attained for one layer. In this regard, the initial porosity should be the minimum. As the cake thickness increases, the upper layers of cake become more porous due to the reduced permeate flux over the filtration time [Tung et al., 2008]. Hence, more precise investigation is required for accurate measurement of cake layer porosity.

5.3 Statistical estimate of goodness of fit

The experiments 1-6 (Table 5.1) were used to statistically estimate the goodness of fit. As mentioned in section 5.2, the average volume fraction obtained from each experiment was used as the constant volume fraction of the corresponding simulation. The model predictions of flux decline (1-$v_w(t)/v_i$), where t is the time at which the experimental and model fluxes are calculated, observed salt rejection (R_o), deposited mass (M_c), and normalized CEOP ($\Delta\pi_m^*$) were plotted against experimental values of these parameters obtained at 2 hrs. and 4 hrs. All of these parameters are shown in Fig. 5.10. These results were then used for statistically comparing the model predictions to the experimental values of flux decline, observed salt rejection, deposited mass, and normalized CEOP. The mean squared error (MSE), root mean squared error (RMSE), correlation coefficient (R), and coefficient of determination (R^2) for these four responses are presented in Table 5.2. All the parameters match experimental data with correlation coefficient (R) of larger than 0.9. The MSE values were calculated using the following equation [Sadrzadeh et al., 2009]:

$$\text{MSE} = \frac{\sum_N (X_M - X_E)}{N} \tag{5.1}$$

where, the subscripts M and E denotes the model prediction and experimental results of different responses (X). The Pearson product-moment correlation coefficients were determined using the following expression [Sadrzadeh et al., 2009]:

$$\text{R} = \frac{\sum_N (X_M - X_{M,avg})(X_E - X_{E,avg})}{\sqrt{\sum_N (X_M - X_{M,avg})}\sqrt{\sum_N (X_E - X_{E,avg})}} \tag{5.2}$$

As observed in Table 5.2, MSE values are in order of $< 10^{-3}$ which implies that the errors are 100 times less than the order of magnitude of the data values. The RMSE is directly interpretable in terms of measurement units, and so is a better measure of goodness of fit than a correlation coefficient. This can be compared to an observed variation in measurement of a typical

Table 5.2 – Statistical criteria for validation of the developed model

Criterion	Response (X)			
	Flux decline, ($1\text{-}v_w/v_i$)	Observed salt rejection, R_o	Deposited silica mass, M_c	Normalized CEOP, $\Delta\pi^*_m$
MSE[a]	1.11×10^{-3}	1.85×10^{-3}	9.34×10^{-3}	8.45×10^{-4}
RMSE[a]	0.033	0.043	0.096	0.029
R	0.959	0.952	0.901	0.965
R^2	0.92	0.906	0.813	0.931

[a] The MSE has the unit of squared of response unit while RMSE has the same unit as response

experimental point. The two should be similar for a reasonable fit. According to RMSE values in Table 5.2, flux decline, observed salt rejection, deposited silica mass and normalized CEOP can be reported with the error of ±3.3%, ±4.3%, ±9.6% and ±2.9%, respectively. The high RMSE for deposited silica mass is attributed to the instrumental error to sense low rate of silica concentration decline in the feed tank during the experiments and to the absence of particle-membrane interaction, particle-particle interaction and critical flux concept in the developed model.

Correlation coefficient (R) indicates the deviation between the experimental and model derived variables, e.g. from independence. Coefficient of determination (R^2) can have only positive values ranging from 1.0 for a perfect correlation down to 0.0 for a complete absence of correlation. The advantage of R is that it provides the positive or negative direction of the correlation. The advantage of R^2 is that it provides a measure of the strength of the correlation [Sadrzadeh et al., 2009]. According to the data presented in Table 5.2, the model shows an acceptable correlation with the experimental trends, although there exists a slight systematic bias in the model to over predict the results.

5.4 Summary

In this chapter, the primary feature of the developed model, contribution of electroosmotic back flow, is presented. Electroosmotic back flow is important for denser and charged cake layer during the low ionic strength operation which

is also evident from the experiment. This reduces the hindered back diffusion and CECP phenomena, and improves the filtration performance. Following this, effect of different operating parameters were experimentally investigated. Simultaneously, the model predictions were compared with experimental results which determined two key limitations of the model, namely, failure to incorporate critical flux and particle-particle interactions to determine the cake porosity and microstructure. However, the model can predict the transient stages of flux decline during the combined fouling experiment by mechanistically coupling the salt CP and transient growth of cake layer. The model considers a constant average porosity obtained from experimental result as the only adjustable parameter. According to the results, operating at higher initial salt flux and silica concentration increases the severity of performance decline of NF process. The porosity of cake layer is controlled by the initial salt flux, salt concentration and deposited mass of cake layer. The model predictions were compared with the experimental results using statistical parameters and were found to be in reasonably close proximity to the experimental results with root mean squared error (RMSE) of lower than 0.1 and correlation coefficient of higher than 0.9.

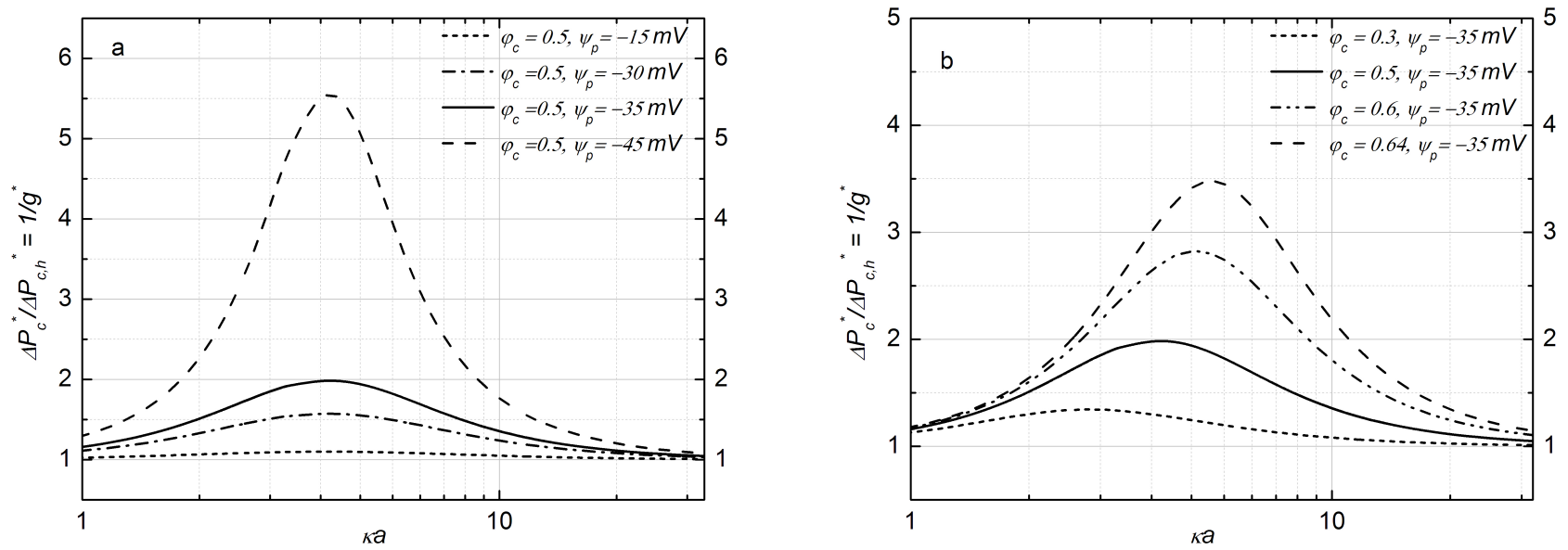

Figure 5.1 – Effect of a) zeta potential (ψ_p) and b) volume fraction (φ_c) on pressure drop ratio ($\Delta P_c^*/\Delta P_{c,h}^*$) as a function of κa.

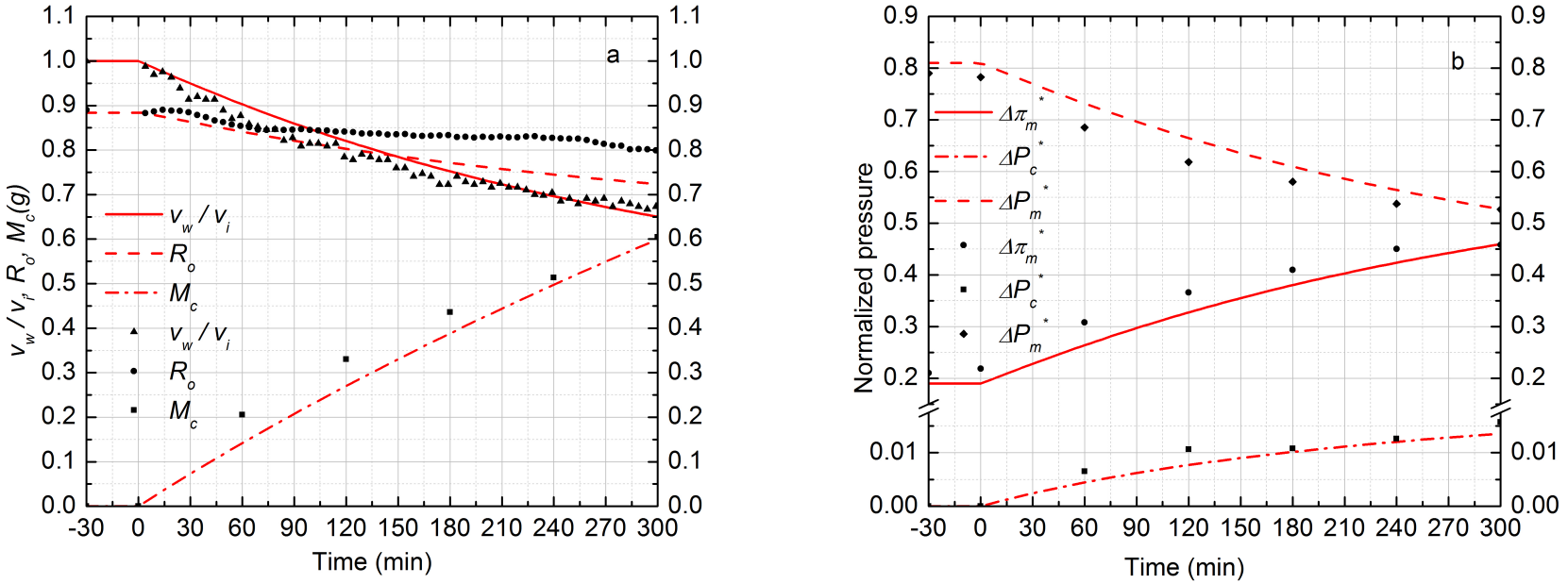

Figure 5.2 – a) Normalized permeate flux (v_w/v_i), Observed rejection (R_o) and Deposited cake mass (M_c) on NF90 membrane. Fouling experiment conducted at 965 kPa, cross flow velocity 0.1 m/s, 10 mM NaCl solution, 300 ppm of 100 nm Silica, temperature of 25℃ and pH 7.0, b) Comparison of normalized trans-membrane pressure ($\Delta {P_m}^*$), trans-cake hydrodynamic pressure ($\Delta {P_c}^*$) and cake-enhanced TMOP ($\Delta {\pi_m}^*$). Symbols and lines represent the experimental results and model predictions, respectively.

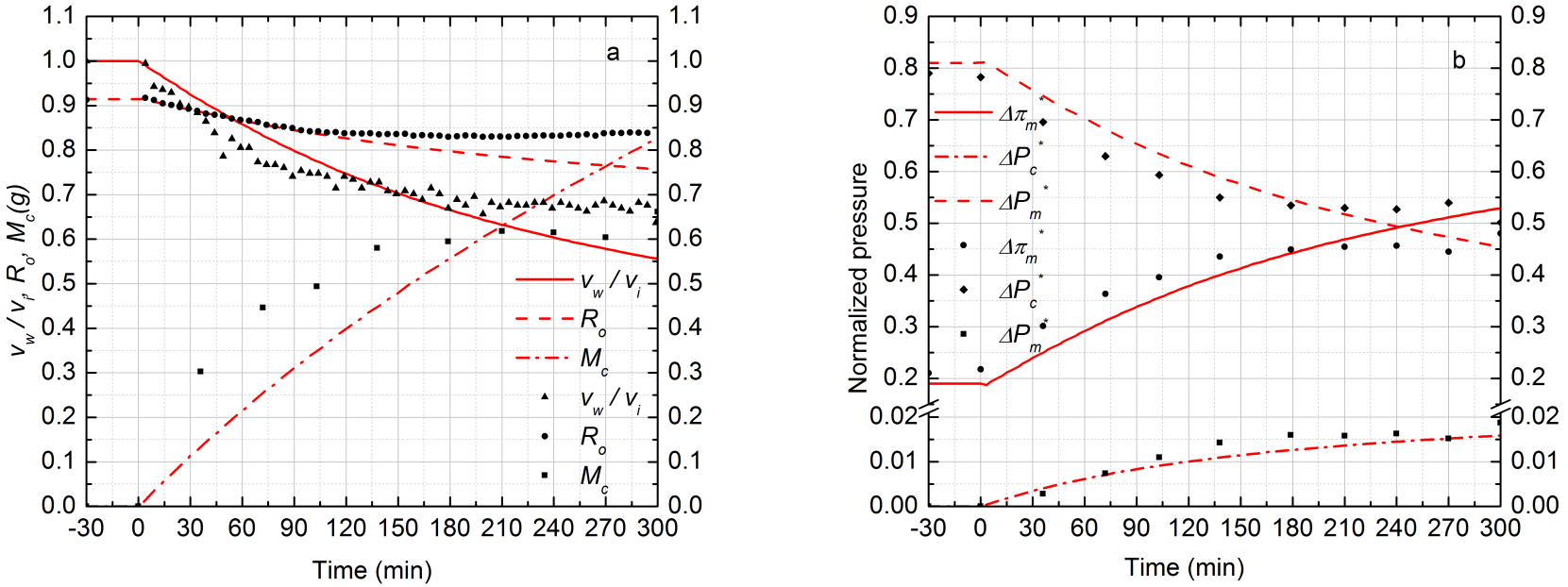

Figure 5.3 – a) Normalized permeate flux (v_w/v_i), Observed rejection (R_o) and Deposited cake mass (M_c) on NF90 membrane. Fouling experiment conducted at 965 kPa, cross flow velocity 0.1 m/s, 10 mM NaCl solution, 500 ppm of 100 nm Silica, temperature of 25℃ and pH 7.0, b) Comparison of normalized trans-membrane pressure ($\Delta P_m{}^*$), trans-cake hydrodynamic pressure ($\Delta P_c{}^*$) and cake-enhanced TMOP ($\Delta\pi_m{}^*$). Symbols and lines represent the experimental results and model predictions, respectively.

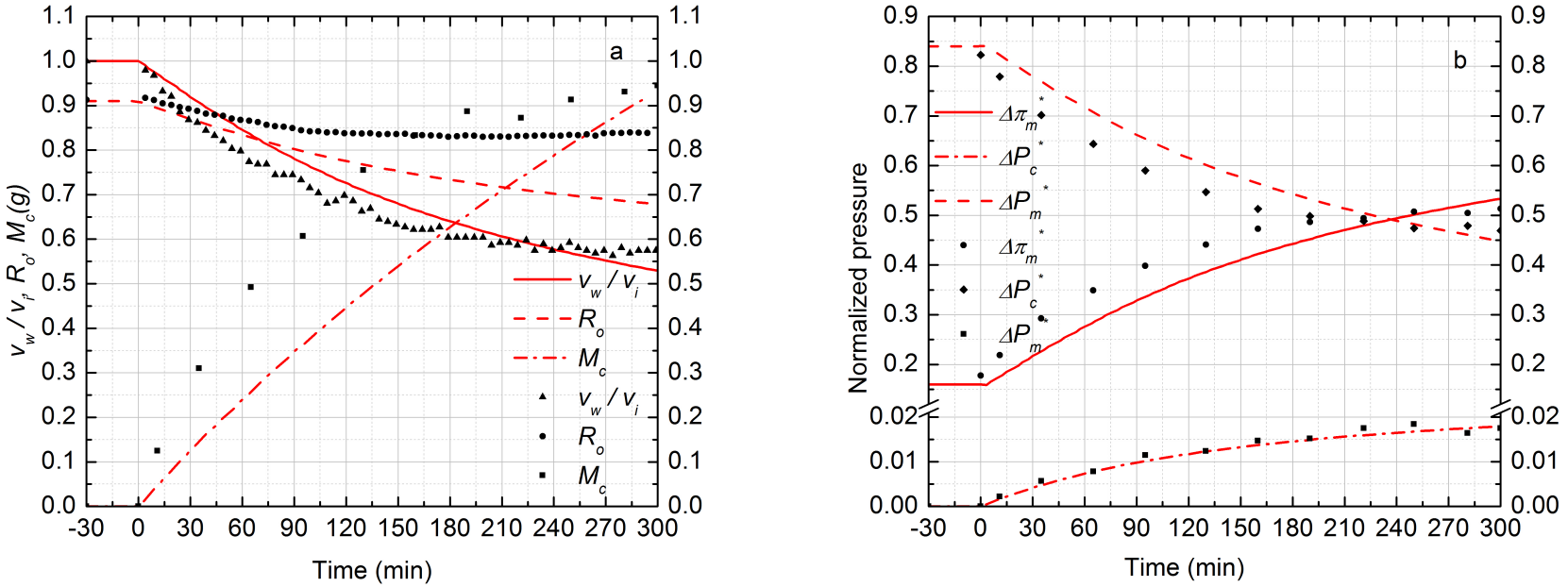

Figure 5.4 – a) Normalized permeate flux (v_w/v_i), Observed rejection (R_o) and Deposited cake mass (M_c) on NF90 membrane. Fouling experiment conducted at 965 kPa, cross flow velocity 0.2 m/s, 10 mM NaCl solution, 500 ppm of 100 nm Silica, temperature of 25℃ and pH 7.0, b) Comparison of normalized trans-membrane pressure ($\Delta P_m{}^*$), trans-cake hydrodynamic pressure ($\Delta P_c{}^*$) and cake-enhanced TMOP ($\Delta\pi_m{}^*$). Symbols and lines represent the experimental results and model predictions, respectively.

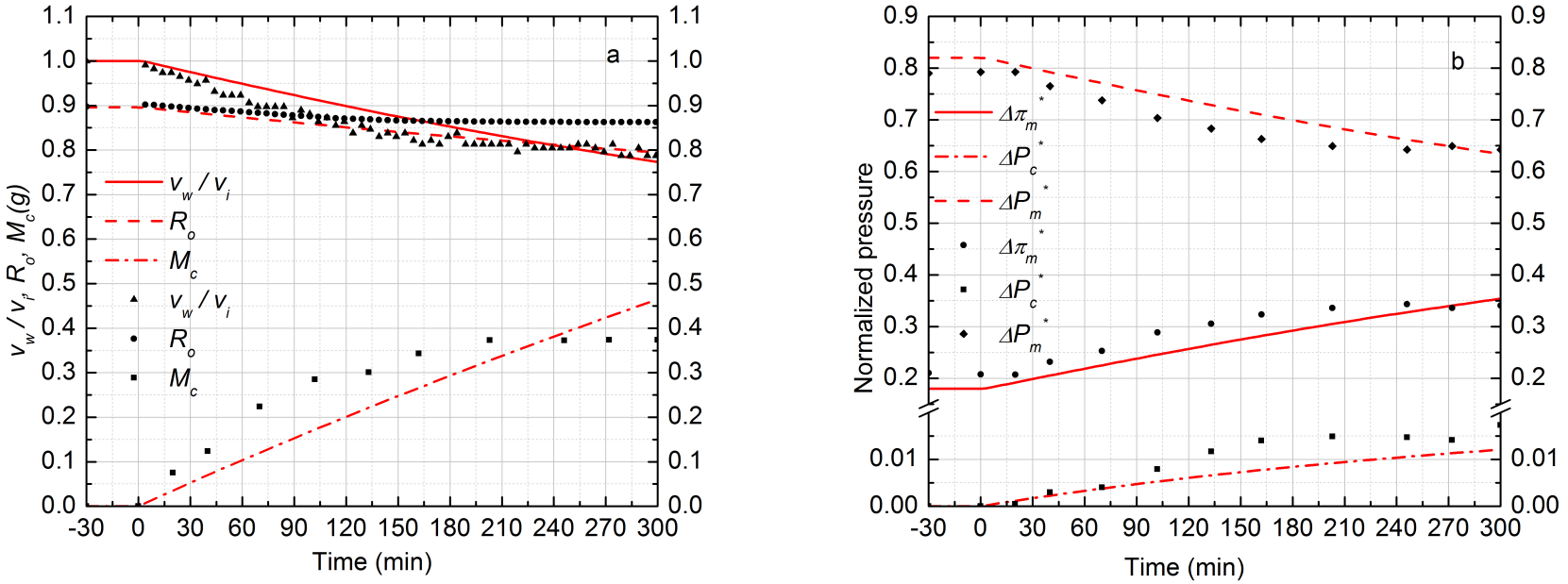

Figure 5.5 – a) Normalized permeate flux (v_w/v_i), Observed rejection (R_o) and Deposited cake mass (M_c) on NF90 membrane. Fouling experiment conducted at 689 kPa, cross flow velocity 0.1 m/s, 10 mM NaCl solution, 300 ppm of 100 nm Silica, temperature of 25℃ and pH 7.0, b) Comparison of normalized trans-membrane pressure ($\Delta P_m{}^*$), trans-cake hydrodynamic pressure ($\Delta P_c{}^*$) and cake-enhanced TMOP ($\Delta\pi_m{}^*$). Symbols and lines represent the experimental results and model predictions, respectively.

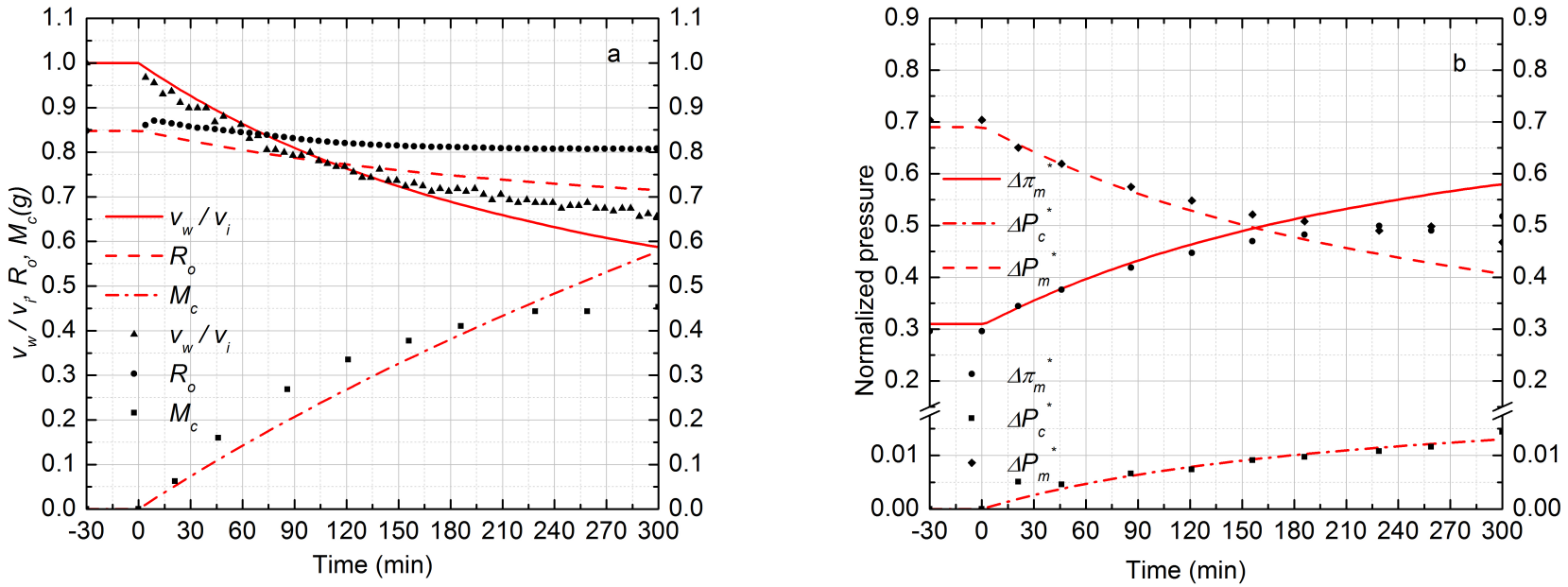

Figure 5.6 – a) Normalized permeate flux (v_w/v_i), Observed rejection (R_o) and Deposited cake mass (M_c) on NF90 membrane. Fouling experiment conducted at 1033.5 kPa, cross flow velocity 0.1 m/s, 20 mM NaCl solution, 300 ppm of 100 nm Silica, temperature of 25℃ and pH 7.0, b) Comparison of normalized trans-membrane pressure ($\Delta P_m{}^*$), trans-cake hydrodynamic pressure ($\Delta P_c{}^*$) and cake-enhanced TMOP ($\Delta\pi_m{}^*$). Symbols and lines represent the experimental results and the electrokinetic model predictions, respectively.

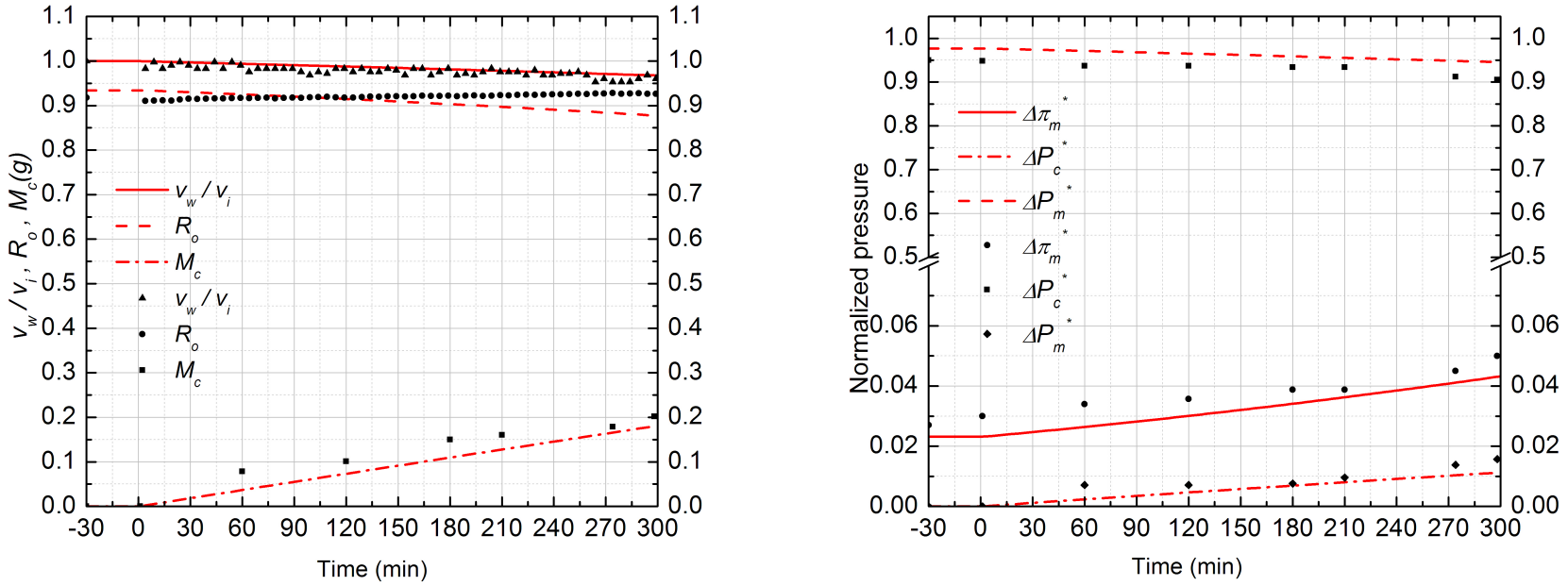

Figure 5.7 – a) Normalized permeate flux (v_w/v_i), Observed rejection (R_o) and Deposited cake mass (M_c) on NF90 membrane. Fouling experiment conducted at 689 kPa, cross flow velocity 0.1 m/s, 1 mM NaCl solution, 100 ppm of 100 nm Silica, temperature of 25℃ and pH 7.0, b) Comparison of normalized trans-membrane pressure ($\Delta P_m{}^*$), trans-cake hydrodynamic pressure ($\Delta P_c{}^*$) and cake-enhanced TMOP ($\Delta\pi_m{}^*$). Symbols and lines represent the experimental results and the electrokinetic model predictions, respectively.

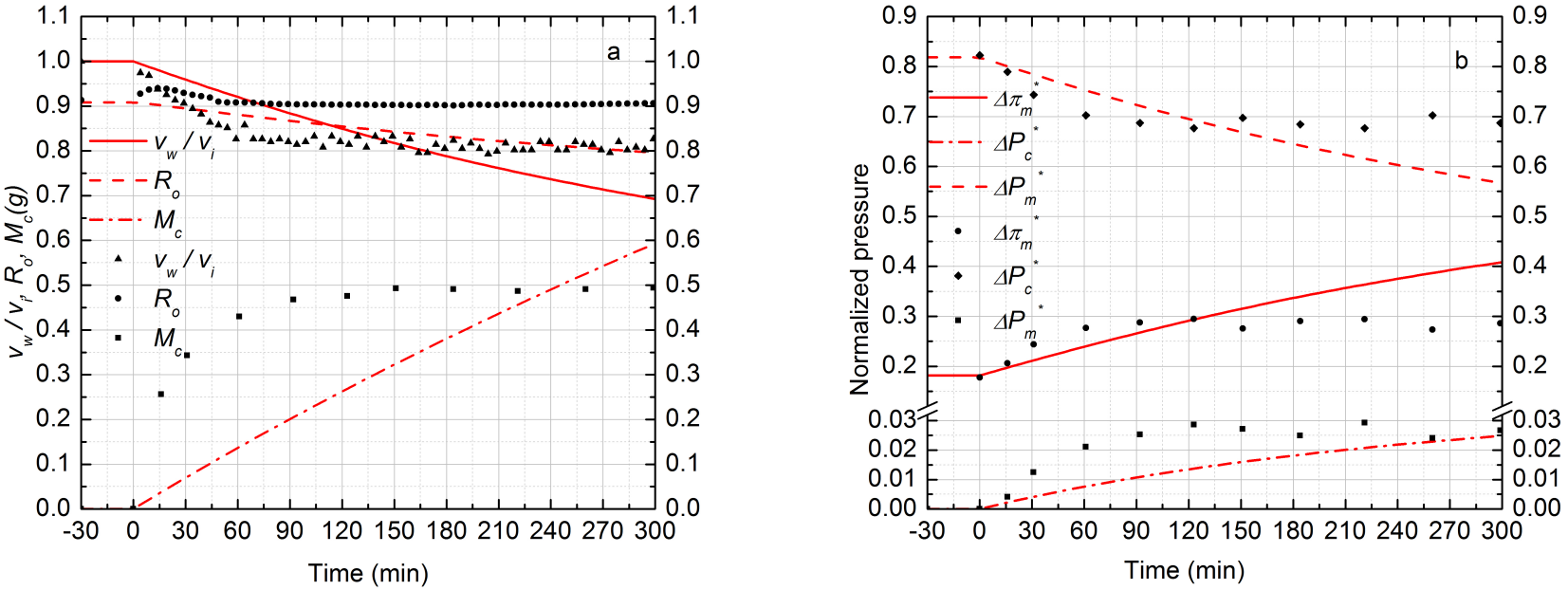

Figure 5.8 – a) Normalized permeate flux (v_w/v_i), Observed rejection (R_o) and Deposited cake mass (M_c) on NF90 membrane. Fouling experiment conducted at 965 kPa, cross flow velocity 0.1 m/s, 10 mM NaCl solution, 500 ppm of 50 nm Silica, temperature of 25℃ and pH 7.0, b) Comparison of normalized trans-membrane pressure ($\Delta {P_m}^*$), trans-cake hydrodynamic pressure ($\Delta {P_c}^*$) and cake-enhanced TMOP ($\Delta {\pi_m}^*$). Symbols and lines represent the experimental results and model predictions, respectively.

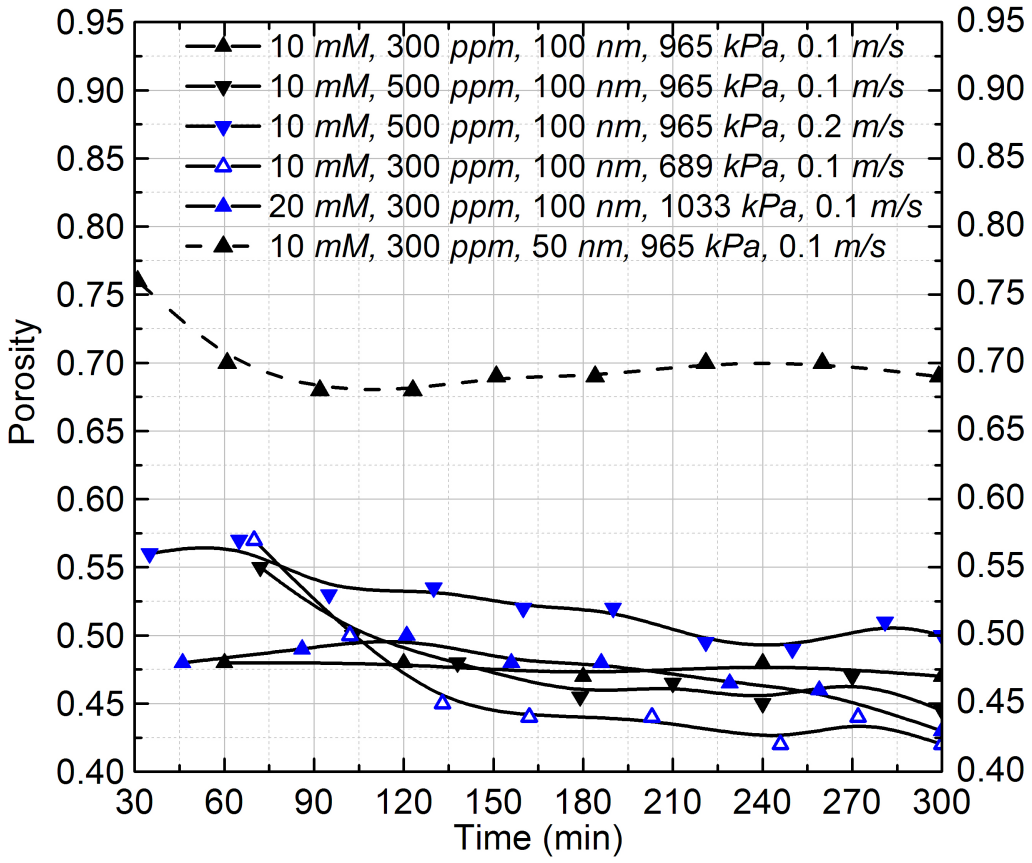

Figure 5.9 – Average cake layer porosity (ε) vs. Time (min.)

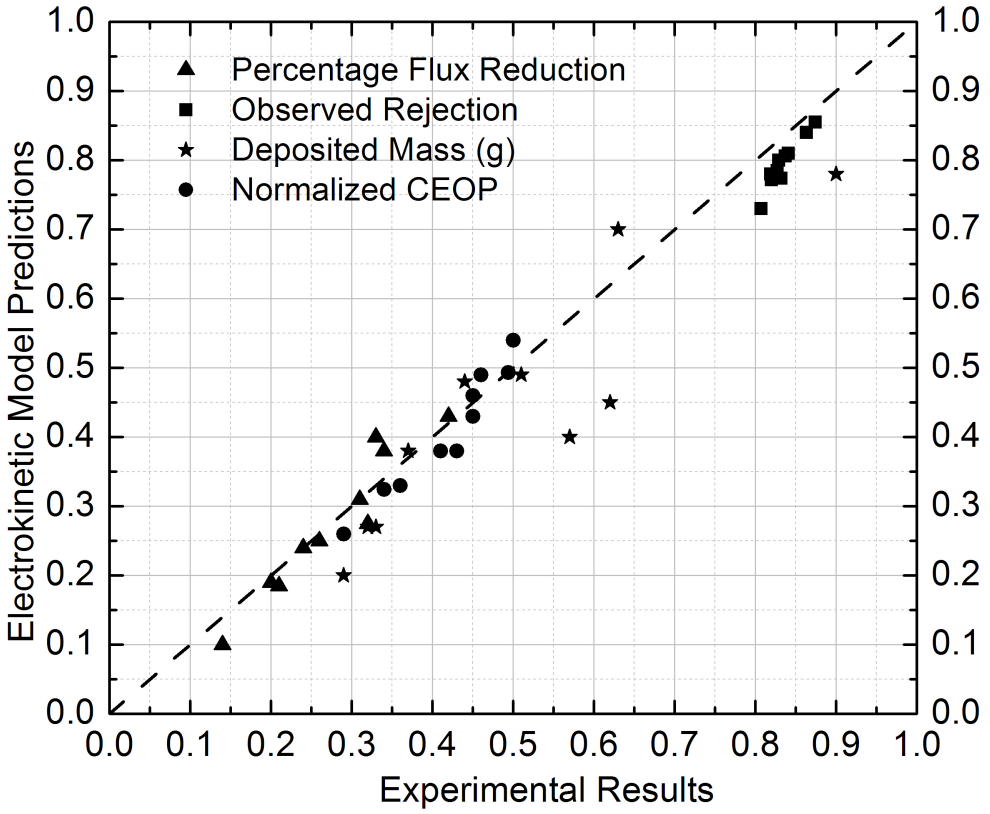

Figure 5.10 – Comparison of electrokinetic model predictions with experimental results at 2 hrs. and 4 hrs.

Chapter 6

Conclusions and Future Work

6.1 Conclusions

This chapter provides the conclusions related to the objectives of the present study. The objectives of the present study were:

1. Develop a dynamic cake layer growth model for colloidal fouling in cross flow membrane filtration process.
2. Incorporate the electroosmotic phenomena related to electrolyte transport through the stationary charged colloidal cake layer.
3. Develop an electrokinetic model to explore the electrolyte transport phenomena within the charged spherical particles of cake layer and explain the CECP mechanism of performance decline in salt rejecting membrane processes.
4. Establish a cross flow membrane filtration setup and methodology of fouling experiment.
5. Validate the transient electrokinetic model with experimental results.

The accomplishments and important conclusions in pursuing the above objective are presented below:

1. A dynamic cake layer growth model has been developed for cross flow filtration process considering 1-D mass transfer using film theory. The assumptions related to the mathematical model were investigated with experimental results. Assumptions were reasonable for predicting the experimental mass deposition and performance decline during the process.

2. Development of electroosmotic flow in presence of electrolyte transport through charged cake layer has been incorporated in the model. The model predictions of increase in pressure drop ratio or apparent viscosity are in good agrement with literature results. The electroosmotic back flow becomes important when the EDL thickness becomes comparable with the outer cell radius. At this condition, flow through the interstices of cake layer modifies the ion distribution and creates the electroosmotic back flow. However, direct measurement of electroosmotic flow during the filtration process is not possible. Therefore, the model allows to predict the electroosmotic effect from the measured quantities of an experiment.

3. Bulk transport of electrolyte through the CP layer and tortuous path of cake layer has been considered in the model to explain the CECP phenomenon. The electrokinetic transport process of ionic species within the charged particles was not incorporated within the present model.

4. These three phenomena were coupled together to develop a process simulator for predicting the performance decline and quantifying the major factors in salt rejecting membrane processes. The model considers the average porosity of cake layer as a fitting parameter instead of considering the particle-particle interactions and measuring the dynamic porosity of cake layer. However, the model is developed in such a manner that the governing equations can be modified to incorporate particle-membrane and particle-particle interactions, multivalent ions, critical flux concept, and dynamic variations of the cake layer porosity.

5. A cross flow filtration setup has been developed to study the membrane filtration processes. The unit allows precise control over wide range of pressures, cross flow velocities and temperatures. Automated data acquisition panel has been developed for advanced data recording during long duration experiments which has access for installation of new instruments as well. The documentation of the unit includes standard operation and maintenance procedure provided in appendix A.

6. The transient electrokinetic model has been validated with experimental results using statistical parameters. The model predictions were in close proximity of the experimental results over the time. The root mean

squared errors (RMSE) were lower than 0.1 and correlation coefficients (R) were higher than 0.9 for different responses.

7. The experimental results and model predictions reveal that operation of the filtration process below the critical flux of particle deposition is beneficial for the process. The dynamic porosity of colloidal cake layer depends on the permeation drag, zeta potential of colloidal particles, deposition rate, and electrolyte concentration.

8. The experimental conditions were not varied over the wide range like the previous literatures to obtain distinguishable variation of the results. However, as shown in section 5.2, the experimental setup is very precise and sensitive for obtaining accurate results even for small variation of conditions. The developed model is also sensitive to major experimental parameters and for predicting accurate results.

6.2 Future work

The transient electrokinetic model developed in this study can be considered as an initial step in the direction of developing a process simulator for colloidal fouling of membrane. Few recommendation for future development of the model and direction of membrane filtration study with the developed setup are listed below:

1. The present model considers the colloidal deposition as a 1-D mass transfer problem in the cross flow channel. However, the colloidal deposition and CP phenomena vary along the length of the cross flow channel. Therefore, the transient model can be further improved by considering 2-D transport in the filtration channel.

2. Further improvement of the model can be done by including the particle-membrane and particle-particle interactions, concept of critical flux and porosity distribution along the cake thickness in cake layer growth model. Incorporation of these phenomena will allow to capture the initial rate of fouling, and steady state flux and rejection phenomena during the later stage of the filtration process more accurately.

3. The electrolyte transport process can be improved by incorporating the electrokinetic transport phenomena of ionic species through the charged

cake layer and membrane pores. Developing an electrolyte transport model through the CP layer, charged cake layer and membrane can be an objective of a specific future study.

4. Online UV absorbance measurement of the feed and retentate using the UV-VIS spectrometer (Varian Carey 50) will facilitate longer duration experiments and enhance the automated data acquisition for fouling experiments.

5. In addition, studying the effect of solution chemistry (divalent ions and pH) and temperature on colloidal fouling behavior, investigating the effect of combined fouling of colloids, organic matter, and salts, studying the performance of membranes for various industrial process streams such as, de-oiled produced water and boiler blow down water filtration, can be other potential areas where the developed filtration setup can benefit scientific studies.

Bibliography

E. W. Allen. Process water treatment in Canada's oil sands industry: II. A review of emerging technologies. *Journal of Environmental Engineering and Science*, 7:499–524, 2008.

P. Bacchin, P. Aimar, and R. W. Field. Critical and sustainable fluxes: Theory, experiments and applications. *Journal of Membrane Science*, 281:42–69, 2006.

P. Banerjee and S. De. Steady state modeling of concentration polarization including adsorption during nanofiltration of dye solution. *Separation and Purification Technology*, 71(1):128–135, 2010.

G. Belfort, R. H. Davis, and A. L. Zydney. The behavior of suspensions and macromolecular solutions in cross flow microfiltration: A Review. *Journal of Membrane Science*, 96:1–58, 1994.

C. Bellona and J. E. Drewes. The role of membrane surface charge and solute physico-chemical properties in the rejection of organic acids by NF membranes. *Journal of Membrane Science*, 249:227–234, 2005.

S. Bhattacharjee and G. M. Johnston. A model of membrane fouling by salt precipitation from multicomponent ionic mixtures in crossflow nanofiltration. *Journal of Environmental Engineering and Science*, 19:399–412, 2002.

S. Bhattacharjee, A. S. Kim, and M. Elimelech. Concentration polarization of interacting solute particles in cross-flow membrane filtration. *Journal of Colloid and Interface Science*, 212:81–99, 1999.

B. P. Boudreau. The diffusive tortuosity of fine-grained unlithified sediments. *Geochimica et Cosmochimica Acta*, 60:3139–3142, 1996.

K. Boussu, A. Belpaire, A. Volodin, C. Van Haesendonck, P. Van der Meeren, C. Vandecasteele, and B. Van der Bruggen. Influence of membrane and

colloid characteristics on fouling of nanofiltration membranes. *Journal of Membrane Science*, 289:220–230, 2007.

W. R. Bowen and F. Jenner. Dynamic ultrafiltration model for charged colloidal dispersions: A Wigner-Seitz cell approach. *Chemical Engineering Science*, 50:1707–1736, 1995a.

W. R. Bowen and F. Jenner. Electroviscous effects in charged capillaries. *Journal of Colloid and Interface Science*, 173:388–395, 1995b.

B. V. der Bruggen and C. Vandecasteele. Flux decline during nanofiltration of organic components in aqueous solution. *Environmental Science and Technology*, 35:3535–3540, 2001.

B. V. der Bruggen, L. Braeken, and C. Vandecasteele. Flux decline in nanofiltration due to adsorption of organic compounds. *Separation and Purification Technology*, 29:23 – 31, 2002.

J. Buffle and G. G. Leppard. Characterization of aquatic colloids and macromolecules. 1. Structure and behavior of colloidal material. *Environmental Science and Technology*, 29:2169–2175, 1995.

J. Buffle, K.J. Wilkinson, S. Stoll, M. Filella, and J. Zhang. A generalized description of aquatic colloidal interactions: The three- colloidal component approach. *Environmental Science and Technology*, 32:2887–2899, 1998.

P. C. Carman. Fluid flow through granular beds. *Transactions of the Institution of Chemical Engineers*, 15:150–166, 1937.

V. Chen, A.G. Fane, S. Madaeni, and I.G. Wenten. Particle deposition during membrane filtration of colloids: Transition between concentration polarization and cake formation. *Journal of Membrane Science*, 125:109–122, 1997.

A. E. Childress and M. Elimelech. Effect of solution chemistry on the surface charge of polymeric reverse osmosis and nanofiltration membranes. *Journal of Membrane Science*, 119:253–268, 1996.

T. H. Chong and A. G. Fane. Implications of critical flux and cake enhanced osmotic pressure (CEOP) on colloidal fouling in reverse osmosis: Modeling approach. *Desalination and Water Treatment*, 8:68–90, 2009.

T. H. Chong, F. S. Wong, and A. G. Fane. Enhanced concentration polarization by unstirred fouling layers in reverse osmosis: Detection by sodium chloride tracer response technique. *Journal of Membrane Science*, 287:198–210, 2007.

T. H. Chong, F. S. Wong, and A. G. Fane. Implications of critical flux and cake enhanced osmotic pressure (CEOP) on colloidal fouling in reverse osmosis: Experimental observations. *Journal of Membrane Science*, 314:101–111, 2008.

A. E. Contreras, A. Kim, and Q. Li. Combined fouling of nanofiltration membranes: Mechanisms and effect of organic matter. *Journal of Membrane Science*, 327:87 – 95, 2009.

S. De and S. Bhattacharjee. Flux decline during cross flow membrane filtration of electrolytic solution in presence of charged nano-colloids: A simple electrokinetic model. *Journal of Colloid and Interface Science*, 353:530–536, 2011.

S. De and P. K. Bhattacharya. Modeling of ultrafiltration process for a two-component aqueous solution of low and high (gel-forming) molecular weight solutes. *Journal of Membrane Science*, 136:57 – 69, 1997.

M. Elimelech and S. Bhattacharjee. A novel approach for modeling concentration polarization in crossflow membrane filtration based on the equivalence of osmotic pressure model and filtration theory. *Journal of Membrane Science*, 145:223–241, 1998.

I. C. Escobar. Chapter 1 An Overview of the Global Water Situation. In I. C. Escobar, , and A. I. Schafer, editors, *Sustainable Water for the Future: Water Recycling versus Desalination*, volume 2 of *Sustainability Science and Engineering*, pages 3 – 5. Elsevier, 2010.

B. Espinasse, P. Bacchin, and P. Aimar. On an experimental method to measure critical flux in ultrafiltration. *Desalination*, 146:91–96, 2002.

R. S. Faibish, M. Elimelech, and Y. Cohen. Effect of interparticle electrostatic double layer interactions on permeate flux decline in crossflow membrane filtration of colloidal suspensions: An experimental investigation. *Journal of Colloid and Interface Science*, 204:77–86, 1998.

Y. Gouellec and M. Elimelech. Calcium sulfate (gypsum) scaling in nanofiltration of agricultural drainage water. *Journal of Membrane Science*, 205: 279 – 291, 2002.

C. Guell and R. H. Davis. Membrane fouling during microfiltration of protein mixtures. *Journal of Membrane Science*, 119:269–284, 1996.

E. M. V. Hoek and M. Elimelech. Cake-Enhanced Concentration Polarization: A New Fouling Mechanism for Salt-Rejecting Membranes. *Environmental Science and Technology*, 37:5581–5588, 2003.

E. M. V. Hoek, S. Hong, and M. Elimelech. Influence of membrane surface properties on initial rate of colloidal fouling of reverse osmosis and nanofiltration membranes. *Journal of Membrane Science*, 188:115–128, 2001.

E. M. V. Hoek, A. S. Kim, and M. Elimelech. Influence of crossflow membrane filter geometry and shear rate on colloidal fouling in reverse osmosis and nanofiltration separations. *Environmental Engineering Science*, 19:357–372, 2002.

E. M. V. Hoek, S. Bhattacharjee, and M. Elimelech. Effect of membrane surface roughness on colloid-membrane DLVO interactions. *Langmuir*, 19: 4836–4847, 2003.

S. Hong, R. S. Faibish, and M. Elimelech. Kinetics of permeate flux decline in crossflow membrane filtration of colloidal suspensions. *Journal of Colloid and Interface Science*, 196:267–277, 1997.

J. A. Howell. Sub-critical flux operation of microfiltration. *Journal of Membrane Science*, 107:165–171, 1995.

A. S. Kim, A. E. Contreras, Q. Li, and R. Yuan. Fundamental mechanisms of three-component combined fouling with experimental verification. *Langmuir*, 25:7815–7827, 2009.

S. Kim and E. M. V. Hoek. Modeling concentration polarization in reverse osmosis processes. *Desalination*, 186:111–128, 2005.

S. Kim, M. Marion, B. H. Jeong, and E. M. V. Hoek. Crossflow membrane filtration of interacting nanoparticle suspensions. *Journal of Membrane Science*, 284:361 – 372, 2006.

S. Kuwabara. The forces experienced by randomly distributed parallel circular cylinders or spheres in a viscous flow at small reynolds numbers. *Journal of the Physical Society of Japan*, 14:527–532, 1959.

A. Leveque. Les lois de la transmission de chaleur par convection. *Annales des Mines*, 13:201 299, 1928.

S. Levine and G. H. Neale. The prediction of electrokinetic phenomena within multiparticle systems. I. Electrophoresis and electroosmosis. *Journal of Colloid And Interface Science*, 47:520–529, 1974.

S. Levine, R. Marriott, G. H. Neale, and N. Epstein. Theory of Electrokinetic Flow in Fine Cylindrical Capillaries at High Zeta-Potential. *Journal of Colloid And Interface Science*, 52:136–149, 1975.

N. Li, A. G. Fane, S. Winston Ho, and T. Matsuura, editors. *Advanced Membrane Technology and Applications*. John Wiley & Sons, Inc., 2008.

Y. Li and C. W. Park. Permeability of Packed Beds Filled with Polydisperse Spherical Particles. *Industrial and Engineering Chemistry Research*, 37: 2005–2011, 1998.

C. J. Lin, S. Shirazi, and P. Rao. Mechanistic Model for $CaSO_4$ Fouling on Nanofiltration Membrane. *Journal of Environmental Engineering*, 131:10, 2005.

R. S. Maier, L. R. Petzold, and W. Rath. Using DASPK on the TMC CM5. Experiences with two programming models . In *Scalable Parallel Libraries Conference, 1993., Proceedings of the*, pages 174 –182, oct 1993.

A. D. Marshall, P. A. Munro, and G. Tragardh. The effect of protein fouling in microfiltration and ultrafiltration on permeate flux, protein retention and selectivity: A literature review. *Desalination*, 91:65 – 108, 1993.

J. Masliyah and S. Bhattacharjee. *Electrokinetic and Colloid Transport Phenomena*. John Wiley and Sons, Inc., 2006.

S. Mattaraj, C. Jarusutthirak, C. Charoensuk, and R. Jiraratananon. A combined pore blockage, osmotic pressure, and cake filtration model for crossflow nanofiltration of natural organic matter and inorganic salts. *Desalination*, 274:182–191, 2011.

M. Mulder. *Basic Principles of Membrane Technology*. Kluwer Academic, 1997.

H. Ohshima. Electrophoretic Mobility of Spherical Colloidal Particles in Concentrated Suspensions. *Journal of Colloid and Interface Science*, 188:481 – 485, 1997.

L. R. Petzold. Description of dassl: A differential/algebraic system solver. pages 430–432, 1982.

C. L. Rice and R. Whitehead. Electrokinetic flow in a narrow cylindrical capillary. *Journal of Physical Chemistry*, 69(11):4017–4024, 1965.

T. Rizwan. *Colloidal particle deposition onto charge-heterogeneous substrates*. PhD thesis, University of Alberta, 2009.

T. Rizwan and S. Bhattacharjee. Initial Deposition of Colloidal Particles on aRough Nanofiltration Membrane. *The Canadian Journal of Chemical Engineering*, 85:570–579, 2007.

M. Sadrzadeh, A. Ghadimi, and T. Mohammadi. Coupling a mathematical and a fuzzy logic-based model for prediction of zinc ions separation from wastewater using electrodialysis. *Chemical Engineering Journal*, 151:262–274, 2009.

A. I. Schafer, N. Andritsos, A. J. Karabelas, E. M. V. Hoek, and R. Schneider. *Nanofiltration Principles and Applications*. Elsevier, 2004.

B. Schafer and H. Nirschl. Distinction between Electrostatic and Electrokinetic Effects on the Permeability of Colloidal Packed Beds. *Chemical Engineering & Technology*, 28:862–866, 2005.

B. Schafer and H. Nirschl. Electrohydrodynamic transport in nanoporous packed beds. *Chemical Engineering Science*, 65:6320 – 6326, 2010.

S. Shirazi, C. J. Lin, S. Doshi, S. Agarwal, and P. Rao. Comparison of fouling mechanism by $CaSO_4$ and $CaHPO_4$ on nanofiltration membranes. *Seperation Science and Technology*, 41:2861–2882, 2006.

L. N. Sim, Y. Ye, V. Chen, and A. G. Fane. Investigations of the coupled effect of cake-enhanced osmotic pressure and colloidal fouling in RO using crossflow sampler-modified fouling index ultrafiltration. *Desalination*, 273 (1):184 – 196, 2011.

L. Song and M. Elimelech. Theory of concentration polarization in crossflow filtration. *Journal of the Chemical Society, Faraday Transactions*, 91:3389–3398, 1995.

C. Y. Tang, T. H. Chong, and A. G. Fane. Colloidal interactions and fouling of NF and RO membranes: A review. *Advances in Colloid and Interface Science*, 164:126–143, 2011.

M. Taniguchi, J.E. Kilduff, and G. Belfort. Modes of natural organic matter fouling during ultrafiltration. *Environmental Science and Technology*, 37: 1676–1683, 2003.

K. L. Tung, Y. L. Li, K. J. Hwang, and W. M. Lu. Analysis and prediction of fouling layer structure in microfiltration. *Desalination*, 234:99–106, 2008.

S. L. Walker, S. Bhattacharjee, E. M. V. Hoek, and M. Elimelech. A novel asymmetric clamping cell for measuring streaming potential of flat surfaces. *Langmuir*, 18:2193–2198, 2002.

F. Wang and V. V. Tarabara. Coupled effects of colloidal deposition and salt concentration polarization on reverse osmosis membrane performance. *Journal of Membrane Science*, 293:111–123, 2007.

E. Wigner and F. Seitz. On the constitution of metallic sodium. *Physical Review*, 43:804–810, May 1933.

Y. Yaun and J. E. Kilduff. Effect of colloids on salt transport in cross fow nanofiltration. *Journal of Membrane Science*, 346:240–249, 2010.

W. Yuan, A. Kocic, and A. L. Zydney. Analysis of humic acid fouling during microfiltration using a pore blockage-cake filtration model. *Journal of Membrane Science*, 198:51–62, 2002.

S. K. Zaidi and A. Kumar. Experimental analysis of a gel layer in dead-end ultrafiltration of a silica suspension. *Desalination*, 172:107 – 117, 2005.

X. Zhu and M. Elimelech. Colloidal fouling of reverse osmosis membranes: Measurements and fouling mechanisms. *Environmental Science and Technology*, 31:3654–3662, 1997.

Appendix A

Standard Operating Procedure for Membrane Filtration Experiment

The objective of this project is to develop a standard and scientific operating procedure to conduct fouling study of membrane filtration process. The purpose of producing this document is to provide a process flow for a new student to work with on their own thesis project without having to reinvent the process flow themselves.

A.1 Health, safety and environment

This procedure involves working with high pressure system which can be dangerous if not operated correctly. Therefore, working with the setup requires PPE (personal protective equipment) like safety goggles, lab coat, hand gloves and shoe. Ear muff can be used based on individuals requirement. This does not include any other protective equipment required for specific usage. This document simply provides a flow chart what must be followed by any individual interested in membrane process. Chemicals, if used, must be disposed according to CCF lab protocols.

A.2 Workflow/Methodology

The methodology contains the following steps:

1. Preparation of membrane sample
2. Start up

3. Membrane Compaction
4. Set up to the operating condition/pure water flux
5. Salt addition and equilibration
6. Silica addition and fouling experiment
7. Setup cleaning
8. Measurement of UV absorbance of feed sample
9. Particle concentration measurement

A.3 Procedure

A.3.1 Preparation of membrane sample

1. Take a membrane and cut it to proper shape using the model sample.
2. Make four holes at proper positions to align the membrane at guide posts.
3. Bring out the SEPA CF Cell from hydraulic jack chamber and remove upper part.
4. Install any shim, if needed, to change the cross flow channel height. Without any shim the height of the channel is 1.73 mm, check the manual for the relevant shim size and channel height.
5. Place the feed spacer, if needed, to reduce the intensity of fouling. Different feed spacers are available such as high foulant, medium foulant and low foulant.
6. Put the membrane facing upside (active layer) down and place the permeate carrier on the permeate side. Without the permeate carrier the permeate flow rate will decrease substantially.
7. Place the upper part and return the SEPA CF Cell into the hydraulic jack chamber.

Note:

- Be careful while making holes. If the holes are not in proper place effective membrane area of permeation will decrease.
- Be careful about the o-ring. If they are not in proper place, they will be damaged and will cause leaking.

A.3.2 Start up

1. Jack the hydraulic pressure to above 700 psi (should be three times higher than the maximum compaction pressure).
2. Install the Cole-parmer flow meter at permeate line and complete permeate return line to the tank.
3. Completely open the back pressure regulator and by pass valve.
4. Place the conductivity probe inside the conductivity chamber and pour 9 L of demineralized water in to the feed tank.
5. Start the pump, temperature controller and slowly increase the pressure in step wise manner.
6. Set the temperature of temperature controller to 22℃ to obtain constant feed temperature of 25±1℃.
7. Set the operating pressure to membrane compaction pressure (1.5 times of operating pressure) and maintain the cross flow velocity at 1 LPM.
8. Place a beaker on the weighing balance and keep the permeate line to beaker closed and allow permeate to return back to the tank.
9. Start the LabVIEW data acquisition which is collecting data from the digital flow meter, conductivity meter and weighing balance.
10. Bleed the trapped air three times from the digital flow meter so that no air is trapped inside the meter and each time after bleeding close the valve before the flow meter then open slowly again. When the valve is closed the meter should give zero reading, otherwise tare the flow meter keeping the valve closed. Closing and opening of the valve, and bleeding the flow meter will allow to remove any trapped air within the flow meter.

11. Open the drain line to the beaker and measure the weight to cross check the flow meter reading. If the flow meter reading is within ±1 then close the drain line and let permeate to return back to the tank. Unless repeat step 10 again.

Note:

- If the digital flow meter is not tarred properly, it will not give accurate value.
- If the flow rate is fluctuating, back pressure regulator (BPR) is not being able to control the pressure and flow rate, change the o-ring inside the BPR.
- Do not increase the pressure quickly. Allow the pressure gauge and BPR regulator to respond to the change. In the case of quick change of pressure, the o-ring inside the BPR can be lifted from the position and BPR might not work properly.

A.3.3 Membrane compaction

1. After setting the compaction pressure, allow the membrane to be compacted for 2 hrs.

A.3.4 Set up to the operating condition

1. Set the operating pressure and cross flow velocity to the desired value by controlling BPR and by pass valve. Control the BPR and by pass valve slowly.
2. Prepare 1 L of salt solution to adjust the feed concentration at the desired level.

A.3.5 Salt addition and equilibration

1. After 1 hr of pure water filtration pour salt solution into the tank slowly.
2. Let the flux to equilibrate and concentration polarization layer to build up for 1 hr.

3. After 1 hr collect one sample (15 mL) of feed solution. This will be used for calibration and to subtract the UV absorbance of salt to from the UV absorbance of sample during the mass deposition study.

4. Prepare specific amount of silica to add into the feed tank and obtain desired feed concentration of silica.

A.3.6 Silica addition and fouling experiment

1. Add the specific amount of silica into the feed tank, stir the solution and collect sample (20 mL) after 2 minutes.

2. This sample will be used for calibration and consider as the known initial silica concentration of feed.

3. Then collect samples (15 mL) every after 30 minute interval until the permeate flux reaches to steady value. After the flux reaches to steady state value collect samples every after 45 minutes.

4. After 5 hrs collect the final sample and then shut down the pump first. This will allow keeping the deposited mass on membrane surface, and using the fouled membrane for further analysis.

A.3.7 Setup cleaning

After shutting down the pump, clean the setup according to the following procedure:

1. Remove the flow meter from the permeate line and keep at a safe place.

2. Release the hydraulic jack and bring the membrane module out. Remove the upper part and take the membrane out. Keep it at a safe location with the details of experimental condition for further study.

3. Remove the permeate carrier, shim and feed spacer (if used), and wash them.

4. Place the o-rings at proper position and return the membrane module to the hydraulic chamber and jack the pressure to 300 psi. Keep the valve at permeate line closed.

5. Fill the tank with around 5 to 7 liter of water and start the pump. Keep the feed pump running for 10 minutes.

6. Shut down the pump and drain the tank water. Completely fill the tank with new clean water and start the pump again. Brush the tank wall, heat exchanger to clean them.

7. Shut down the pump, pour new water in the tank, start the pump and let it run for 1 hr.

8. Take a sample from the tank, measure the UV absorbance of the sample and check against the lab demineralized water UV absorbance. If these two values are same the setup is clean for the next experiment.

A.3.8 Measurement of UV absorbance of feed samples

Take the collected samples for UV absorbance analysis and do the scanning of each sample according to the following procedure:

1. Start the computer and wait for at least 15 minutes to warm up the instrument.

2. Start the software, run scan and open the setup option.

3. Set the scan width from 300 nm to 200 nm for silica samples, scan speed to medium, base line correction of multi base line to zero, activate cell change and use cell no 3 for scanning and save these settings.

4. Clean the 10 mm quartz cuvette and pour the sample in it. Place the cuvette in the UV-VIS spectrometer and click start.

5. After finishing the measurements save all the data in to a *.csv file.

A.3.9 Particle concentration measurement

The absorbance results of UV-VIS spectrometer were used for concentration measurement. The calibration was done using 3 points serial dilution method for each experiment. The salt sample collected prior to silica addition and feed sample collected after 2 minutes of silica addition was used for the calibration. The feed sample of 3 mL was taken in the quartz cuvette and considered as the initial known concentration ($C_{p,0}$) of the experiment. Then, the UV absorbance of the sample was measured. After that, the initial feed sample was diluted to $2C_{p,0}/3$ and $C_{p,0}/3$ using the salt sample for calibration. The UV absorbance of the diluted samples and salt sample were measured. The

absorbance of salt was subtracted from the absorbance of calibration samples to obtain the absorbance of silica. The results were then plotted in concentration vs. absorbance graph as shown in Fig. A.1. Table A.1 gives the UV absorbance results of calibration corresponding to experiment no. 5 listed in Table 5.1. The calibration equation was used to measure the feed concentration ($C_{p,t}$) of different time interval samples and calculate the deposited mass using Eq. 4.8.

Table A.1 – Calibration result of experiment no. 5 in Table 5.1

Concentration (mg/L)	Abs. of calibration samples	Abs. of Salt solution	Abs. of silica
300	0.68746	0.0777	0.60976
200	0.48468	0.0777	0.40698
100	0.27963	0.0777	0.20193

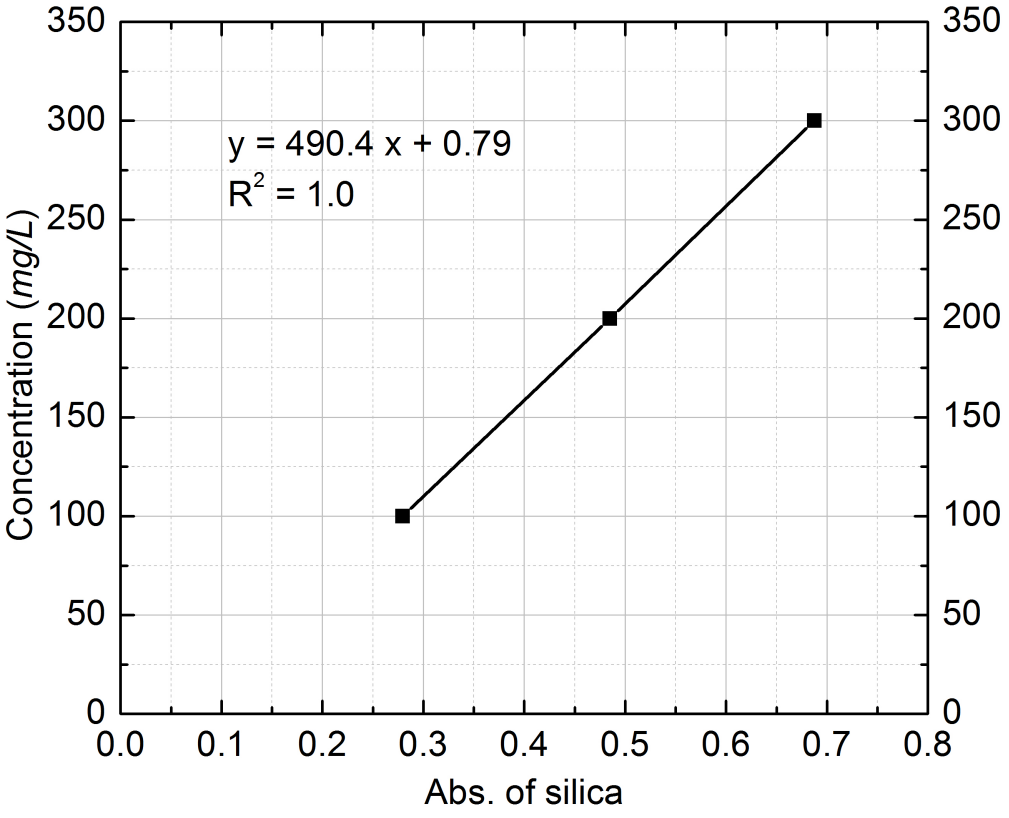

Figure A.1 – Concentration (mg/L) vs. Abs. of silica